# Mechanical Responses of Neuronal Cells and Spider Silk

by

**Sushil Dubey**

**A thesis submitted to the Jawaharlal Nehru University**
**for the degree of DOCTOR OF PHILOSOPHY**

August 2020

## DECLARATION

I, hereby, declare that this thesis is composed independently by me at Raman Research Institute, Bangalore, India, under the supervision of Prof. Pramod A Pullarkat. The subject matter presented in this thesis has not previously formed the basis of the award of any degree, diploma, associateship, fellowship or any other similar title in any other University. I also declare that I have run it through the Turnitin plagiarism software.

Prof. Pramod A Pullarkat
Raman Research Institute

Sushil Dubey
Raman Research Institute

## CERTIFICATE

This is to certify that the thesis entitled **Mechanical Responses of Neuronal Cells and Spider Silk** submitted by Sushil Dubey for the award of the degree of DOCTOR OF PHILOSOPHY of Jawaharlal Nehru University is his original work. This has not been published or submitted to any other University for any other degree or diploma.

Director
Raman Research Institute

Prof. Pramod A Pullarkat
Thesis Supervisor

*To my family*

## ACKNOWLEDGEMENTS

Many people have contributed to make this thesis successful. I would like to take this opportunity to thank and express my gratitude towards them.

The first and the most due expression goes to my PhD supervisor, Prof. Pramod Pullarkat, who introduced me to the interdisciplinary field of biophysics. He showed a lot of patience throughout these years. Without his constant encouragement and support this thesis would not have been a reality. I also would like to thank him for the freedom he gave. I am overwhelmed by his patience and humility.

I would like to thank my collaborators Andrew Callan-Jones (Paris Dedirot, Paris), Aurnab Ghose, and Sayantan Majumdar for their help and support. Without their support it would have not been possible. I would like to thank Nishita for spetcrin work, Chinmay for silk work, Sukh Veer for silk analysis, and Shivani for super-resolution imaging. I would like to thank Arsalan for his help with some of the graphics in the thesis.

I am grateful to Prof. V. A. Raghunathan and Dr. Gautam Soni for assessing progress of the work every year and providing positive inputs about the projects. I would like to thank Prof. N. V. Madhusudana, Prof. Ranjini Bandyopadhyay, Prof. R. Pratibha, Dr. Arun Roy, and Prof. Sandeep Kumar for the discussions, suggestions and help.

I would like to thank our group secretary Radhakrishna and other staff including Ishaq, Murali, Vasudha and Raja. I would also like to thank RRI Administration for taking care of most of the formal/official procedures from time to time. I thank Krishnamaraju, C.S.R. Murthy, Naresh, Vidya, Radha, Shailaja, Ram and Marisa. I would like to thank Achan, Ibrahim, Dhason and Mani from the mechanical workshop for their help in making mechanical accessories for the force device. I thank Yatheendran for his help with electron microscopy and confocal microscopy. I thank Som, Rishin and GK of electronics work shop.

I would like to thank all the library staff for their help, especially Meera, Manjunath and Nagaraj. I would like to thank the computer department Jacob, Sridhar,

and Krishnamurthy for their help. I would like to thank the Purchase section and Accounts section for all their help. I would like to thank GB Suresh, Sridhar, Muneeswaran, and others from civil and electrical department.

I am lucky to have wonderful lab-mates around. I thank Giri and Renu for their friendship, care and support. I also would like to thank Giri for help with device and instrumentation. I would like to thank Anagha, Arsalan, Ashish, Jaisha, Sukh Veer, Laxmi, Amal, Alka, Susav, Serene, Praveen, Madhu for just being there for me.

I would like to thank Madhukar, JK, Swamy, Mari, Surya, Jaggu, Irla, Santanu, Saichand, Nishant, Nancy, Adwaith, Rajkumar, and Ashutosh for the discussions and gossips. I would like to thank Jagdish, Sanjay, Sreeja, Chandeshwar, Palak, Tiwari, Amit, Anand, Raj Prince, Vishnu for the fun time in RRI and hostels.

I would like to thank my teachers Ratan Lal Jaiswal, Dr. A.P. Srivastava, and Dr. B.K. Verma for their motivation and encouragements.

I would like to thank my friends Alok, Gaurav, Nisha, and Subrata for their unconditional support and friendship. I would also like to thank Sanjeev, Chiru, Satyam and Durgesh for their support.

I thank Meera, Raj, and Ashish for their help and support and the awesome times we spent from the course work time to till date. I would like to thank Karamveer, Raviranjan, Debsankar, Niranjan, Abhijit, Anirudh, Abir, Kartik, Deepak, Shivam, and Priyanka for their support and help.

At last but not the least, I would like to thank my (late) grandparents for their constant support, blessings and prayers and encouragement. I would like to thank my parents, brothers and family members for their unconditional love, support, and encouragements. I thank all my other family members and friends for their support and encouragement.

Sushil Dubey
Bangalore
August, 2020

# SYNOPSIS

## Introduction

This thesis highlights the studies on neuronal cell mechanics and spider silk mechanics using a custom built optical fiber based force device (Micro-Extension Rheometer) [1]. Neurons are unique cells in their morphology, typically extends from hundreds of micrometers to about a meter in a human body. Axons, the extension of neurons, having a thin tubular structure about a micron in diameter which transmits signals. How these thin extensions maintain its shape and integrity over such a large range is always a curious question [2, 3]. Axons can be subjected to large stretch deformations under a variety of normal as well as abnormal conditions. For example, the human brain, being one of the softest tissues, undergoes significant shear deformations (2–5% strain) even under normal activities such as jumping [4]. Using the force device, we probed the axonal cytoskeletal mechanics of neuronal cells and investigated the role played by different cytoskeletal filaments and proteins to mechanical stretch. In short, we probed axon mechanics using techniques such as Micro-Extension Rheometer, chemical perturbations, genetic alternations, and super-resolution imaging.

Spider silk is strongest natural material known to us which makes it an interesting bio-material to study their mechanical properties. Silk exhibits unique mechanical properties like large extensibility, high tensile strength, super-contractility, etc. Among all types of silk, dragline silk is strongest one which is the main structural part of the web [5, 6]. We have probed rheological properties of dragline and cribellate silk from social spiders with different rheological protocols.

These two materials occur in nature as thin and long strands and are constantly subjected to stretching forces–due to limb movement or shear deformation of brain in case of axons and impacts of insects or movement of branches in silk. Most fascinating thing is, having thin tubular structure of few micrometers in diameter and they grow/evolve over extreme lengths. So it is very interesting to study

the mechanical properties of these materials. We show that these biomaterials of completely different origins share common strategies to cope with mechanical stretch or stress.

Research work presented in this thesis is divided broadly into two parts:
(i) Neuronal cell mechanics and the role of their different cytoskeletal filaments and proteins
(ii) Rheological properties of silk from Social spider

## Neuronal cell mechanics and the role of their different cytoskeletal filaments and proteins

Neurons are unique cells in their morphology which extends from few micrometres to about a meter in human body. A neuronal cell typically has a cell body (soma), a long thin tubular extension called axon and a palm like structure known as growth cone (growing end of the neuron). In order to achieve such extreme aspect ratios, axons have evolved a unique organisation of the cytoskeleton. The axonal cytoskeleton has three main types of filaments–bundled-microtubules, actin filaments and neurofilaments [2, 3]. Recent experiments using super-resolution light microscopy have revealed that the actin cortex also involves a periodic array of F-actin rings which are interconnected by spectrin cross-bridges [7]. These filaments respond to externally applied mechanical stimuli [3, 8]. The mechanism of how axons regulate their tension is not fully understood [9–11].

In this part of the thesis, we investigated the role played by different cytoskeletal filaments and proteins to the mechanical stretch. Using the force device, various cytoskeleton perturbations, and genetic alterations, we have probed the axonal cytoskeleton mechanics.

### The Advanced version of Micro-Extension-Rheometer

The Micro-Extension-Rheometer was modified and advanced against the requirements of the neuron and silk experiments. A motorized XYZ positioning stage (Xenoworks) was used to hold the Piezo drive. Various LabVIEW codes were

written to enable different rheological protocols in feedback mode such as step strain, successive step strain, successive step strain along with oscillations, cyclic strain, ramp, etc. The set up was also modified to investigate active fluctuations in axons in which the fiber tip (adherent to axon) position was recorded on a Quadrant Photo Diode (QPD) and corresponding power-spectrum was calculated.

**Axons show viscoelastic solid-like response and exhibit strain softening**

A home built optical fiber based force device mentioned above has been extensively used to probe the mechanical response of axonal cytoskeleton [1]. Mechanical response of neuronal cells subjected to tension using the force device shows non-linear viscoelastic behaviour. To study the mechanical response of axons as a function of imposed strain, we applied successively increasing strain steps. The force relaxation data, elastic modulus, and relaxation curves are shown in Fig. 1. From this data, we conclude that axons behave as viscoelastic solid-like and show strain softening response. The tension relaxation curves were fitted with double exponential $(Aexp(-t/\tau_1) + Bexp(-t/\tau_2) + C)$ where $\tau_1$ and $\tau_2$ are the two relaxation times. The relaxation times obtained from tension relaxations curve are non-monotonic on the applied strain [12].

**Cytoskeleton perturbations and contribution of different filaments towards mechanical response**

To test the relative contributions of different cytoskeletal filaments, we performed experiments with either stabilizing or destabilizing microtubules and F-actin. To check if microtubules dynamics could lead to strain-softening observed, We first tested the response of axons treated with Taxol (Paclitaxel), a microtubule stabilizer, and resulted in elastic moduli show a strain-softening response similar to normal axons but higher in moduli compared to the normal axons. Next, in order to check whether F-actin dynamics could lead to strain-softening, we treated neurons with Jasplakinolide a F-actin stabilizing agent. F-actin-stabilized axons exhibit a more substantial increase in the elastic moduli compared to Taxol treatment, while both display pronounced strain-softening.

We then performed measurements after disrupting microtubules and F-actin filaments. Microtubules depolymerization with Nocodazole (Noco) shows a slight

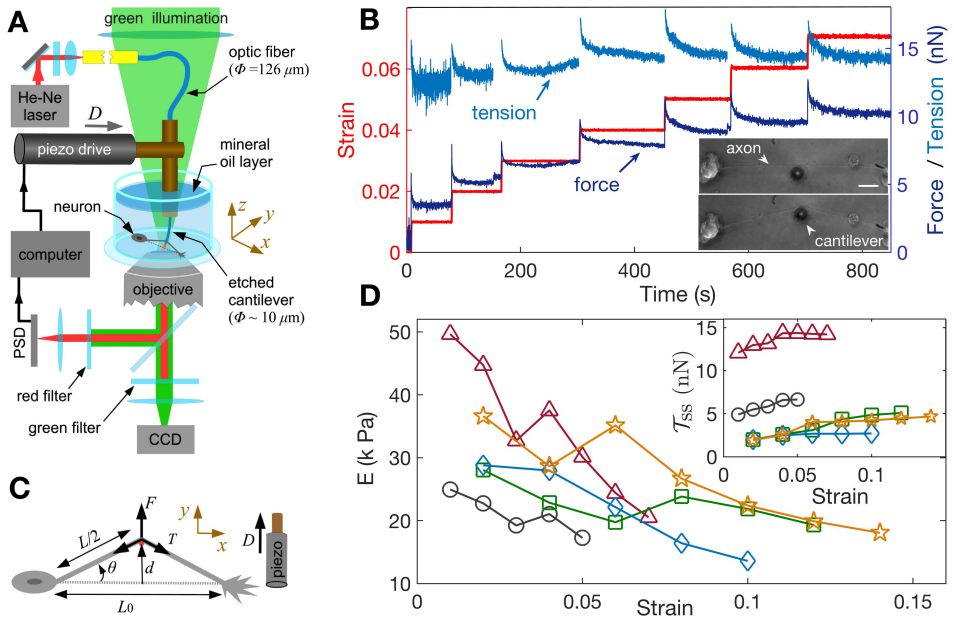


FIGURE 1: (A) The schematic of the home-developed force apparatus (MER) that uses an etched optical fiber as a cantilever to stretch axons and to sense force (B) Axonal response to increasing strain explored using successive strain steps and the resulting force response. The calculated tension in the axons is also shown. The inset shows the images of the axon before and after stretch (C) Schematic to calculate tension in axons (D) Elastic moduli calculated for different axons using the steady-state tension after each step show a strain-softening behaviour. The inset shows the tension vs. strain plots for different axons.

reduction in steady-state tension where as F-actin disruption with Latrunculin-A shows a dramatic reduction in steady-state tension of axons. In addition, the tension-relaxation is much faster for Latrunculin-A treatment as compared with either Nocodazole-treated or control axons suggesting that F-actin plays a leading role in strain-softening in axons.

**Role of the actin-spectrin lattice in the mechanical response of axons**

Recently discovered actin-spectrin skeleton could be responsible for the observed force response in axons keeping in mind that F-actin disruption shows a significant reduction in steady-state tension. The axons of spectrin knock-out animals are known to snap during normal wiggling of the worm. Spectrins are also held under pre-stress shown using FRET measurements [13]. Using super-resolution imaging and spectrin knockdown experiments, we have quantified the role of actin-spectrin skeleton to mechanical stretch.

We first did super-resolution imaging (STED nanoscopy) to show that actin-spectrin are arranged in a periodic fashion in chick neurons which reveals the ultrastructure of axons at various Days In Vitro (DIV). It has been shown that the periodic lattice becomes more prominent and more prevalent with the number of days the neurons are in culture while maintaining a periodicity in the range of 190–200 nm which has been shown in Fig. 2(A, B(inset)). The predominance of the actin-spectrin lattice with age is well correlated with the mechanical response, with axons of aged neurons showing much higher values of elastic moduli as can be seen from Fig. 2(B). Using genetic alterations with Morpholino, we knocked down(suppression of particular protein) spectrin proteins and shown that there is reduction in force response compared to control Morpholino (no suppression) treated cells. Depletion of $\beta$-II spectrin has been reported to abolish the development of the periodic organization of the actin-spectrin membrane-associated skeleton [14]. Anti-$\beta$-II spectrin Morpholino-treated axons show a dramatic decrease in the steady-state tension compared to axons treated with a non-specific Morpholino as shown in Fig. 2(C). The extent of spectrin knockdown was quantified using antibody labelling and confocal microscopy and the result is shown in the inset of Fig. 2C, demonstrating a correlation between reduction in spectrin content. The results of the extent of knockdown and reduction in steady-state tension demonstrate the importance of the actin-spectrin periodic skeleton to mechanical response of axons.

**Folding-unfolding of spectrin buffers axon tension**

To explain our observations of axon strain-softening, we then developed a minimal model of the axon mechanical response. We model tension relaxation as arising from unfolding/refolding of repeats along a spectrin tetramer, which is known to yield softening at the single tetramer level. These unfolding events lead to dissipation of stored elastic energy. Taking unfolding/refolding force dependent, we showed that relaxation times are non-monotonic with applied strain. Using this simple model, we explained the experimentally observed strain-softening, non-monotonic tension relaxation and predominance role of actin-spectrin in axonal mechanical response.

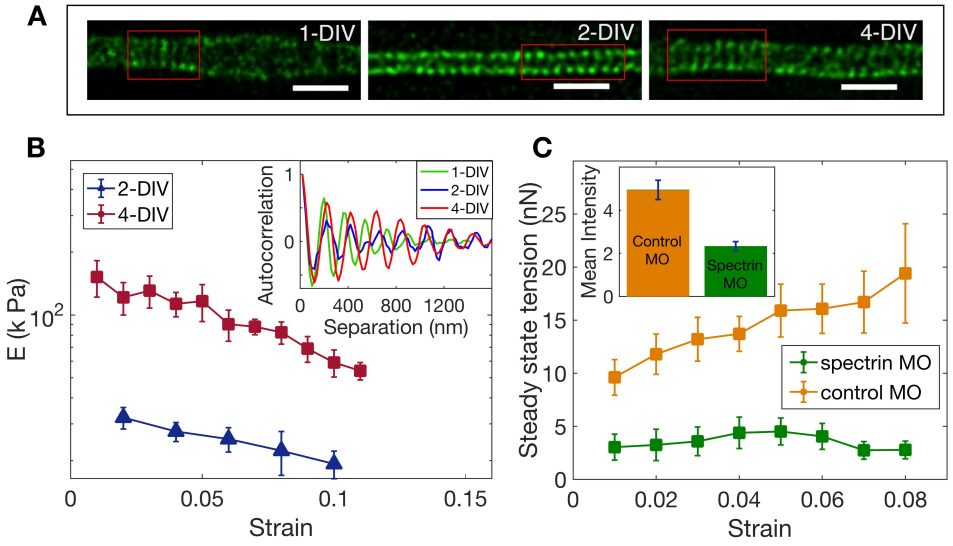


FIGURE 2: (A) STED nanoscopy images of axons immunolabelled with $\beta$-II-spectrin antibody for axons at various DIVs (Scale bars = 1 µm). (B) Plots of averaged elastic moduli vs strain for axons at 2-DIV and 4-DIV show a increase in moduli with age. The inset shows autocorrelation functions obtained from the regions marked by the red-boxes (C) Plots of the averaged steady state tension $T_{ss}$ as a function of strain for 2-DIV neurons treated with a non-specific, control Morpholino and for those treated with an anti-$\beta$-II spectrin Morpholino. There is a substantial reduction in the tension measured after knock-down. The inset shows the extent of the knock-down obtained using antibody labelling of spectrin for control.

## Rheological properties of silk from Social spider

In this part of the thesis, Rheological Properties of social spider silk *Stegodyphus sarasinorum* was studied using the force device mentioned earlier. Dragline silk produced by spiders known to be toughest material known to nature till date that is why mechanical properties of dragline interests to many [5]. Earlier studies on silk mechanics are by applying cyclic, linear stretching or single stretch up to the yield or break point. Various quantities like yield stress, yield strain, breaking stress, breaking strain, Young's modulus and dissipation are calculated using this data [6, 15]. Here we show a device which is capable of a full characterization of the linear and non-linear rheological properties of silk in extension mode. We found that elastic modulus shows softening followed by a stiffening response. The unfolding of the $\beta$-sheets present in the silk can explain this phenomenon.

### Measurement at small strain

To obtain the elastic moduli at equilibrium states with different amounts of pre-strain, we used a sequential step strain protocol where the silk is stretched by increasing amounts of strain, and the modulus is measured at steady state using small strain sinusoidal oscillations. We observe that silk exhibits an initial strain softening for up to about 4% strain. The relaxation times obtained from stress relaxation curve increases monotonically with increasing strain. The tension relaxation curves were fitted with double exponential $(Aexp(-t/\tau_1)+Bexp(-t/\tau_2)+C)$ and relaxation times were shown in Fig. 3. Using a Fourier analysis method, we also extract the frequency dependence of the elastic and viscous moduli from the relaxation process.

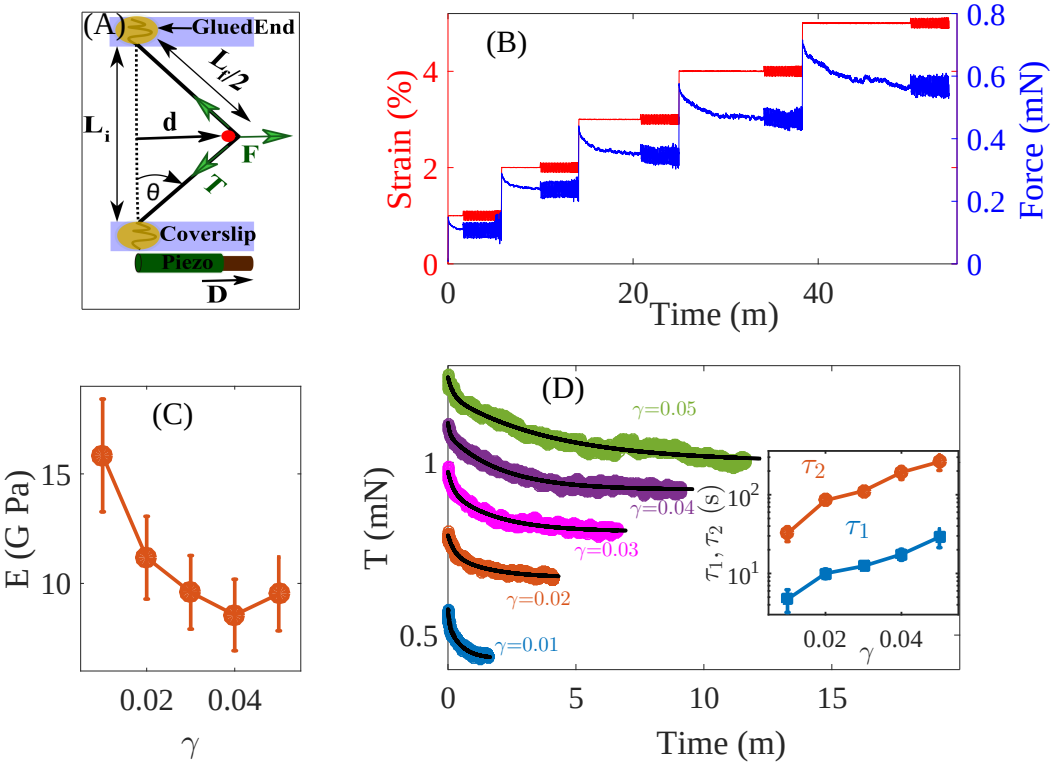


FIGURE 3: (A) Schematic of a silk strand pulled using the optical fiber. (B) Typical force response of silk subjected to sequential strain steps along with small oscillations.The force relaxes to a steady state value after each step and this steady state force increases with strain showing that silk behaves as a viscoelastic solid. (C) Storage moduli calculated using the sinusoidal oscillations exhibit a strain-softening behaviour. (D) The tension relaxation curves obtained for each step is fitted to a double exponential to extract the relaxation times. A log-linear plot of the variation of these relaxation times as a function of strain is shown in the inset.

### Large strain and Energy dissipation

Silk shows initial softening followed by stiffening and obtained relaxation times monotonically depend on imposed strain Fig. 4. Using ramp protocol we found the energy dissipation while silk is stretched. The area enclosed was calculated at various strain ranges. From different stress-strain curves, it has been shown that area initially decreases and later saturated which is indicative of limit cycle. At various pre-strain, (Lissajous figures at different strain levels) it has been shown that evolution the Lissajous figure corresponds to stiffening regime which has also been evident from our high strain data. We show that the area enclosed in the loop is independent of applied frequency range of (0.01–1 Hz).

### Ageing of spider silk

We have done force measurement on fresh silk and aged silk (same silk fiber but aged for 10-12 months). We see that Silk becomes stiffer after ageing, i.e. rise in elastic modulus of aged silk. We also observed that relaxation times decrease with applied strain. The decrease in relaxation times can be explained as follows– $\tau = \eta/E$ ; if $E$ will increase $\tau$ will decrease.

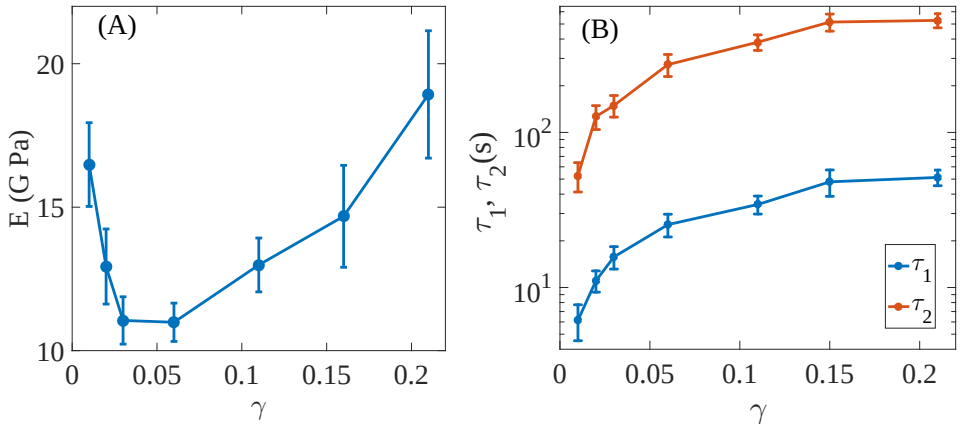


FIGURE 4: (A) Elastic modulus for high strain for dragline silk (B) relaxation times plotted as function of strain for higher strain show monotonic increase in relaxation time.

### Possible mechanism

It has been shown that spider silk consists of amorphous and crystalline regions. The crystalline region is composed of $\beta$-sheets. It has been shown that the unfolding of $\beta$-sheets could give rise to strain softening behaviour observed in silk which

does not include monotonic dependence of relaxation times [16]. We aim to build a minimal model to incorporate our all observed results.

## Summary

The studies of this thesis are focussed on two biomaterials of completely different origin. But it seems that nature has employed a similar mechanism in these two systems to protect them from stretch deformation. In first part of the thesis actin-spectrin skeleton protect neurons from stretch induce damage having repeated spectrin unfolding units whereas in the second part in silk $\beta$-sheets supposed to protect spider web from large deformation via $\beta$-sheets unfolding. The study described in the thesis provides a better understanding of axon biomechanics and spider silk mechanics.

## Publications

- Sushil Dubey, Nishita Bhembre, Shivani Bodas, Sukh Veer, Aurnab Ghose, Andrew Callan-Jones, and Pramod A Pullarkat. The axonal actin-spectrin lattice acts as a tension buffering shock absorber. *eLife*, 9:e51772, 2020.

- Sushil Dubey, Chinmay Hemant Joshi, Sukh Veer, Divya Uma, Hema Somanathan, Sayantan Majumdar, and Pramod A Pullarkat. Strain softening and stiffening responses of spider silk fibers probed using Micro-Extension Rheometer. *Soft Matter*, 16:487-493, 2020.

# Contents

# Chapter 1

# Introduction

The brain is one of the most complex organs and softest tissues of the human body. The human brain has billions of neurons [17]. The brain undergoes significant shear deformations (2–5% strain) even under normal activities such as jumping [4]. Hence, knowing how and under what conditions brain deformation compromises axonal integrity is considered essential to understand, manage, and treat concussions [18].

The long processes in neurons called axons, which transmit signals to the other cells, typically grows up to the order of centimeters in the brain and up to a meter long in the peripheral nervous system of a human body [2, 3]. The mechanical force responsible for the axonal injury is the rotational acceleration of the brain, resulting from unrestricted head movement inducing dynamic shear, tensile, and compressive strains within the tissue. Even at a mild injury, loss of consciousness was induced following rotation transverse to the brainstem [19]. This injury interrupts axonal transport and induces progressive swelling and degeneration. There is a considerable amount of evidence to show that the primary cause of concussive injuries is the inertial, or acceleration, loading experienced by the brain at the moment of impact [20]. Evidences suggest that just a single traumatic brain injury may be associated with the later onset of neurodegenerative disorders, including Alzheimer's disease [19–22]. Axons are key injury sites in injury-induced trauma and coma [18, 22]. At a higher age, mammals tend to lose their axons, which are enhanced in neurodegenerative disorders [23, 24].

Axons are under stretch caused by the expansion of surrounding tissue or overall growth while embryos develop, and to maintain connections, it has to accommodate materials in response to the stretch. Moreover, axons are under mechanical tension throughout the life of the organism [25]. Notably, neurons can not be replaced; this means that most of the axons have to be maintained over the lifespan of the organism [23, 24, 26].

Axons can be subjected to large stretch deformations under a variety of normal as well as abnormal conditions. They are subjected to repeated stretching during limb or other body movements. For example, the mammalian sciatic and median nerves can experience localized strains up to 30% during regular limb movements [27]. While Peripheral nerves are susceptible to stretch injury, in extreme cases of stretching occurs in the nerves running along the mouth-floor of certain species of baleen whales where it elongates up to 160% during feeding [28].

The field of neuroscience has progressed in the past few decades, but neuromechanics remains poorly understood. The mechanical behaviour at a single cell level has been extensively studied. Axons are shown to behave viscoelastically when stretched [9]. Axons can develop excess mechanical tension due to stretch [9, 11]. Despite the observations of such a rich variety of mechanical responses, the contribution of different cytoskeletal elements and their mechanical responses are poorly understood [10, 29–32]. This thesis describes the contributions from the various cytoskeletal components of the axonal cytoskeleton due to mechanical stretch.

## 1.1 Neuronal cells

Neuronal cells have a unique morphology, as shown in Fig. 1.1. It consists of a cell body or called soma with a nucleus, dendrites, and a long extension called axons, which typically extends from few microns to up to about a meter in a human body [2, 3]. The palm-like structure called growth cone is the growing end of the axon (Fig. 1.1) and it interacts with the extracellular environment to find its target. To transmit signals, dendrites and axons form special connections known as synapses

to communicate with other neuronal cells. In the functioning of neuronal cell dendrites receive the electrochemical signals which pass through the cell body and axon carry the signal to the other targeted cells [2, 32].

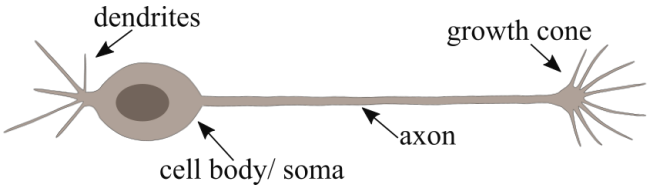


FIGURE 1.1: **Neuronal cell morphology.** Neurons having unique morphology extends long processes, which are thin tubular structures called axons. Typically axons are a few hundred microns to a meter long in a human body. Dendrites receive signals from other cells which travel through the axon and reaches to the target cell. The palm-like structure called the growth cone, which senses the extracellular environment during path-finding. The growth cone pulls and generates tension along the axon. This tension causes protein synthesis in the cell body, and these synthesized proteins reach the growing end in response to tension.

## 1.2 Neuronal structure and the cytoskeleton

The cytoskeleton provides structure and shape to the cell. The cytoskeleton plays an important role in cell shape, movement, mitosis, etc. The cytoskeleton has three main types of filaments—microfilaments, intermediate filaments and microtubules. The axonal cytoskeleton comprises three main types of filaments, namely, microfilaments, which are called actin filaments, Intermediate filaments, which are called neurofilaments (NFs), and microtubules. A variety of molecular motors and other associated proteins play an important role in the organization and dynamics of these filamentous structures [2, 3, 34]. These filaments in cells reorganize themselves to resist deformation from externally applied stimuli. Dynamics of actin and microtubules along with molecular motors guide the cellular transport [3].

Microtubules are the stiffest filaments, and due to its stiffness and bundling, it is hypothesized that microtubules are the major load bearer in axons. The actin filaments are less stiff than microtubules, but in the presence of crosslinking proteins, they can form a highly stiff non-linear structure [35]. Whereas Neurofilaments are the least stiff biopolymers among all [2, 3, 34].

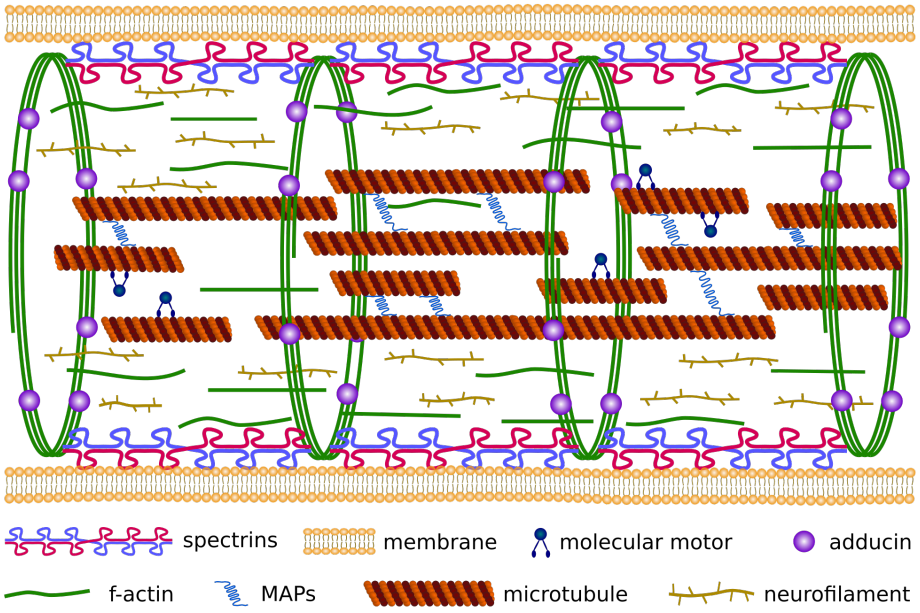


FIGURE 1.2: **Axonal ultrastructure.** Axons are about a micron thick. Typically, the axonal core has a bundle of polar microtubules which are cross-linked by a variety of microtubule-associated proteins including Tau (in some cases a more loose organization of microtubules interdispersed with neurofilaments [33]). The molecular motors use microtubules that have their plus ends towards the growth cone as road tracts for transport. This core is surrounded by neurofilaments. The outermost scaffold has an array of periodically spaced rings composed of F-actin filaments. The actin rings are interconnected by $\alpha$ and $\beta$ spectrin tetramers, which are aligned along the axonal axis (only tetramers in a cross-section, are shown for clarity). Other cortical F-actin structures also exist as well as in the form of waves and trails. A myriad of proteins, including motor proteins (not shown), interconnect the various filaments, and also the membrane to the inner skeleton. The actin rings are about 200 nm apart, which is the typical spectrin tetramer length.

### 1.2.1 Microtubules (MTs)

Microtubules are the stiffest filament among all, having a persistence length of about a millimeter and a diameter of ∼25 nm. Microtubules are hollow cylindrical bio-polymers typically made up of 13 protofilaments of $\alpha$ and $\beta$-tubulin heterodimers having growing end called plus-end and degrading end called minus-end (Fig. 1.4) [2, 3]. In vertebrate axons, MTs organization is unique, and are arranged in a polarized fashion. MTs are oriented with their plus-end away from the cell body, whereas, in dendrites, their orientation is with mixed polarity [36]. This unique orientation in the axon has important implications for its function since it affects the specific sorting of axonal and dendritic cargoes. The axonal cytoskeleton consists of co-axially bundled microtubules which are interdispersed by

the neurofilaments matrix [33]. Axonal cross-sections typically have 10-100 MTs organized often in bundles (Fig. 1.2) [2, 3, 36, 37]. Microtubules dynamics are regulated by a large number of factors, including Microtubule-Associated Proteins (MAPs), motor proteins, which influence microtubule dynamics. Microtubule-Associated Proteins like Tau play a significant role in modulating the stability of MTs in axons. Cross-linking tau proteins stabilize microtubules and establish a homeostatic equilibrium state of axonal tension [31].

These filaments also undergo dynamic instability [3]. Under low stretch rates of the order of minutes, axons easily tolerate stretches up to twice their original length with no evidence of damage. Under higher stretch rates, axons display a progressive loss of microtubules. This study suggests that progressive loss of microtubules in response to rapid axonal stretch [21].

### 1.2.2 Neurofilaments (NFs)

Neurofilaments are flexible and apolar polymers. Neurofilaments have a persistence length of $\sim$1 μm and a diameter of $\sim$10 nm. Neurofilaments are stable and completely polymerized polymers within the cells [3, 37]. NFs form a dense network of discontinuous, cable-like filaments along the axon, which are interconnected by small extensions [38]. There are three types of neurofilaments subunits that differ in their molecular weight–light (NF-L), medium (NF-M), and heavy (NF-H). These subunits form dimers, each with the NF-L subunit. After dimerization, they arrange in pairs to form biochemically stable tetramers [17, 38]. NFs are aligned in the orientation of MTs along the axon, and the three cytoskeletal filaments (actin, NFs, and MTs) are interconnected by a separate family of proteins known as plakins [38].

In axons, using electron microscopy by Hirokawa [33], two specialized regions are found–bundles of MTs, which were linked with each other by shorter cross-bridges, and NFs were also crosslinked with each other. Most of the axoplasm was filled with longitudinally oriented NFs [33, 39]. Neurofilaments are hypothesized to set axonal diameter [40].

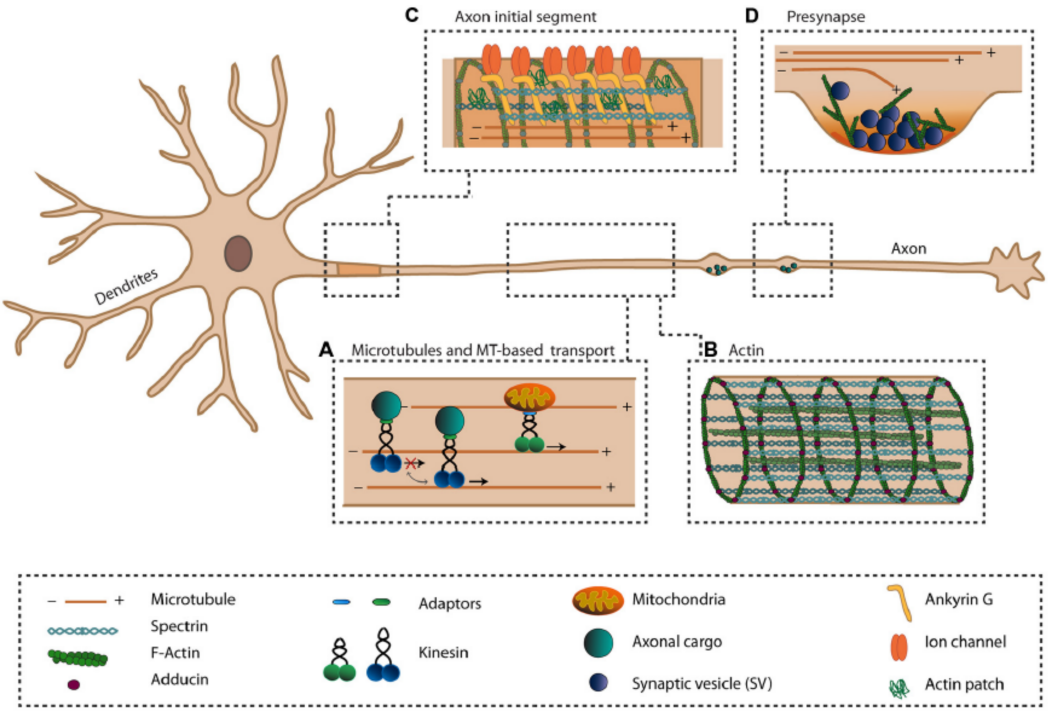


FIGURE 1.3: **The axonal cytoskeleton and axon specific structures.** The axon is specialized in transmitting information to other cells. To ensure this function, the axon has a unique cytoskeletal organization (A,B) and has several specialized structures (C,D). (A) The unique unipolar orientation of the microtubules(MTs) within the axon provides anterograde transports of various axonal cargoes via plus-end directed kinesins. Various mechanisms exist that regulate the activity of kinesins. (B) The actin cytoskeleton within the axon exists as periodically spaced rings underneath the axonal plasma membrane, organized by spectrin and adducin, and provides the axon with elastic and stable support. Along the axon, bundles of actin are present. (C) The axon initial segment (AIS) is important for the initiation of action potentials and maintaining neuronal polarization by acting as a transport filter. Within the AIS, a dense meshwork of cytoskeletal and scaffolding proteins exists where Ankyrin-G(AnkG) links transmembrane proteins to the actin and microtubule cytoskeleton. (D) At the presynaptic site, neurotransmitter-filled synaptic vesicles(SVs)are docked at the presynaptic membrane and undergo exocytosis upon the arrival of an action potential. Within the presynapse, actin is proposed to exist in a branched network where it may function in the controlling exo-and endocytosis, recruiting and positioning of SVs and organizing the activezone (AZ) (figure and caption adapted from [37]).

### 1.2.3 Actin filaments (F-actin)

Actin-filaments are semi-flexible fibers, which are crucial for the growth cone motility of neuronal cells. Actin filament has a persistence length of ∼10 µm and a diameter ∼4–5 nm. Actin filaments (F-actin) are formed by actin monomers called globular actin (G-actin) and are polar biopolymers that form a double-stranded helix (Fig. 1.4). On the growing end of F-actin called barbed end, subunits (G-actin) are added while on the opposite side, the pointed end, monomers dissociate,

the process called tread-milling. Due to the weak interaction between these actin monomers, actin filaments rapidly shift between polymerized and depolymerized states. F-actin forms cortical mesh, contractile bundles, contractile rings, etc. F-actin is mostly found in axonal cortical mesh, whereas a dense bundle is found in neuronal filopodia. Actin dynamics is regulated by numerous actin-binding proteins (ABPs) via various mechanisms [2, 3, 8, 37]. These mechanisms are nucleating actin filaments, sequestering actin-monomers, inhibit or promote actin polymerization or depolymerization by capping or binding to the barbed or pointed end, the severing of actin filaments by ADF/cofilin, bundling, crosslinking, stabilizing, and anchoring to other cellular elements. F-actin is known to be providing cortical scaffold to the plasma membrane. Before the discovery of actin rings, actin was assumed to exist in the cortical region that contains a dense mesh of actin filaments. This dense mesh was connected to microtubule cytoskeletal network via microtubule-associated proteins which regulate microtubule dynamics, bundle actin filaments, and cross-link actin filaments with microtubules [33, 37].

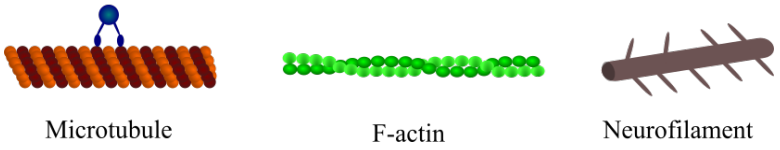


FIGURE 1.4: **Elements of the cytoskeleton.** Microtubules which are made from $\alpha$-$\beta$ heterodimers; shown along with the molecular motor, Actin filaments that are made from G-actin monomers and form a double-stranded helix and neurofilaments with side-arms.

The Recent discovery has unraveled the membrane periodic scaffold formed by actin and spectrin skeleton, which are arranged in a periodic manner [7, 41, 42]. The actin-spectrin skeleton was found beneath the plasma membrane arranged in a periodic fashion along the axons like a 1-D periodic lattice structure and wrapped around the circumference of the axon (Fig. 1.2, 1.3)[7, 41]. The actin ring comprises short actin filaments that are capped by capping protein adducin and connected by spectrin tetramers, which are arranged with a regular periodicity of 180-190 nm between the rings. This membrane periodic skeleton is suggested to provide mechanical integrity to axons [7, 41, 42]. Apart from these stable ring structure, F-actin is also present in the form of dynamic actin, which is hotspots, waves, and trails, and filamentous actin. This suggests that the stable

actin rings maintaining mechanical integrity and dynamic actin provide flexibility and in maintaining synaptic plasticity [43, 44] (a detailed description of actin rings is given in chapter-4).

## 1.3 Axonal Transport

Axons are long processes of neurons that range typically from a few hundreds of microns to a meter long. Having this length, material transport by diffusion will take an enormous amount of time (several days) to reach the traverse length of the axon. For this reason, axons have specialized machinery to transport materials from the cell body to specific targets [34, 37]. The axonal cytoskeleton plays an important role in the active transport of proteins, vesicles, and organelles throughout the axon. The axon, functionally different from the dendrites, requires a different set of proteins and cellular organelles to transport. Active motor protein-driven transport is essential for sorting these axonal cargoes and to ensure that the correct proteins reach the right location within the cell [37]. Axonal MTs organized with their plus-ends towards the growth cone act as rail-tracks for the transport of many neurotransmitters, organelles, and cytoskeletal elements that are carried as cargoes [2, 36]. The motor proteins which transport cargoes along the axonal cytoskeleton are kinesins and dyneins. Kinesin moves towards plus-end, and dynein towards minus-end along microtubules to facilitate long-range transport. Since microtubules have a polarized organization in axons, therefore kinesins are responsible for the anterograde (away from the cell body) transport of axonal proteins, while dynein enables retrograde (towards the cell body) transport. Myosins are actin-based motor proteins that are also responsible for contractile force generation in axons [2, 3, 34, 36, 37].

## 1.4 The role of mechanics in neuronal development

During embryo development, many processes evolve at different time and length scales. All these processes involve forces during the development of the organism. During neuronal development, neurons migrate and extend their processes to find

specific targets. Then, axons grow by interacting with the extracellular environment effected by the pulling force generated by the growth cone after finding its target; axons considerably expand their length, a process called stretch growth [29–32, 45, 46]. Once the connection has been established, tension is regulated along the axons. Changes in the brain tissue stiffness with age suggest that during development, the mechanical properties of nervous tissue are prone to alterations [31, 32, 47].

After the first observation by Weiss that nerve tissue advance and generate tension [48], Bray showed that growth cone could exert mechanical tension and there is a correlation between axonal tension, and its diameter [45]. Bray also shows that mechanical tension can initiate new neurites from cell bodies [29] and later confirmed by the Heidmann group [49]. This group also showed that advance in the growth cone, which leads to neurite elongation, is associated with an increase in neurite tension, whereas stable growth cones have no change in tension [47].

Mechanical tension plays a significant role in the formation of the synapse, and its functioning. *In vivo* experiments on fly neurons suggest that tension along axons can be actively regulated by neurons. It is even involved in synapse functioning. Mechanical tension act as a signal to modulate vesicle accumulation and synaptic plasticity. In a recent study [50], axon attached to the substrate is stretched along the axon, and the accumulation of synaptic vesicles is quantified. The stretched axon exhibits increased vesicle accumulation at the synapse. It also modulates local and global vesicle dynamics [50]. Clustering at neuromuscular junctions increases when axons are stretched mechanically using micro mechanical force sensors by pulling the postsynaptic muscle. The clustering of neurotransmitter vesicles at presynaptic terminals at the neuromuscular junction depends on the mechanical tension in neurons [51, 52]. Hence, mechanical tension in and along neuronal axons might contribute not only to neuronal network formation but ultimately also to the regulation of neuronal function [32].

This mechanical tension is regulated, and it can regulate many physiological processes in the neurons and might be important in long-distance signaling. The role

of mechanical tension in neurons is well studied, but their internal mechanistic details are poorly understood [3, 31, 32].

In recent times growing experimental evidence suggest that mechanical tension plays an important role in the growth and retraction of neurons [8, 29, 45]. The recent development in experimental techniques made it easier to quantify mechanical tension in neuronal mechanics [11, 12, 53, 54].

## 1.5 Investigation of the axonal mechanical response

The first quantitative measurements are performed by the Heidmann group on PC-12 neurites [9]. They have used calibrated glass micro-needles to measure forces on PC-12 neurites. They showed a linear dependence of tension and change in length of neurite in cultured PC-12 neurites. They also report the rest tension of a few hundred pN. Their experiments using destabilizing drugs such as Latrunculin-A and Nocodazole suggest that microtubules are under compressive load [9]. In another study, they showed that axons actively regulate their tension [30].

Saif group did force measurements *in vivo* on *Drosophila* neurons. By studying the mechanical response of *Drosophila* neurons using high-resolution micromechanical force sensors, they showed that axons behave like elastic springs showing a linear force-deformation relationship. After the application of deformation, force relaxed to a steady-state value. They also shown that axons exhibit a rest tension 1-13 nN. The axons actively generate force and regulate their tension once release from the taut state [11].

Experiments on fly and chick neurons show that axonal contraction is an ATP driven and myosin-II dependent process. They have shown that axonal contraction is affected by ATP depletion, disruption of actin filaments and inhibition of myosin-II motors [55, 56]. These studies suggest that acto-myosin machinery is primarily involved in the contractility of axons which results in tension generations in axons [55, 56].

### 1.5.1 Physical modeling to understand axonal mechanics

Various experiments show that axons are viscoelastic in nature. Axons behave as a viscoelastic solid-like response due to mechanical stretch [9, 10]. To explain the main observed behaviours of axons, the various model has been developed. In response to fixed stretch, axons can grow, and force relaxes to a steady-state value. Axons can actively regulate their tension in response to stretch [10, 11, 30]. Below is the description of such models based on experimental observations.

The first attempt to measure mechanical tension in PC-12 neurites and chick neurons was made by the Heidmann group using calibrated glass micro-needles [30]. Dennerll *et al.*[30] proposed a mechanical model for the passive behavior of the axon to explain the viscoelastic solid-like response. They applied single distension on neurites and recorded the tension relaxation response as well as the change in length. They observed three-phase behaviors, an initial phase, where a sudden increase in length occurs and a second phase where length slowly reaches a saturation value. They found that axons behave like a passive viscoelastic material. They also showed that axons actively regulate their tension as after releasing from the maximally applied strain, the tension exceeded from the previous tension. At or above threshold tension, axons show lengthening behavior, which is called the "towed growth" phase (third phase). Their model consists of a stiff spring in series with Kelvin-Voight element, which includes relatively less stiff spring and dash-pot in parallel (Fig. 1.5), which explains the passive viscoelastic behavior. To account for "towed growth", they put another growth dash-pot in series with the Kelvin-Voight element.

Bernal *et al.* [10] observed active viscoelastic response along with passive response in PC-12 neurites. They hypothesized that the molecular motors could activate these active contractions [10]. To explain the active contraction observed as shown in Fig. 1.6, they added an extra element in Dennerll *et al.* model to account for the active contraction. By accounting for molecular motors, they were able to explain observed contractile responses of axons. Mechanical response of PC-12 neurites has also been probed using fluid drag force generated within a flow chamber.

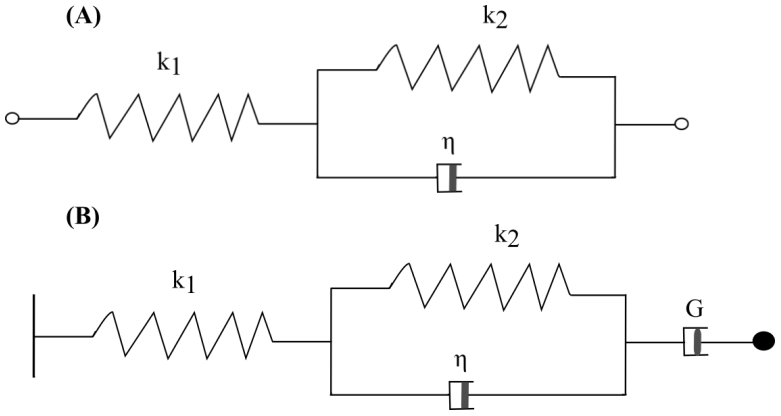


FIGURE 1.5: **Viscoelastic solid model** (A) The figure depicts a viscoelastic solid-like model with a spring in series with Kelvin-Voight element in which a spring parallel to a dash-pot (B) Along with viscoelastic solid-like, the "growth dashpot" is added. This dash-pot allows the axon to elongate above the threshold force and retract when the force is under threshold [30].

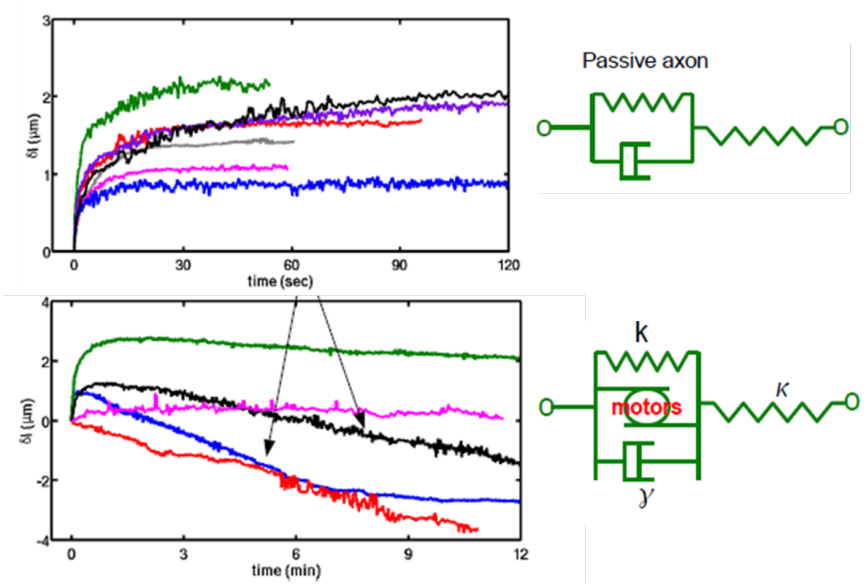


FIGURE 1.6: **Viscoelastic solid model** Bernal *et al.* [10] showed two phases of axonal behavior– passive axonal behavior and active axonal behavior. The mechanical model for neurite behavior with an additional molecular motor element. The model is the same as the mechanical model proposed by Dennerll *et al.* [30] along with an additional element (motors) representing the action of the molecular motors (the figure is adapted from Roberto's thesis [57]).

These experiments also reveal viscoelastic and active responses, and in addition to oscillatory response [58].

Various models have been proposed to explain how axons elongate in response to mechanical stretch. Mass addition during the elongation process is debatable. Growth is thought to either happen at the tip of the advancing growth cone or

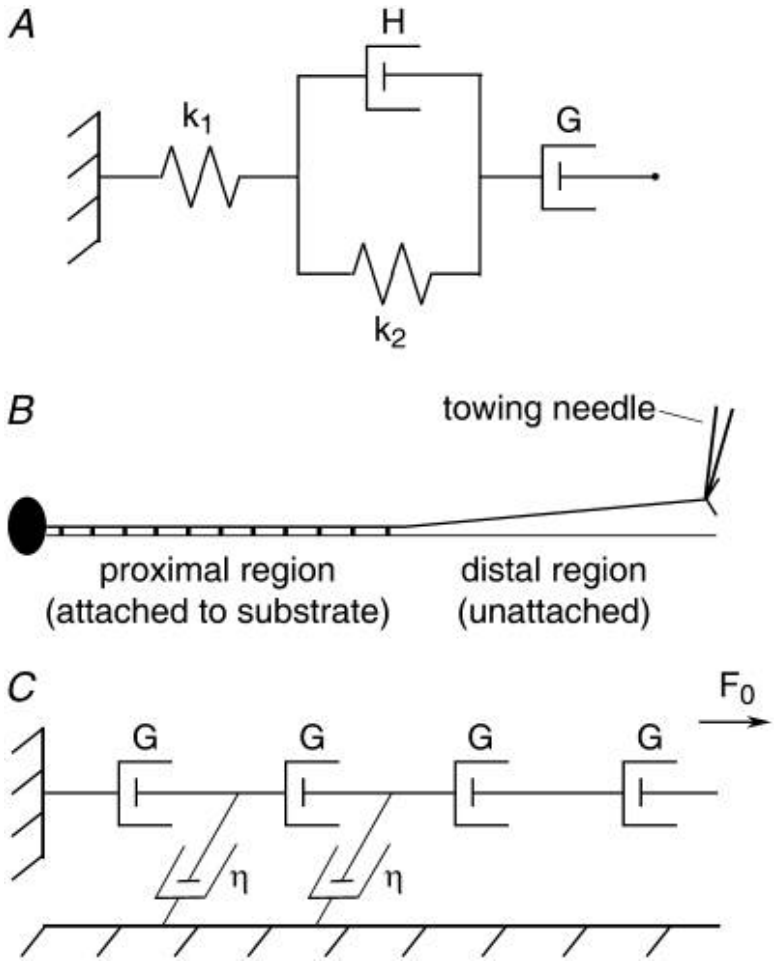


FIGURE 1.7: **Model of a towed neurite as a series of dash-pots**. (A) Considering the axon as a series of Burgers elements. Each element consists of two elastic elements and a free dash-pot (with constant G), which simulates towed growth. (B) Diagram of a neurite during towing. The distal region of the neurite is free of the substrate, whereas numerous adhesions in the proximal region cause the neurite to remain firmly fixed. (C) Under constant tension ($F_0$), the behaviour of a Burgers element is dominated by its free dash-pot. We treat a neurite under constant tension as a series of dashpots. Attachments to the substrate are represented as friction dash-pots (constant $\eta$). Tension is constant in the distal region but is dissipated by adhesions in the proximal region (The figure is adapted from O'Toole *et al.* [59]).

along the length of the elongating axon– stretch growth. Tip growth models assume that mass addition happens through microtubules polymerizations.

O'Toole *et al.* [59, 60] suggested that axons elongate either by tip growth or by stretching. This depends on the level of force generation at the growth cone, the viscosity of the axon, and the level of adhesions along the axon [59, 60]. The proposed model which is an extension of the Dennerll *et al.* [30] model to the entire axon (Fig. 1.7). In this model, the axon is treated as a viscoelastic fluid, and forces

exerted at the growth cone are dissipated by adhesions along the axon. This study explains how tension causes axonal stretching in addition to elongation along with each point of the axon. This model captures the effect of tension generation at the growth cones and dissipation of tension along the axons due to the adhesion of extracellular substrates [59, 60].

The axonal response due to mechanical stretch can be summarized as follows– axons behave as spring-like at short times ($\sim$ few seconds), viscoelastic solid and active at intermediate times ($\sim$ tens of minutes) and growth ("fluid-like") at long times ($\sim$ hours) [9–11, 59, 60].

## 1.6 Relevance of current study to axonal mechanics

Although having such a wide variety of studies on neuronal cells, the role of different cytoskeletal elements of the axonal cytoskeleton to axonal mechanics is poorly understood. We have developed a custom-built force apparatus which has advantages over existing glass micro-needles. The force device work in control mode using a feedback mechanism, which enables us to do either strain controlled measurements or controlled tension measurements. Using this force device, we have probed axonal mechanics and quantified the role of different cytoskeletal components due to mechanical stretch. We have shown that spectrin is a new contributor to axonal mechanics than other cytoskeletal filaments such as microtubules. We investigated the role of the actin-spectrin skeleton in axonal mechanics, which shows a prominent role in protecting neurons from mechanical stretch via reversibly unfolding the spectrin repeated domains.

# Chapter 2

# Instrumentation

## 2.1 Introduction and Motivation

This chapter describes the enhancements and various applications of custom-built force device Micro-Extension Rheometer (MER) [1]. The Force device (MER) was extensively used throughout the thesis for force measurements on systems such as Neurons and Social Spider Silk. The force device was modified and advanced to implement numerous rheological protocols such as step strain, successive step strain, successive step strain along with oscillations, cyclic strain, ramp, etc. to measure mechanical properties of neuronal cells and spider silk strands.

A variety of force measurement techniques enabled the exploration of mechanobiology/cell mechanics [61]. In the mechanobiology field most widely used force devices include Atomic Force Microscope (AFM) [62], optical tweezers [63], optical stretchers [64], and magnetic tweezers [65]. Apart from these, several other techniques are available to measure forces on cells. In particular, calibrated glass micro-needles were developed to measure forces on neuronal cells [10, 30].

Depending upon the mode of measurement, these devices, such as AFM and optical tweezers, can control either the force or the strain. These devices have several advantages and disadvantages, depending on the mode of application.
In this chapter, I will begin by discussing the calibrated glass micro-needles technique in contrast to Micro-Extension-Rheometer.

## 2.2 Overview of Glass Micro-needle Technique

Glass micro-needles were used for force measurement on neuronal cells (see Fig. 2.1). In this technique, a tapered long glass needle with a sharp tip was calibrated and used for force measurement [9, 10]. The micro-needle technique is especially of good use in case of pulling on cylindrically symmetric objects. This technique has been widely used by many groups to explore the mechanical properties of axons, where the axons can be stretched at different rates or can be subjected to step deformations with the help of a step motor and the force relaxation can be observed [9, 10, 59, 60]. In the micro-needles method, the cell extension has to be measured by optical microscopy. Due to this limitation, the controlled force or extension measurements are difficult to perform. This also has poor precision in position determination. Measured forces in axons using micro-needles were from sub nN to few nN and extensions of few microns to few tens of microns.

There are few disadvantages with micro-needles which are as follows –
1. The recorded video should be processed for calculating force on the neurons, which can be time-consuming.
2. There is no direct interfacing, so implementation of feedback to control either the force or strain algorithm is not possible.

## 2.3 Advantage of Micro-Extension-Rheometer over Micro-needles

The basic principle of the Micro-Extension-Rheometer is similar to that of the glass micro-needles technique. The Micro-Extension Rheometer (MER) has several advantages over the glass micro-needle technique, as well as several other techniques in the mechanobiology field. The MER overcomes the disadvantage listed above. The MER is an optical fiber based force transducer, which uses an optical fiber as a cantilever, the light exiting through the tip of the fiber is tracked to know the current position of the sample which enables to apply the control feedback mechanism. The second advantage is that the sample deformation can

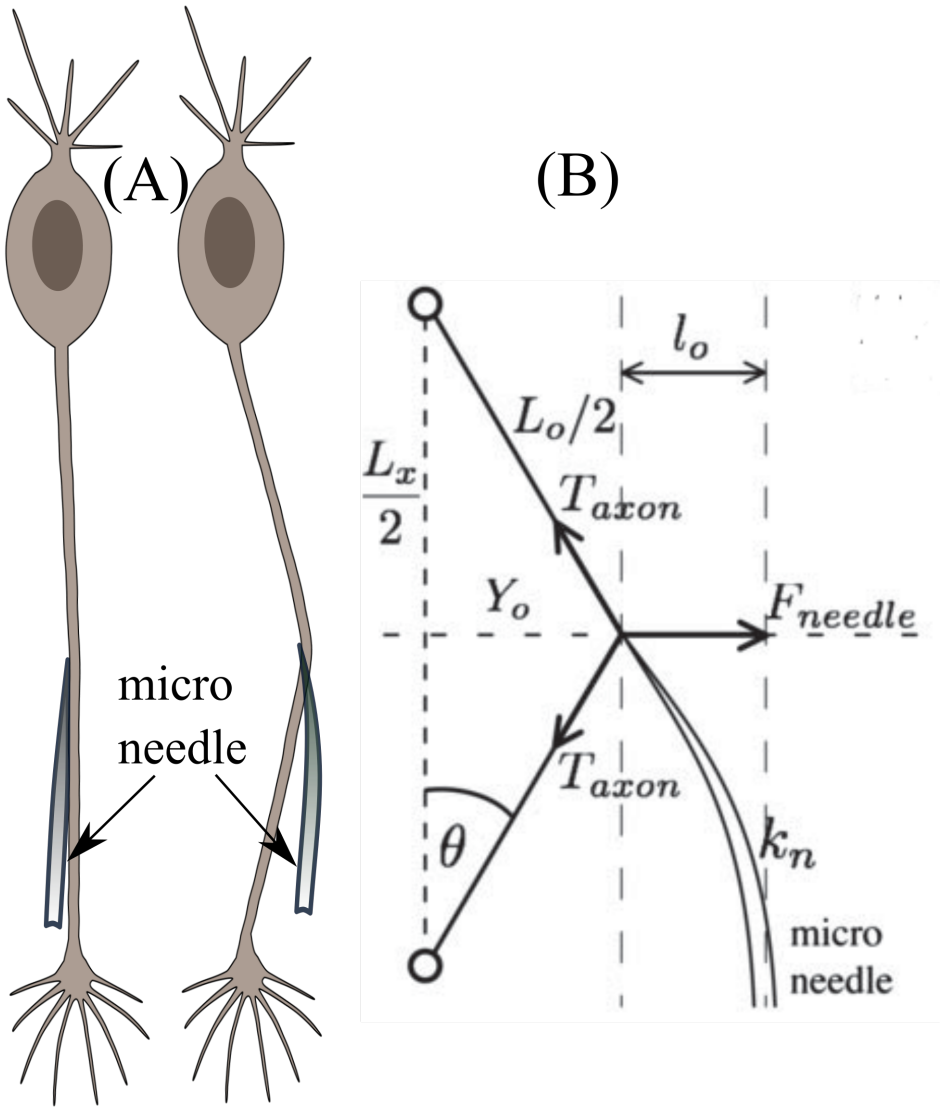


FIGURE 2.1: **Stretching of axons using Micro-needles** (A) schematic of axon stretching using calibrated glass micro-needles and the deflection in the needle which is used to calculate the force on the axon (B) schematic showing the calculation of tension on an axon (adapted from Bernal *et al.* 2007 [10]).

be imaged during the application of deformation to the sample, and the same can be recorded. The system can also enable us to do fluorescent imaging while measuring the force on the sample. Apart from this, the MER has advantages over other devices as well. For example, in AFM, the sample deformation can not be imaged simultaneously while force is applied to the sample. In optical tweezers,

one is limited by the range of forces that can be applied to the sample, which are sub-pico-newton to few hundreds of pico-newton. The force device (MER) has the potential for numerous applications to soft matter physics and mechanobiology because of its wide range of measuring force capabilities from few mN to up to a few pN.

## 2.4 Working principle of Micro-Extension-Rheometer (MER)

The MER is an optical fiber based force transducer. The MER uses an etched optical fiber as a force-sensing cantilever. It consists of a cylindrical glass cantilever of a 125 μm in diameter, single-mode (632.2 nm) optical fiber (P1-630A-FC, Thorlabs Inc.). The length and diameter of the cantilever can be adjusted to achieve the desired stiffness depending on the experimental requirement. The uniform cylindrical cantilever was obtained by uniformly etching the cantilever with the help of Hydrofluoric acid and slowly rotating magnetic stirrer in a cylindrical jar. The length of the cantilever is measured using vernier calipers, and the diameter of each cantilever is measured using an optical microscope and its force constant determined by treating it as a perfect cantilever [1]. The fiber was cut using a scalpel to get a perfect tip. A photograph of the MER is shown in Fig. 2.3.

The base of the cantilever was attached to a closed-loop linear piezoelectric drive (P-841.60, Physik Instruments), which has an accuracy of 1 nm and a travel range of 94 μm. The piezo was mounted on a Zeiss AxioObserver D1 (Carl Zeiss GmbH) microscope with the help of a joystick operated XYZ-stage (XenoWorks, Sutter Instruments) (see Fig. 2.2 (a)). The tip of the cantilever is focussed as a bright spot through the microscope when laser light is coupled into the fiber. The position of the tip of the cantilever is measured with a resolution of 35 nm and 70 nm in 40× and 20× objectives respectively by focussing the laser light exiting through the tip of the fiber on to a Position Sensitive Detector (PSD) (S2044, Hamamatsu). The cantilever tip and the sample were imaged simultaneously using a microscope. The sample was illuminated by the green light of the microscope. The green microscope illumination light and the red laser light were separated using appropriate filters to

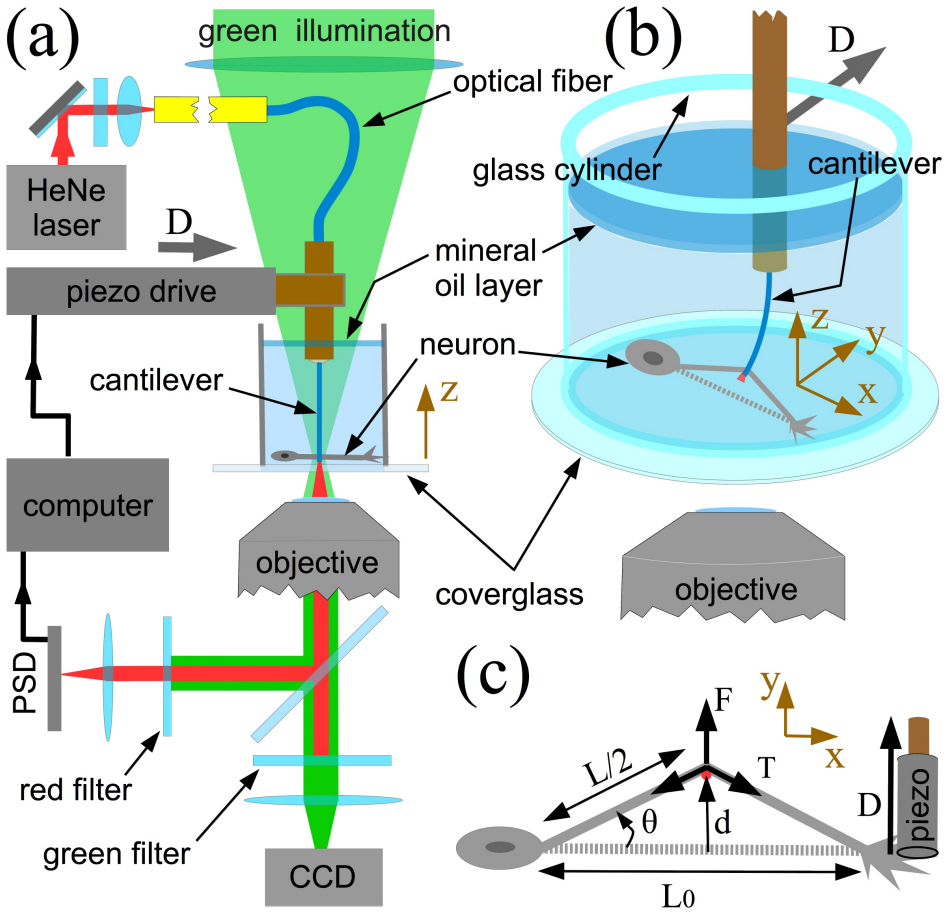


FIGURE 2.2: **Schematic of the force device pulling on a neuronal cell**. (a) The schematic of the home-developed force apparatus that uses an etched optical fiber as a cantilever to stretch axons and to sense force. Laser light exiting the cantilever tip is imaged on to a Position Sensitive Detector (PSD), which in turn is read by a computer. The computer controls a piezo drive via a feedback algorithm to position the base of the cantilever to impose a user prescribed strain function. Simultaneous phase contrast imaging is done using the CCD camera. (b) An expanded view of the cell culture chamber showing the stretching scheme. (c) Illustration of the parameters used in the calculations. The strain is calculated using $L_0$ and $d$, and force on the cantilever as $F(t) = -k(D-d)$, where $k$ is the cantilever force constant. The axonal tension is $T = F/(2sin\theta)$, where $\sin\theta = \mathrm{d}/\sqrt{d^2 + (L_0/2)^2}$.

enable simultaneous force measurements and imaging using a CCD camera (Andor Luca R604, Andor Technology) and 40×, 20× objectives (see Fig. 2.2 (a)).

Axons or silk strands were then pulled laterally at their mid-points by extending the piezo by a distance $D$, as shown in Fig. 2.2 (b), (c). During this process, we ensure that the cantilever and the sample are maintained slightly away from the surface of the coverslip. A feedback algorithm implemented using LabVIEW (National Instruments, v14.0) calculates the strain steps such that there is no

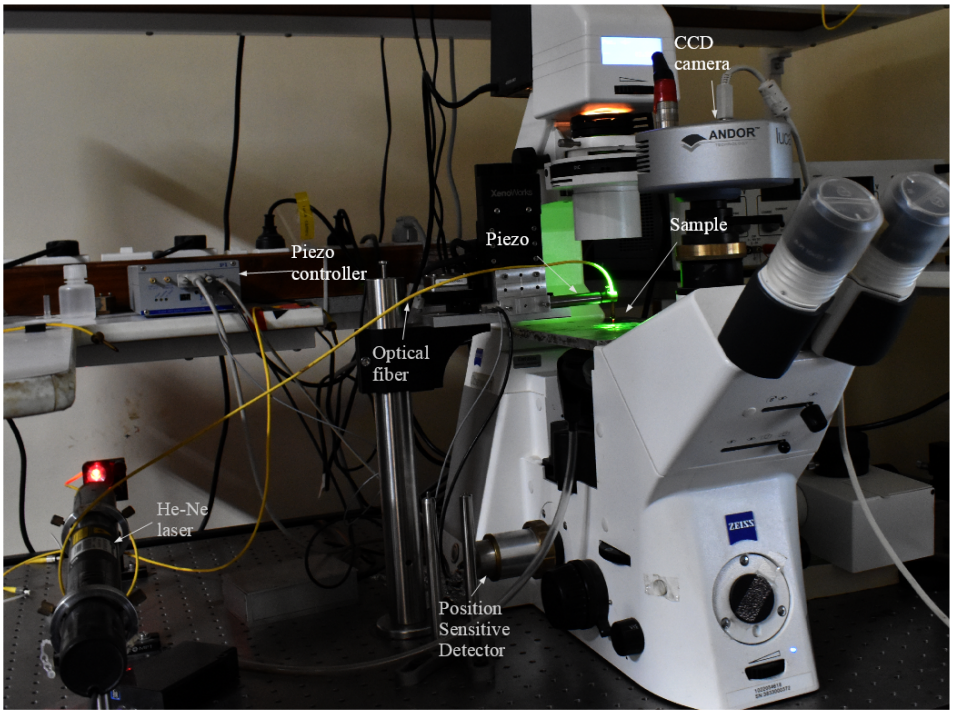


FIGURE 2.3: **Photograph of the setup:** Photograph of the optical fiber based force apparatus Micro-Extension Rheometer (MER) used to investigate the mechanical properties of silk/axon. The piezo drive and the Position Sensitive Detector (PSD) are interfaced to a computer to operate the setup in a feedback strain control mode.

overshoot, and maintains the strain constant for a prescribed wait time after each step. The resulting cantilever deflection was calculated as $D - d$ (see Fig. 2.2 (b), (c)).

The sample strain is calculated from the initial length of the sample $L_0$. The desired strain was calculated from the geometry as $\gamma = \dfrac{\sqrt{L_0^2 + 4d^2} - L_0}{L_0}$. The deflection of the cantilever is calculated as, $\delta = D - d$, where $D$ is piezo displacement, and $d$ is the displacement of the tip of the cantilever obtained from the PSD output. The force on the cantilever is then given by $F = -k\delta$, where $k$ is the cantilever force constant.

From force relaxation data, the tension along the axon/silk strand is calculated as $T(t) = F(t)/(2\sin\theta)$, where $\sin\theta = \dfrac{d}{\sqrt{d^2 + (L_0/2)^2}}$, $\theta$ is the angle with respect to the initial position, $d$ is the displacement of the tip of the cantilever which is in contact with the sample midpoint, and $L_0$ is the initial length of the silk strand (see Fig. 2.2 (c)).

The force constant is obtained by placing the cantilever in a horizontal position and loading it with small pieces of thin copper wires of known weight. The deflection is measured using a home-built horizontal microscope and a CMOS camera (DCC1545M-GL, Thorlabs Inc.) with calibrated pixels. The camera was calibrated using a standard microscopic scale (Olympus) of known distance. Several measurements were done to get the distance in per pixel.

## 2.5 Implementation of various Rheological protocols

We have developed/implemented various rheological protocols to investigate the mechanical properties of axons and silk strands. In this section, I will discuss the different rheological protocols, which we have implemented for different samples to probe mechanical properties. Starting with without feedback loop experiments to strain controlled experiments.

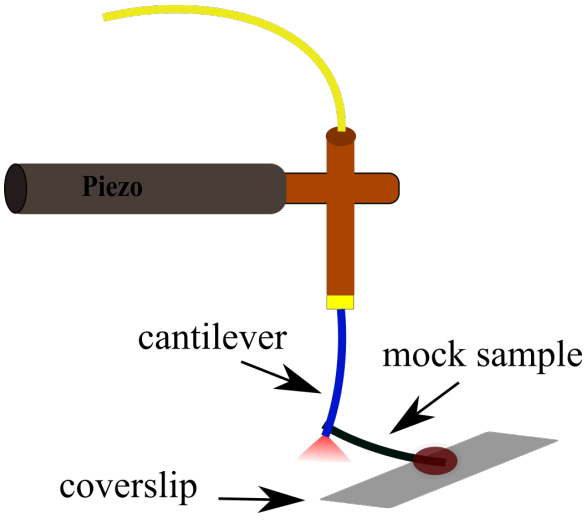


FIGURE 2.4: **Stretching of the mock sample (another piece of optical fiber) using cantilever** The cantilever is pushed against the mock sample that is another piece of the optical fiber glued on the coverslip. All tests are done using this mock sample. The piezo is commanded to move according to various protocols such as multiple steps strain, multiple steps strain along with oscillations, and ramp protocols.

Before implementing these protocols to real experiments, we performed measurements on a mock sample that is another piece of optical fiber. One end of the mock sample is glued on a coverslip, as shown in Fig. 2.4. The cantilever is made in contact with the mock sample, and then various trials on this sample have been

done. The force on the cantilever is given by multiplying spring constant and deflection of the cantilever. Due to force balanced conditions, the force shared by the cantilever and the sample would be the same as given below (Fig. 2.4).

$$F = -k_1.\delta = -k_2.d$$

where $k_1$ is the spring constant of the cantilever and $k_2$ is the spring constant of the sample, $\delta$ is the deflection of the cantilever whereas $d$ is the displacement of the sample. (Note: the spring constant of the cantilever/sample is dependent on the length and diameter of the optical fiber. Here we have used unetched fiber for both the cantilever as well as sample, so the diameter is fixed for both.)

Using this scheme, we tested the various protocols on this sample. We show the multiple step strain, multiple step strain along with sinusoidal osculations and ramp protocol, as well as verification tests for the same.

### 2.5.1 Multiple strain step

In multiple step strain, we have applied a 5 μm fixed sample displacement steps with the help of piezo, which maintains the displacement in feedback mode. The mock sample shows a purely elastic response, and also change in force is the same for every step applied, which is a signature of linear elastic material (Fig. 2.5). Thus, we show that the developed code can apply multiple strain steps and maintains the imposed displacement, as well as can work in feedback mode. The cantilever behaves as a linear elastic material in the range of deflection of few micrometers.

### 2.5.2 Multiple step strain along with small oscillations

Next, we performed multiple strain steps along with oscillations protocol on the mock sample. In this protocol, after a step-strain, a small sinusoidal oscillation of two different frequencies (0.1 and 1 Hz) is superimposed, as shown in Fig. 2.6. The piezo was commanded to maintain the imposed sample displacement along

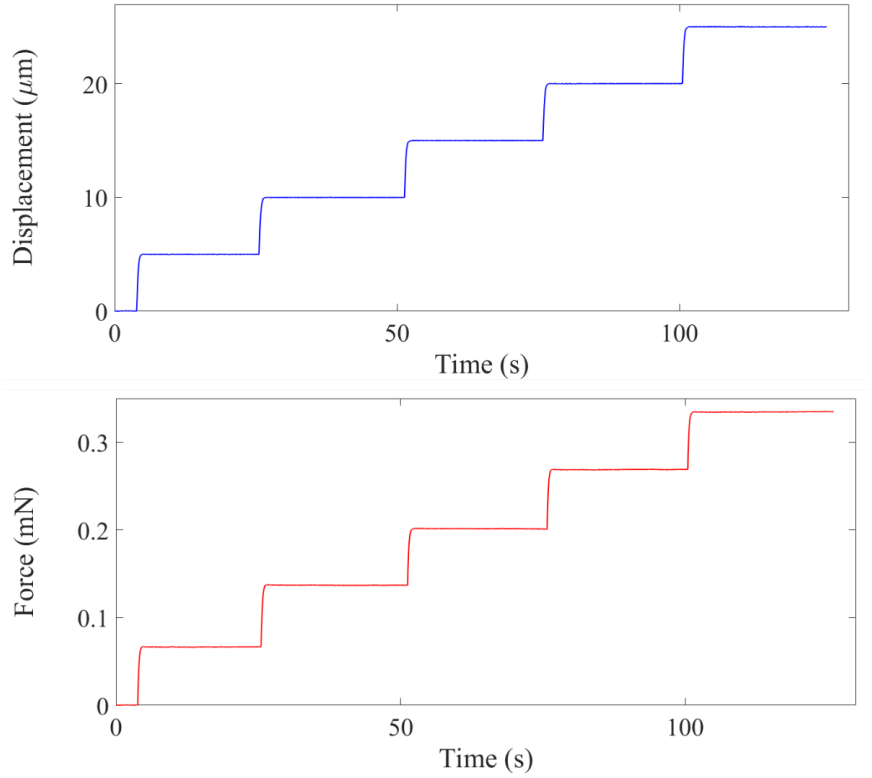


FIGURE 2.5: **Force extension response of a mock sample** Successive steps are applied to the mock sample. The piezo is commanded to maintain a sample displacement of 5 μm for each step in feedback mode. It is evident from the figure that the mock sample shows linear elastic behavior. All protocols were verified by the mock sample before performing the actual experiments.

with sinusoidal oscillations, which is shown in Fig. 2.6. Only a single step is shown here for clarity. For fully implemented protocol on the silk strand, see Fig. 2.14.

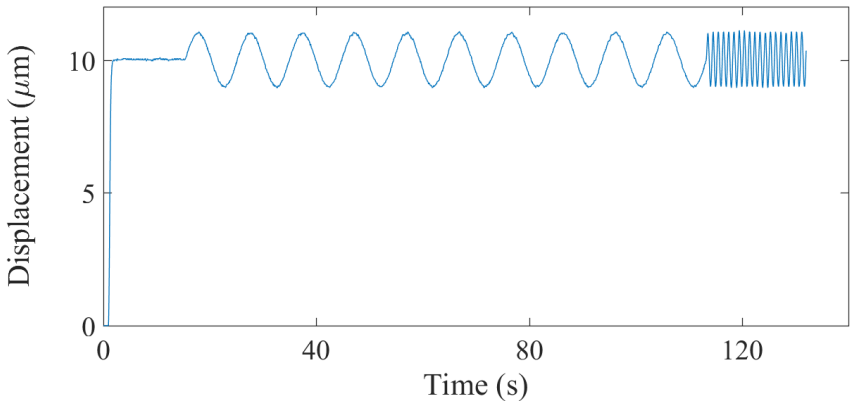


FIGURE 2.6: **Imposed sinusoidal oscillations** Applied sinusoidal perturbation of frequency 0.1 and 1 Hz against the mock sample. The figure shows the sample displacement after the imposition of sinusoidal oscillations.

The mock sample was used to test the nature of the imposed sinusoidal waveform in Fig. 2.6. To test that applied perturbations are perfect sinusoidal oscillations, Fourier transform of the time series of the sample displacement shown in Fig. 2.6, is calculated and plotted against frequency shown in Fig. 2.7. The peak of the frequency found to be close to 0.1 and 1 Hz, which are the applied frequencies (see Fig. 2.6). This also indicates the capability of the MER to imposed these oscillations. However, when a frequency above 1 Hz is applied, we could see some aberration in sinusoidal oscillations. The device limited by the application of oscillations between 0.01–1 Hz. At much lower frequency to get a few cycles, the data can be corrupted by the drift, whereas at a higher frequency, the MER is not able to maintain the feedback loop.

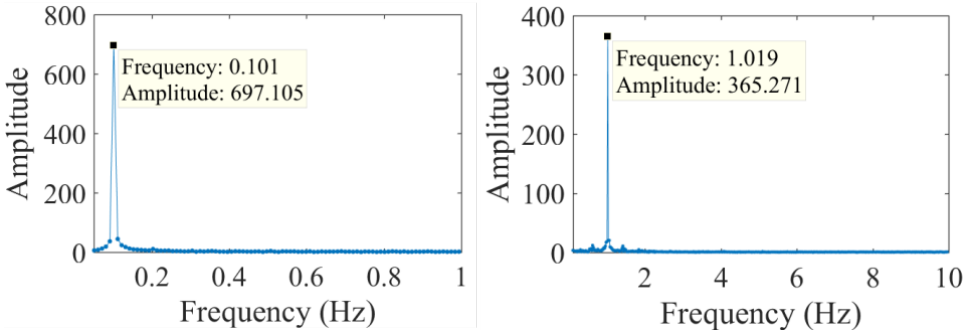


FIGURE 2.7: **Frequency response of applied sinusoidal oscillations** Frequency response of a few cycles of sinusoidal oscillations of sample displacement shown in Fig. 2.6. The frequency response clearly shows a peak at 0.1 and 1 Hz. This indicates that imposed oscillations are sinusoidal oscillations of applied frequency.

### 2.5.3 Ramp protocol

A similar method as sinusoidal oscillations was employed in ramp protocol (triangular wave). First, a step-strain was imposed with wait time to let force relax to steady-state then on top of that triangular wave were superimposed as shown in Fig. 2.8. The protocol is then used to calculate energy dissipated in the loading and unloading cycle. This protocol was extensively used to probe spider silk mechanical responses such as energy dissipation, limit cycle, and stiffening or softening responses were studied (see details in Silk chapter). We have also applied triangular waves of different frequencies (0.01–1 Hz).

To test the nature of the applied triangular wave, the waveform was Fourier transformed. For example, a 0.05 Hz triangular waveform is shown in Fig. 2.8. The Fourier transform shows a peak at 0.05 Hz, as shown in Fig. 2.9, as well as alternative peaks at equal distance of various frequencies, are seen as expected for a Fourier transform of a triangular wave.

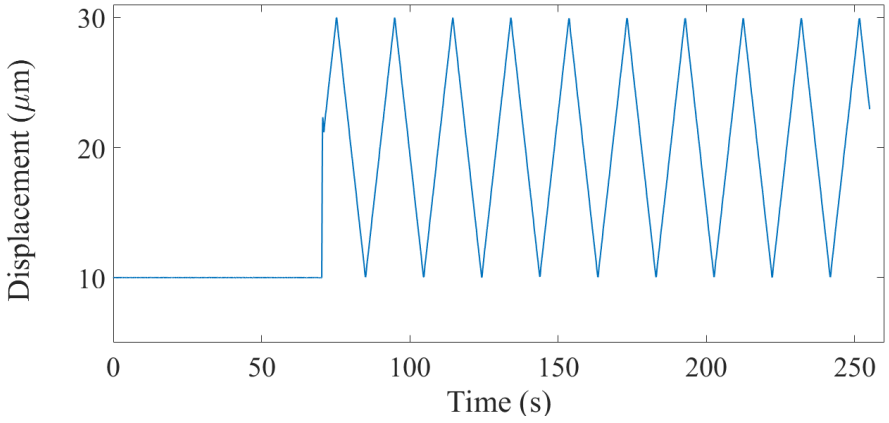


FIGURE 2.8: **Imposition of ramp protocol (triangular waves)** The figure shows a step-strain followed by a ramp (triangular wave) displacement of the sample with a frequency of 0.05 Hz. Corresponding Fourier transform is shown in 2.9.

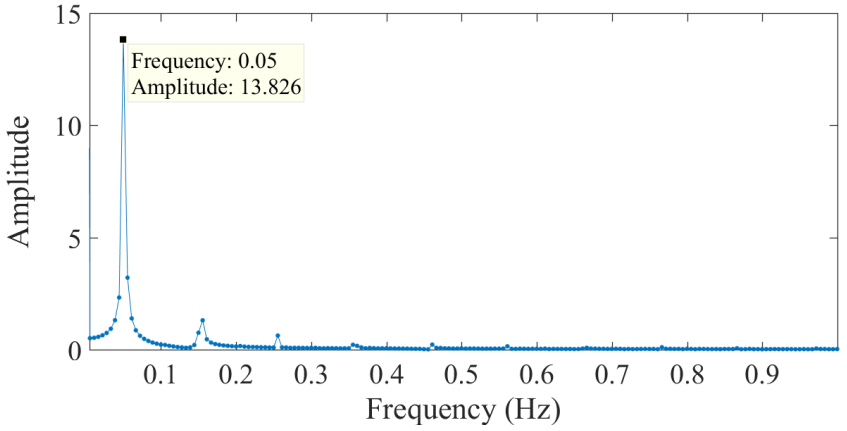


FIGURE 2.9: **Frequency response of ramp protocol (triangular waves)** Frequency response of the triangular wave displacement shown in Fig. 2.8. The frequency response shows a clear peak at 0.05 Hz along with alternatives peaks, which is the signature of a triangular wave.

## 2.6 Implementation of the protocol on axons/silk strands

After successful tests of these protocols on the mock sample, we tested these protocols on real samples, either on axons or on silk strands.

### 2.6.1 Multiple steps without feedback on axons

We first started with developing LabVIEW codes without controlling strain or force. This shows that the MER is capable of doing measurements on axons and reproduces the viscoelastic behavior of axons reported earlier. In this case, the piezo drive was commanded to move a fixed step, and the corresponding evolution of the displacement of the sample (axon) and the force was recorded. The Fig. 2.10 shows the commanded piezo movement with time and evolution of the tip displacement and observed force with time. The force response shows the viscoelastic nature of the axonal cytoskeleton. Note that both sample displacement and force evolves with time after each step. Since the measurement should be in such a way that either force or strain is controlled so that one could study the viscoelastic behaviors of materials like axons and silk strands, we developed an algorithm that either controls strain or force. In the next section, I will show examples of controlled strain protocols that will be used throughout the thesis to study the mechanical properties of axons and silk strands.

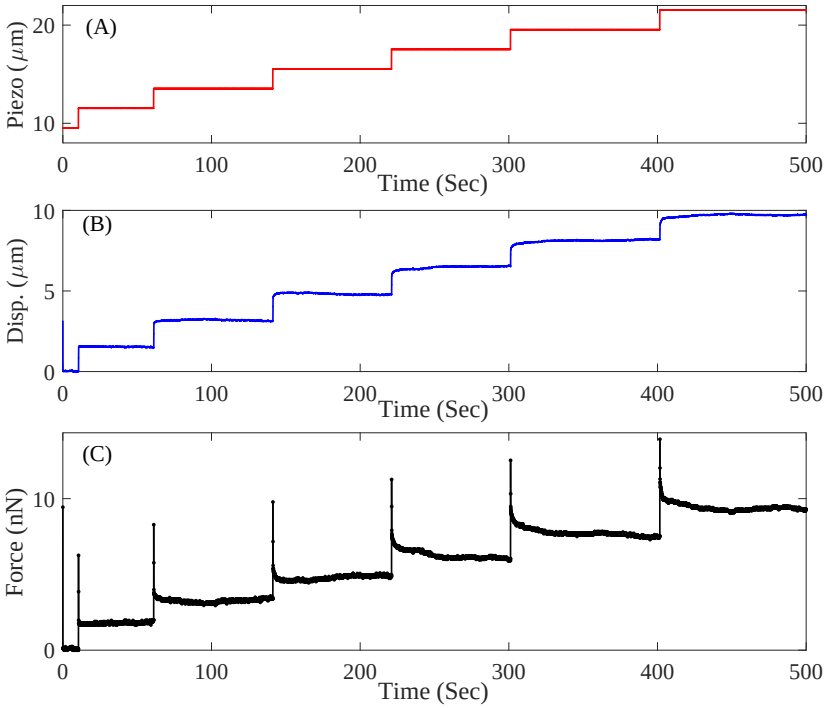


FIGURE 2.10: **Evolution of force in uncontrolled strain** (A) Commanded fixed piezo step of 2 µm each (B) evolution the displacement of the sample (axon) as a function of time (C) evolution of corresponding force which is viscoelastic in nature.

### 2.6.2 Single Step Strain (Controlled strain) on silk strands

In this section, we developed a control strain protocol for samples such as axons or silk strands. The single strain step protocol tells us about the long time behavior of the sample if waited reasonably. This protocol will tell us that the sample behaves as a viscoelastic solid or fluid at long time scales. We have shown later in the thesis that axons, as well as silk strands, show a viscoelastic solid-like response at longer time scales.

In control strain, the piezo is commanded in such a way that it maintains the desired strain by moving forward and backward steps. For control strain, the displacement between the initial cantilever tip position and final tip position should be made constant in a way to achieve control strain. The feedback loop works in proportion mode where $\alpha$; the proportionality constant was optimized for each cantilever before the actual experiment. The controlled variable (strain) is given by— $\alpha.\triangle$[set strain - current strain]. Fig. 2.11 shows the imposed controlled strain and the corresponding evolution of the force. The loop takes about a second to reach the desired strain value. Due to this reason, in all the measurements, we consider the force relaxation data after the strain achieved the desired value. From now onwards throughout the thesis, I have used various protocols in control strain measurement.

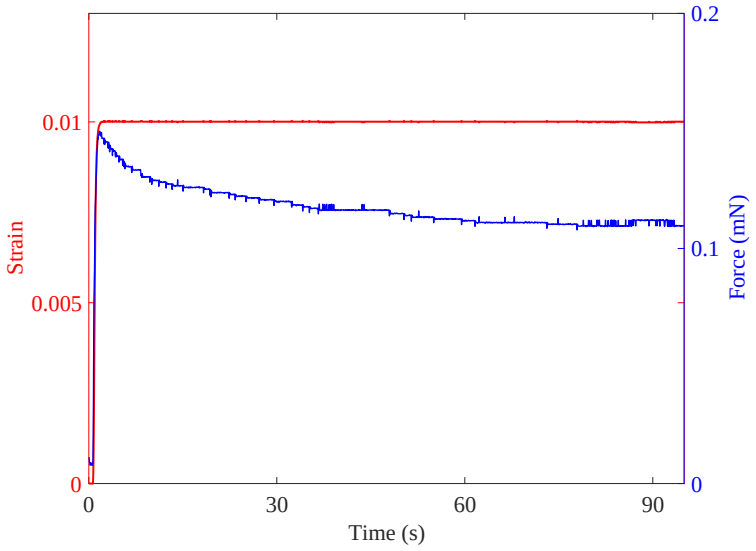


FIGURE 2.11: **Imposition of single step strain** Imposed controlled strain of fixed magnitude with a reasonable wait time and evolution of corresponding force, which is viscoelastic in nature.

### 2.6.3 Cyclic strain on axons

In this protocol, a small step-strain was applied, and top of that repeated cycles of up and down (positive and negative strain) strain-steps were applied, as shown in Fig. 2.12. The initial small strain was applied to avoid any slippage of the axon at zero strain. The cyclic protocol was extensively used to probe the mechanics of axons after perturbing with various cytoskeletal drugs, for example, Latrunculin-A and Nocodazole. The main reason to use this protocol instead of successive strain protocol (described in the next section) is that after the application of drugs, the axons become very fragile and prone to detach easily from the ends. A typical cyclic strain protocol has been shown in Fig. 2.12.

### 2.6.4 Successive strain steps on axons

Successive step strain protocol was developed by keeping in mind to investigate the viscoelastic properties of the sample with imposed strain. In particular, the elastic modulus as a function of strain and relaxation behavior of axons and silk strands. In this protocol, successive strain-steps were applied on top of each other with a reasonable wait time depending on the type of sample (reasonable wait

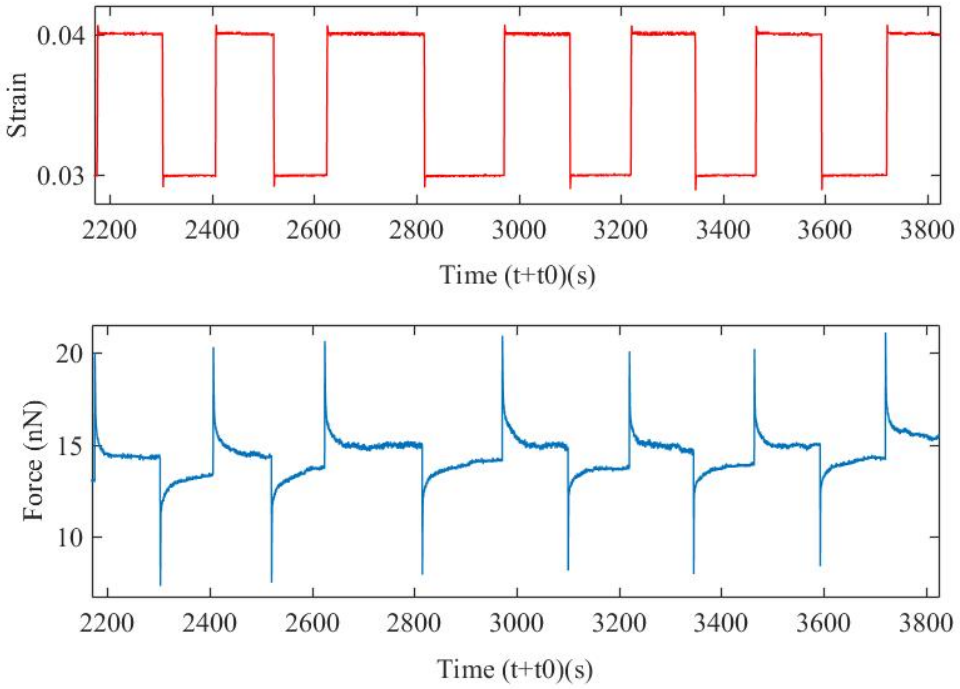


FIGURE 2.12: **Cyclic strain protocol** An example of an axon that was pulled to a strain of 3% and then cyclic strain has been applied over an extended period to show that there is no damage with the number of cycles. This protocol is then used to study the effect of specific cytoskeleton disrupting agents.

time is the time to reach the force to steady state at a given strain). Using this protocol, we can estimate the elastic modulus as a function of strain, relaxation time, which is obtained from tension relaxation data and its dependence on the imposed strain. This protocol also tells about materials behaviors as a stiffening or softening response as a function of the imposed strain. The protocol has been shown in Fig. 2.13.

### 2.6.5 Successive strain steps along with oscillations on silk strands

The successive step-strain along with oscillations protocol, is an advancement of the earlier successive strain-step protocol. In this protocol, after imposition of constant strain, small sinusoidal oscillations were superimposed. We have applied two different frequencies, 0.1 and 1 Hz of sinusoidal oscillations. The advantage of this protocol over the successive strain step is that pre-tension of the strand is not needed to calculate the moduli. Thus, irrespective of the pre-tension, one can

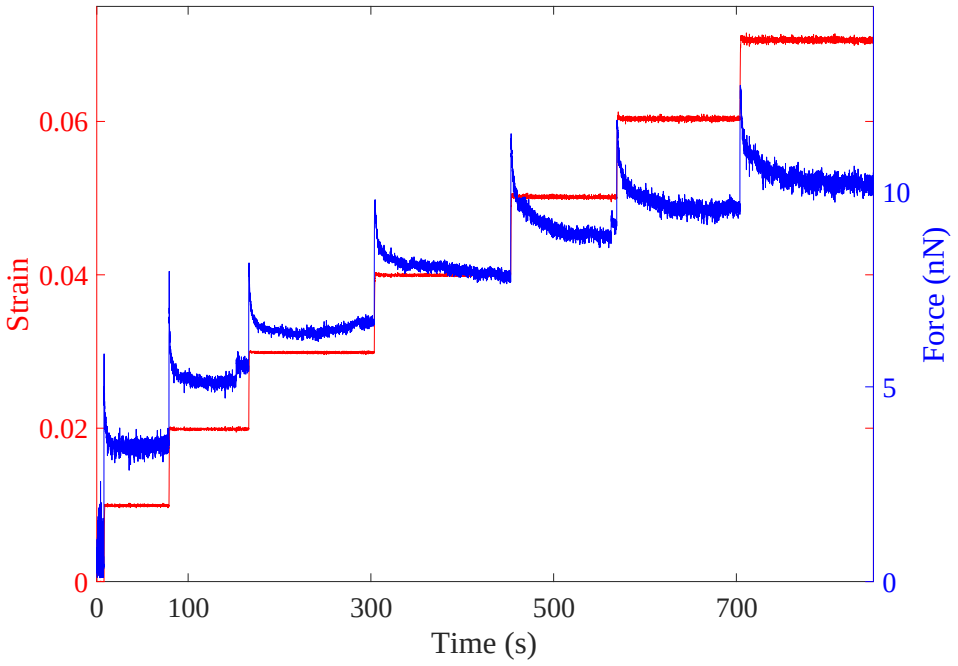


FIGURE 2.13: **Evolution of force in controlled strain (Successive strain-steps).** Imposed controlled strain of fixed magnitude with a reasonable wait time and evolution of corresponding force, which is viscoelastic in nature.

calculate the moduli from the small oscillation data described below. As will be elaborated in a later chapter, this protocol helped us to determine the moduli in high strain regime apart from the small strain regime. The second advantage of this protocol is that one can know the frequency dependence of the moduli.

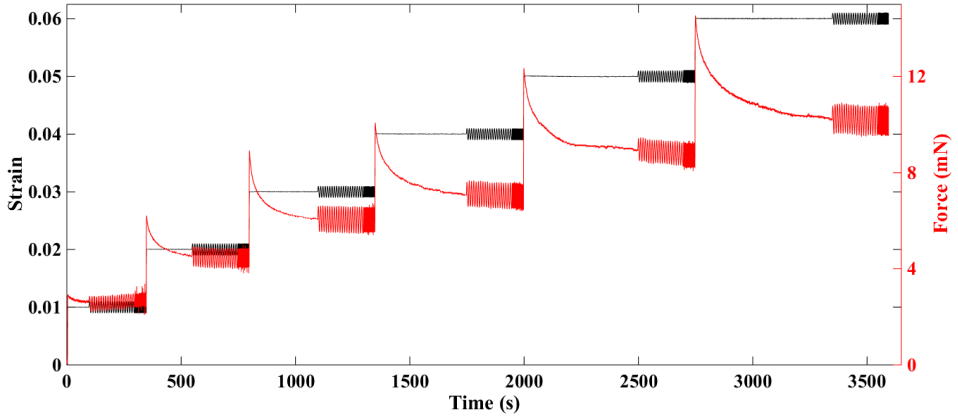


FIGURE 2.14: **Evolution of force in controlled strain along with oscillations (Successive strain-steps).** Imposed controlled strain of fixed magnitude with a reasonable wait time superimposed with small sinusoidal oscillations and evolution of corresponding force, which is viscoelastic in nature.

The tension $T(t)$ obtained along the silk strand as described earlier, we calculate the elastic moduli for different pre-strain values using the small amplitude oscillations as follows. Corresponding to the imposed strain oscillations $\gamma(t) = \gamma_0 \sin(\omega t)$, we obtain stress oscillation as $\sigma(t) = \sigma_0 \sin(\omega t + \phi)$, where $\sigma(t) = T(t)/A$, $A$ being the cross-sectional area of the fiber. The storage moduli for different strains can be obtained as $E'(\gamma) = \frac{\sigma_0}{\gamma_0} \cos(\phi)$, and the viscous moduli as $E''(\gamma) = \frac{\sigma_0}{\gamma_0} \sin(\phi)$.

## 2.7 Conclusion

In this chapter, we have developed various rheological protocols to investigate the mechanical properties of neuronal cells and spider silk. We have successfully implemented many protocols that are used in the next chapters to study various rheological properties. We have tested these protocols on mock sample as well as on real samples. The development of these protocols enables us to investigate neuronal cell mechanics and spider silk mechanics in the way which was not possible before.

# Chapter 3

# The role of different cytoskeletal elements in axonal mechanics

## 3.1 Introduction

Mechanical tension plays an important role in the development, growth, and motility of cells. In neurons, the mechanical tension has importance in neuronal growth, its function, and guidance [2, 31]. The thin tubular extensions of neurons, called axons, can be a meter long in a human body. Axons extend long distances to communicate with other cells. A growing axon or post-synaptic axon can be under tension [2, 3, 49]. During embryo development, as the size of the organism increases and the expansion of the surrounding tissue generates tension in the axon, in response, axons get stretched, and the length of axons increases [66].

The axonal cytoskeleton has a unique organization. The axonal cytoskeleton has three main types of filaments, microtubules, actin, and neurofilaments. These filaments respond to externally applied stimuli and rearrange themselves [3]. The axonal cytoskeleton has an axi-symmetric structure with a central core of bundled microtubules arranged in a polar fashion and cross-linked by associated proteins. The core is surrounded by neurofilaments and a membrane-associated cortex of cross-linked actin filaments. Apart from these filaments, the cytoskeleton has a myriad of proteins, including motor proteins, which interconnect these structural

elements. Recently, super-resolution light microscopy has revealed a periodic array of actin rings that are interconnected by spectrin cross-bridges beneath the plasma membrane. The actin-spectrin skeleton is thought to preserve the mechanical integrity of axons [7, 41].

The contribution of each cytoskeletal filaments is obtained by measuring the change in cell stiffness or contractile force generation by genetic modifications or by polymerization-depolymerization of the individual filaments. However, the axonal cytoskeleton is a complex structure having these three filaments which are connected by various proteins. These filaments form dynamic networks within the cell with the help of crosslinkers and motor proteins and regulatory proteins that promote filament polymerisation and depolymerisation [2, 34, 35, 37]. The inter-dependencies between these filaments to axonal mechanics are not well understood and hard to dissect. In this thesis, I have used various stabilizing and disrupting drugs to study the contribution of individual filaments.

Several attempts have been made to investigate the role of mechanical tension in neurons both *in vivo* and *in vitro*. To study the axonal mechanical responses, calibrated glass micro-needles have been used to pull on neurites of PC-12 cells as well as on chick neurons. In this study, the evolution of force and change in neurite length has been recorded using video microscopy and glass micro-needle. Axons respond viscoelastically to stretch deformations and can build up excess tension when stretched, presumably due to the action of molecular motors [30]. This suggests that axons can actively regulate their tension. The linear response of axons has been studied most extensively, where a linear relationship between force and extension has been revealed in axons[9, 11]. However, the role of individual filament types in axonal mechanics has not been explored. Contractile tension generation in axons is shown to be an ATP driven and myosin-II dependent contraction. The axonal contraction is affected by ATP depletion, disruption of actin filaments, and inhibition of myosin-II motors suggests that acto-myosin machinery is primarily involved [10, 55, 56, 60].

Despite the observation of such a rich variety of mechanical responses, the structure–function relationships between the different cytoskeletal elements and these mechanical responses are poorly understood. In this chapter, we have used a strain-controlled, home-built optical fiber based force apparatus to probe axonal response due to mechanical stretch. We investigated the non-linear mechanical properties of axons in greater detail using this technique and quantified the contribution of different cytoskeletal components due to mechanical stretch.

## 3.2 Methods

### 3.2.1 Force measurement

Measurements were made using a modified version of the optical fiber based force apparatus [1] and are shown schematically in Fig. 2.2. More details are described in the instrumentation chapter-2. In short, it consists of a cylindrical glass cantilever, 10–20 μm in dia. and 5–10 mm in length, fabricated by uniformly etching the end portion of a 125 μm thick single mode optical fiber. The exact length and diameter of each cantilever are measured, and its force constant determined by treating it as a perfect cantilever [1]. We use the Young's modulus value for the optical fiber obtained by loading test cantilevers by known weights and measuring the tip deflection using a horizontal microscope. The base of the cantilever was attached to a closed-loop linear piezoelectric drive. The piezo was mounted on a microscope using a joystick operated XYZ-stage. The position of the tip of the cantilever is measured with a resolution of 35 nm by focussing the laser light exiting the fiber on to a Position Sensitive Detector. The setup was tested using another cantilever as a mock sample, and this gave the expected linear elastic response. Details of the setup and it's working principle is given in the Instrumentation chapter (chapter-2). Once the cantilever is placed in the container with cells, a drop of mineral oil is added on top of the culture medium to minimize convection currents due to evaporative cooling. Axons were then pulled laterally at their mid-points by extending the piezo by a distance $D$, as shown in Fig. 3.1. During this process, we ensure that the cantilever and the axon (except at the soma and

the growth-cone) are maintained slightly away from the surface of the coverslip. The resulting cantilever deflection was calculated as $D - d$ (see Fig. 3.1C). The axonal strain $\gamma$ is calculated from the initial length of the axon $L_0$. A feedback algorithm implemented using LabVIEW (National Instruments, v14.0) calculates the strain steps such that there is no overshoot, and maintains the strain constant for a prescribed wait time after each step. Axons with initial length $L_0$ in the range of about 100–200 µm were chosen for experiments. The axonal diameter was measured in each case using phase-contrast microscopy.

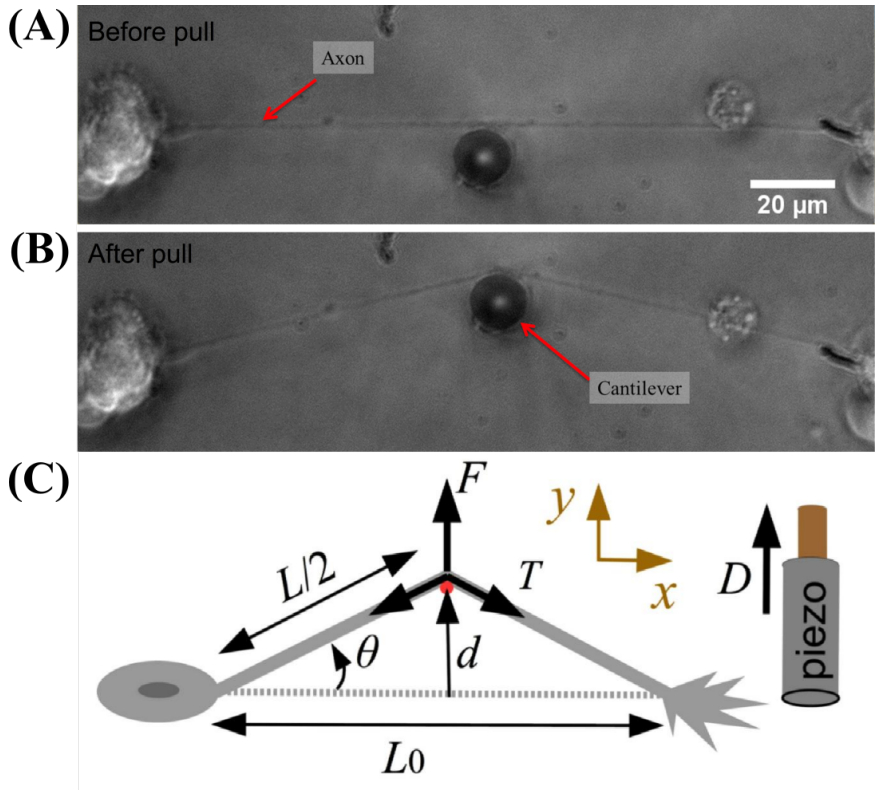


FIGURE 3.1: **Axon pulling scheme. (A) & (B)** Typical images of an axon before and after pulled using an optical fiber. The bright spot is the light exiting through the tip of the cantilever. **(C)** Axon pulling schematic with the illustration of the parameters used in the calculations. The strain is calculated as $\gamma = (\sqrt{L_0^2 + 4d^2} - L_0)/L_0$, and the force on the cantilever as $F(t) = -k(D - d)$, where $k$ is the cantilever force constant. The axonal tension is $\mathcal{T} = F/(2\sin\theta)$, where $\sin\theta = d/\sqrt{d^2 + (L_0/2)^2}$.

There are practical difficulties in performing stretching experiments on primary neurons. The cell body is poorly adherent and can easily move or detach during mechanical perturbations, especially after treating with cytoskeleton modifying drugs. This limits both the range of strain values and the duration of measurements at each strain. For these reasons, we used successive strain steps with a

strain-dependent wait time when probing the non-linear response of the axon and small amplitude cyclic strains for cytoskeleton perturbation experiments. Moreover, active contractile responses to mechanical perturbations and growth cone dynamics can get superposed with the passive force relaxation process. In order to suppress active dynamics as much as possible, we performed all experiments at room temperature (25–26 °C). Axons were chosen such that their entire length was within the field of view, and the data was discarded if either the soma or the growth cone moved during measurement.

### 3.2.2 Cytoskeleton treatments

All cytoskeleton perturbing agents such as Nocodazole (M1404, Sigma-Aldrich), Latrunculin-A (L5163, Sigma-Aldrich), Jasplakinolide (J7473, Thermo Fisher Scientific), and Paclitaxel (Taxol) (T7402, Sigma-Aldrich) were dissolved in DMSO. The final DMSO concentration was kept well below 1% during experiments. The concentrations of these agents are indicated in the text describing these experiments. For force measurement on fixed cells, neurons were incubated for 20 min with a fixative solution of 0.05% (v/v) glutaraldehyde (16200, Electron Microscopy Sciences) and 3.2% (w/v) paraformaldehyde (15710, Electron Microscopy Sciences) in 1X PHEM buffer (60 mM PIPES, 25 mM HEPES, 10 mM EGTA, 2 mM $MgCl_2.6H_2O$, pH 6.9).

## 3.3 Axons exhibit viscoelastic solid-like response

Axons behave as viscoelastic material in response to mechanical stretch [10, 30]. In order to have an idea of its viscoelastic nature at longer time scales and to know the typical relaxation time, we have applied a specified pre-strain and waited for longer times to investigate the axonal behavior. We performed experiments on a few axons with wait time $\sim$ 10 min $\gg$ after a strain step and these results show that the tension relaxation curve indeed decays to a non-zero steady-state value, as shown in Fig. 3.2. For this measurement, we have applied a single step-strain (see instrumentation chapter-2 for step-strain scheme) and waited for forces to

relax over time. We observe that the force relaxes to a steady-state value after a reasonable waiting time. This shows that axons behave as viscoelastic solid tubes at these timescales, as shown in Fig 3.2.

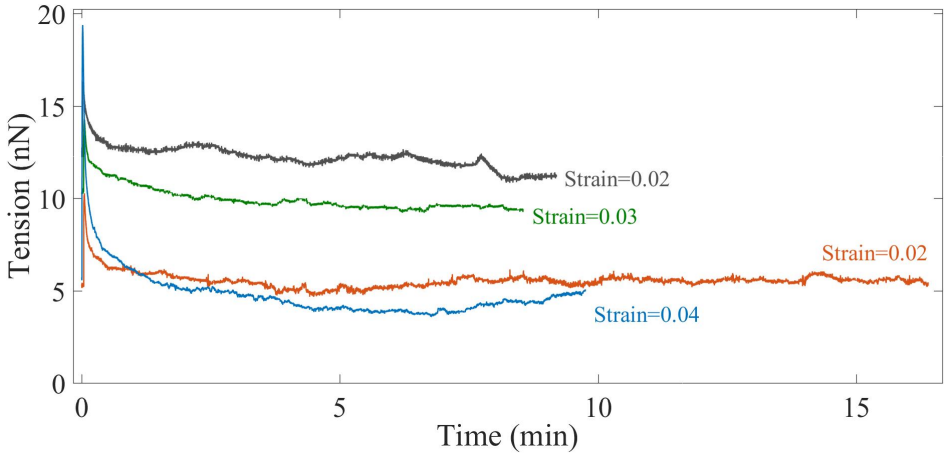


FIGURE 3.2: **Axonal long time viscoelastic behavior** Long time axonal response after the application of a single strain step shows that the tension relaxes to a steady-state value. This shows that axons behave as viscoelastic solid tubes at these timescales ($\sim$ 10 min).

## 3.4 Axons exhibit strain softening response

Axons have been shown to behave as viscoelastically in response to stretch deformation [30]. In response to consecutive step deformations, the only linear response has been studied [11, 49]. Here, using an optical fiber based force device in controlled strain mode, we investigated the non-linear response of the axonal cytoskeleton, which reveals interesting axonal behavior.

In order to study the axonal response as a function of imposed strain, we applied successively increasing strain steps with a wait time between the steps using the home-developed force apparatus (see Fig. 2.2), (the scheme is shown in instrumentation chapter-2) [1].

After each strain step, the strain is held constant using a feedback algorithm. The resulting force relaxation data is shown in Fig. 3.3. Unless specified otherwise, all data are for cells grown for two days *in-vitro* (2-DIV). The observed force relaxation behavior after each strain step is indicative of the viscoelastic nature of the axon,

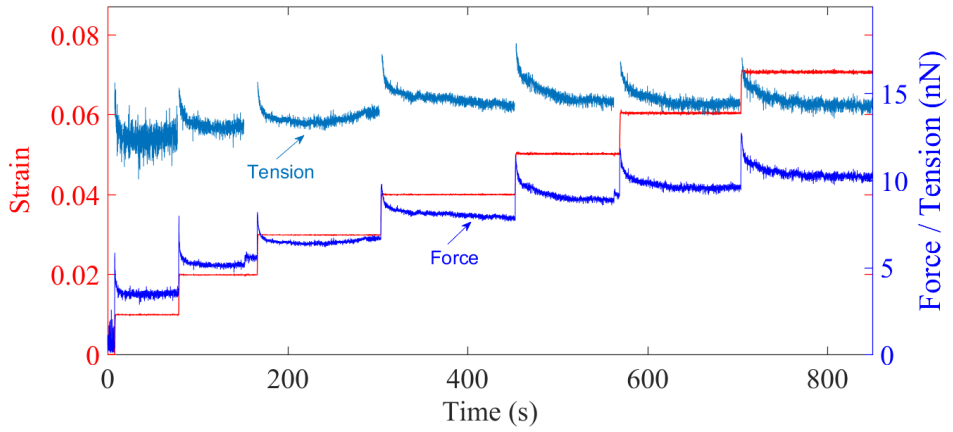


FIGURE 3.3: **Axonal force response** A typical force response (dark blue) of a 2-DIV axon after application to successive strain steps (red). A strain step was imposed and waited for a reasonable time to let forces relax to steady-state, and then another strain-step was imposed. Corresponding to the force relaxation, tension (light blue) was calculated and plotted.

and the dissipative process occurring inside the axon. The origin of the relaxation process is not fully understood. In this chapter, we have explored the role of various cytoskeletal elements to understand the dissipative mechanism happening inside the axonal cytoskeleton and origin of the same. From the data, we can calculate the axonal tension $\mathcal{T} = F/(2\sin\theta)$ (see Fig. 3.1C), where $\sin\theta = d/\sqrt{d^2 + (L_0/2)^2}$, with $\theta(t)$ as the angle with respect to the initial position, $d$ is the displacement of the tip of the cantilever, which is in contact with the axon midpoint, and $L_0$ is the initial length of the axon. The calculated tension plotted in Fig. 3.3 shows that it tends to relax to the same steady state value $\mathcal{T}_{ss}$ as the strain on the axon increases (tension homeostasis). The inset of Fig. 3.5 shows a non-linear response of tension vs. strain while tension saturates with increasing strain, and this trend of $\mathcal{T}_{ss}$ is seen for multiple axons. The occurrence of a steady-state tension (or a steady-state force) is indicative of a solid-like long time behavior of the axons.

### 3.4.1 Determination of rest tension

Axons are under pre-stress (rest tension) even without any application of deformation [11]. A prime example of the same is shown in laser axotomy experiments where axons retract after the cut, which indicates that axons have rest tension at zero strain [67, 68]. In our experiments, to get the rest tension of an axon, we

extrapolate the steady-state tension vs. strain curve to zero strain, as shown in Fig. 3.4. This is done by fitting the data to an equation of the form $-ax^2+bx+c$, which is a simplified form of the tension expression derived from the model presented in the next chapter (Chapter-4). The tension value at zero strain is called the Rest Tension of the axon. The rest tension is used to calculate the effective Young's modulus of the axon, which is described below.

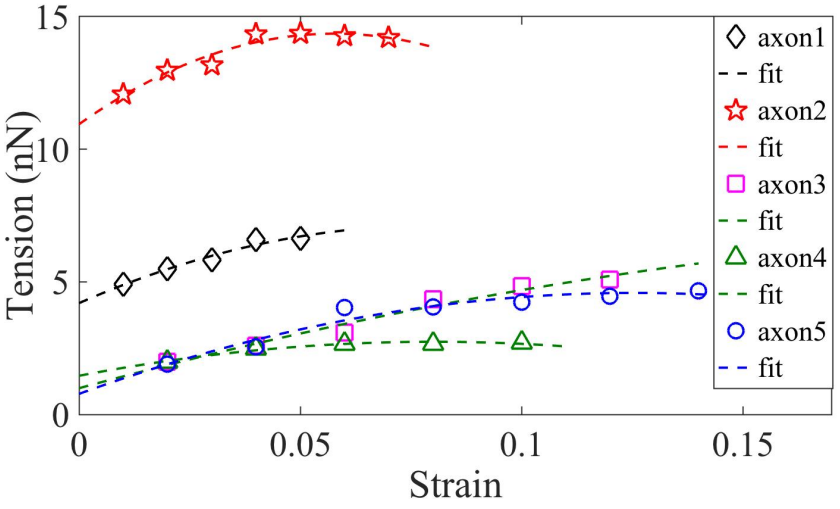


FIGURE 3.4: **Determination of rest tension** Axons are under pre-stress (rest tension) even before the application of any strain. This rest tension can be obtained by extrapolating the tension vs. strain plot to zero strain. This is done by fitting the data to an equation of the form $-ax^2+bx+c$, which is a simplified form of the tension expression derived from the model presented shown in chapter-4.

### 3.4.2 Calculation of elastic modulus

We note that the axonal structure is highly anisotropic and is composed of multiple cytoskeletal structures, and its elastic response is non-linear. Considering extensile deformations alone, we calculate an "effective" Young's modulus $E = (\mathcal{T}_{ss} - \mathcal{T}_0)/(A.\gamma)$, where $\mathcal{T}_0$ is the tension of the axon at zero strain which is calculated by extrapolating the tension vs. strain data (Fig. 3.4), $A$ is the cross-sectional area of the axon (neglecting the change in $A$ with strain), and $\gamma = (\sqrt{L_0^2 + 4d^2} - L_0)/L_0$ is the imposed strain. This modulus is expected to be different from that measured using AFM or magnetic tweezers where the imposed force or strain is radial [69, 70]. The effective modulus data we obtained from multiple axons are shown in Fig. 3.5. More examples (including another set of axons)

are shown in Fig. 3.6, where the modulus is normalized for clarity. Remarkably, the elastic modulus shows a strain-softening behavior, which actually reflects the tendency for tension to saturate with the increasing strain (tension homeostasis) (see Fig. 3.5 (inset)). Moreover, when the axons are released from the cantilever from the maximal strain state, they recover their initial length within 5–10 s. This strain-softening response is not due to any permanent damage or plastic flow as the response remains qualitatively the same when repeated for the same axon. To explore the origin of strain-softening behavior in axons, we have used different stabilizing/ disrupting drugs to know the axonal behavior in subsequent sections. Since, the origin of strain-softening is not known in axons, we have compared our results with other cells such as RBCs, where it shows strain-softening response, and the origin of softening is thought to be actin-spectrin cross-linking which are arranged in a hexagonal structure.

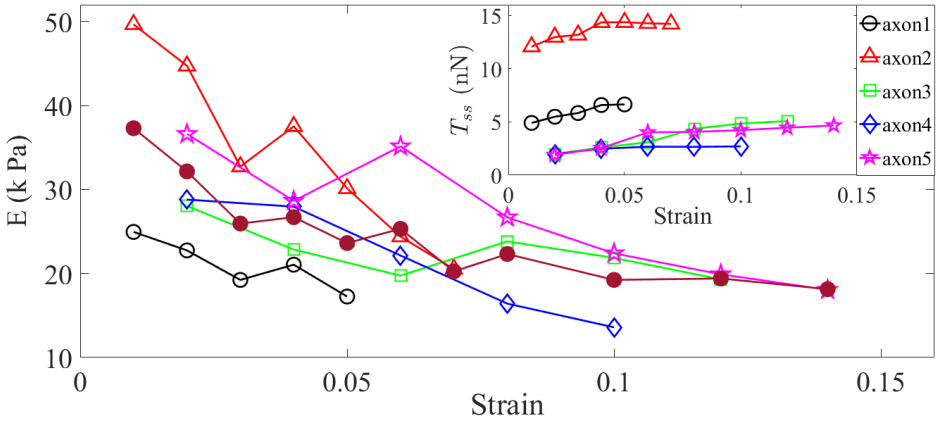


FIGURE 3.5: **Strain-softening in axons** Young's moduli calculated for different 2-DIV axons using the steady-state tension after each step show a strain-softening behavior (the different symbols are for different axons). Only a few representative plots are shown for clarity, and more examples are shown in Fig. 3.6. The inset shows the tension vs. strain plots for different axons. Tension tends to saturate with the increasing strain (tension homeostasis), which leads to the observed softening.

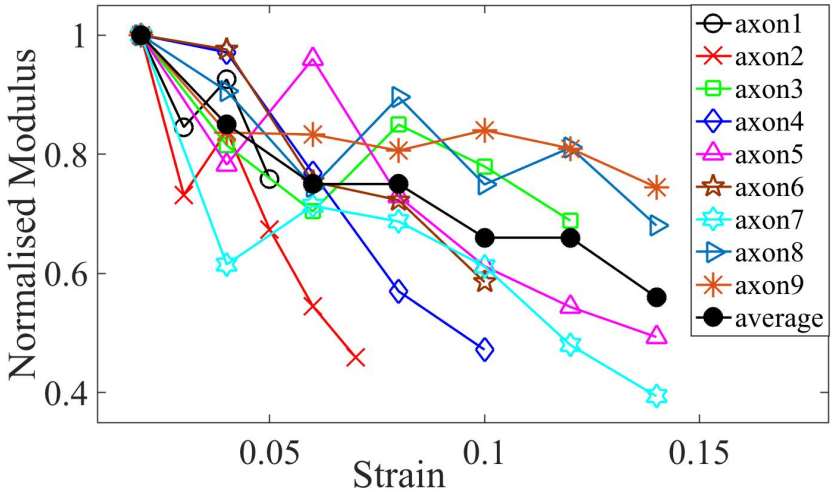


FIGURE 3.6: **Normalized Modulus** Elastic moduli for different axons of age 2-DIV normalized by the rest strain value, which is at 0.02. The plots show the softening of modulus with increasing strain. The average is also shown.

## 3.5 Strain stiffening and softening in other cell types

The axonal response reported here is in sharp contrast with the strain stiffening response exhibited by many cell types [71, 72]. This stiffening has its origin in the entropic nature of the F-actin cytoskeleton and has been observed in purified systems of a variety of biopolymers as well as in cells (Fig. 3.7 A, B) [73, 74]. Fig. 3.7A shows the response of various cross-linked bio-polymers, including actin, vimentin, neurofilaments, etc. while Fig. 3.7 B shows the response of fibroblast cells during the application of stress. The strain-stiffening is also reported in many biological materials such as blood clots, cornea, and assumed that they resist deformation to maintain tissue integrity [75]. Neurofilaments, a major cytoskeletal component of neurons show a strain-stiffening response up to 400% without fail, whereas the actin network fails after a stretch of 20%. This is why it is also thought that neurofilaments are one of the major cytoskeleton components which preserves the mechanical integrity of axons [73]. Since, there is no clean way to perturb or destabilize neurofilaments, quantifying their effect to cytoskeleton mechanics is hard. However, softening observed here is reported to begin even at the smallest strain applied (1%). It is also known that the stiffening response can transition towards a softening response at higher strains, either due to the force induced detachment of transient cross-links or due to buckling of filaments [76–78].

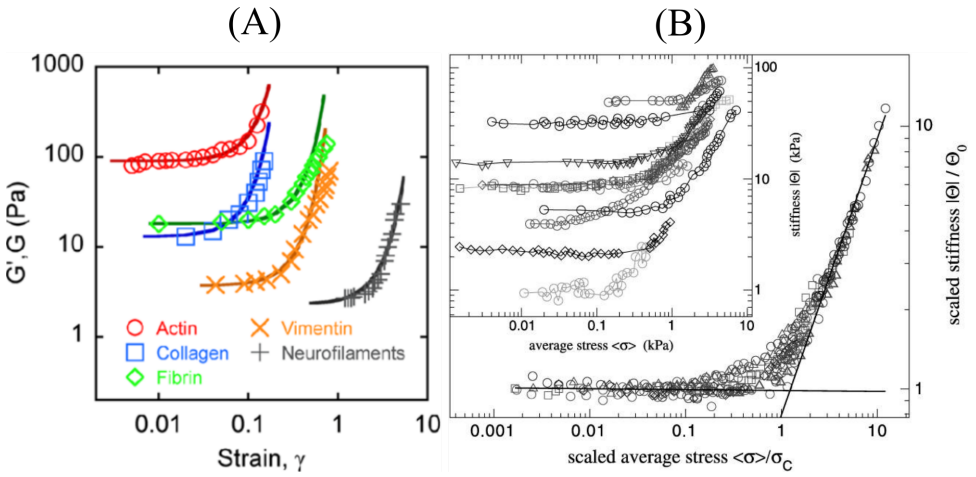


FIGURE 3.7: **Strain stiffening response in crosslinked filaments and cells** (A) The real part, G′, of the storage modulus reduce to the shear modulus G at zero frequency. Data shown are G′ values for F-actin, fibrin, collagen, vimentin and polyacrylamide, and shear modulus G for fibrin and neurofilaments plotted as a function of the dimensionless strain $\gamma$ (the figure and caption adapted from Storm *et al.* [73]. (B) Strain stiffening in fibroblasts cells (the figure is adapted from Fernández *et al.* [74]).

Microtubule bundles alone can account for strain-softening via their cross-linkers (MAPs) exhibit binding-unbinding dynamics or via filament sliding. The filament will slide in response to stretch and, when they detach, the energy stored will dissipate, which can be accounted for relaxation behavior observed. But considering binding-unbinding mechanism, it will give rise to a long time fluid-like behavior because after unbinding, it can bind to another site without having a memory of its initial state [79, 80]. Such a model will not be able to explain the axonal viscoelastic solid-like behavior. The microtubules also go through dynamic instability and become disrupted under dynamic loading. Hence, microtubules can not resist sudden stretch deformation and do not recover easily while released after sudden stretch [21].

Strain-softening is seen in Red Blood cells (RBCs), which is well studied and documented. The softening assumed to be originated from spectrin-mediated elastic behavior. RBCs have a hexagonal actin-spectrin membrane-associated skeleton where short actin filaments are connected to spectrin tetramers [81]. Spectrin molecule has repeated folded units, and these units can unfold under the application of applied force [82]. The softening seen in RBCs is most likely due to the unfolding of spectrin domains under applied force [83, 84].

Our results show that axons exhibit strain-softening without initial entropic stiffening. Direct strain-softening without initial entropic stiffening has been observed in other eukaryotic cells when subjected to a transient stretch. This softening is transient, and if instead a steady-state stretch is applied, the same cells show strain-stiffening response. It shows a transient softening following a fast stretch and release protocol [85]. This is a transient effect and is not reflected in the steady-state modulus of the cell and has been attributed to ATP driven processes, which make the cell behave as a soft-glassy system [86]. The same cells, when subjected to a step strain protocol to measure the steady-state modulus, exhibit strain stiffening [85].

### 3.5.1 Determination of relaxation times

After the application of step-stain, dissipative processes occur inside the axons, and the cytoskeletal components rearrange themselves. To get an insight into how these relaxation processes occur, we quantified the tension relaxation behavior as a function of strain. To obtain the relaxation times, the tension relaxation data corresponding to each strain-step was to fit with different functions. We found that the double exponential function as $\mathcal{T}(t) = A\exp(-t/\tau_1) + B\exp(-t/\tau_2) + C$ fits well, as shown in Fig. 3.8. The steady-state tension tends towards saturation at higher strains show tension homeostasis.

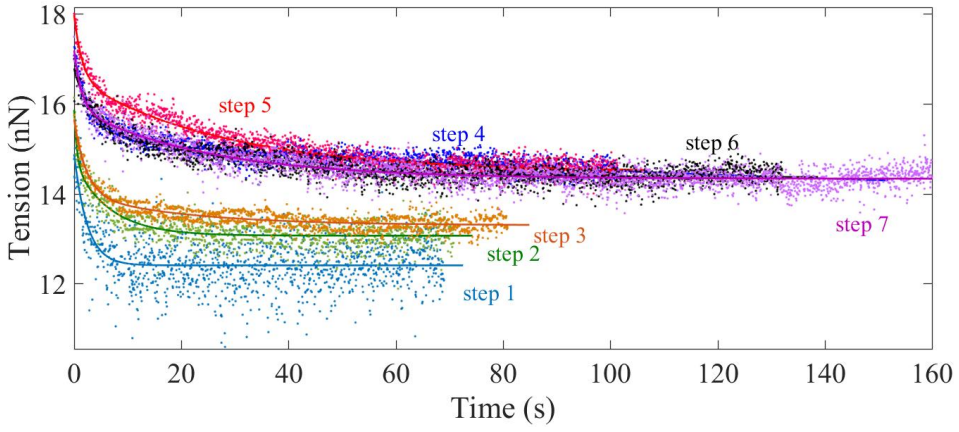


FIGURE 3.8: **Tension relaxation fits** Plots showing double exponential fits to the tension relaxation data from the multi-step experiment (2-DIV axons) using $\mathcal{T}(t) = A\exp(-t/\tau_1) + B\exp(-t/\tau_2) + C)$ where A, B, and C are positive constants and $\tau_1$, and $\tau_2$ are the two relaxation times.

The fitted curves for tension relaxation after each strain-step in Fig. 3.8 were normalized by the tension immediately after each step ($\mathcal{T}_{\text{peak}}$) and plotted together to better illustrate the variation in relaxation time with strain-step. The normalized tension is calculated as $\mathcal{T}_N = [\mathcal{T}(t) - \mathcal{T}_{\text{ss}}]/[\mathcal{T}_{\text{peak}} - \mathcal{T}_{\text{ss}}]$, where $\mathcal{T}(t)$ is the axonal tension, $\mathcal{T}_{\text{peak}}$ is the peak value of tension for each strain-step, and $\mathcal{T}_{\text{ss}}$ is the steady-state tension after the force has relaxed. Closed observation of normalized plots shows that the relaxation times in normalized fitted curves first increase and then decrease at higher strains.

The two relaxation times obtained from double exponential fits as a function of strain, we observe that the relaxation times initially increase with applied strain and later decrease with a peak in relaxation time. The relaxation times show non-monotonic behavior with imposed strain, as shown in Fig. 3.10. The origin and nature of these relaxation times were not known and can unravel interesting phenomena happening inside the axonal cytoskeleton due to mechanical stretch. This unique behavior of relaxation motivated us to explore the axonal mechanics further and helped us develop a model to incorporate these observed behaviors, which is described in the next chapter.

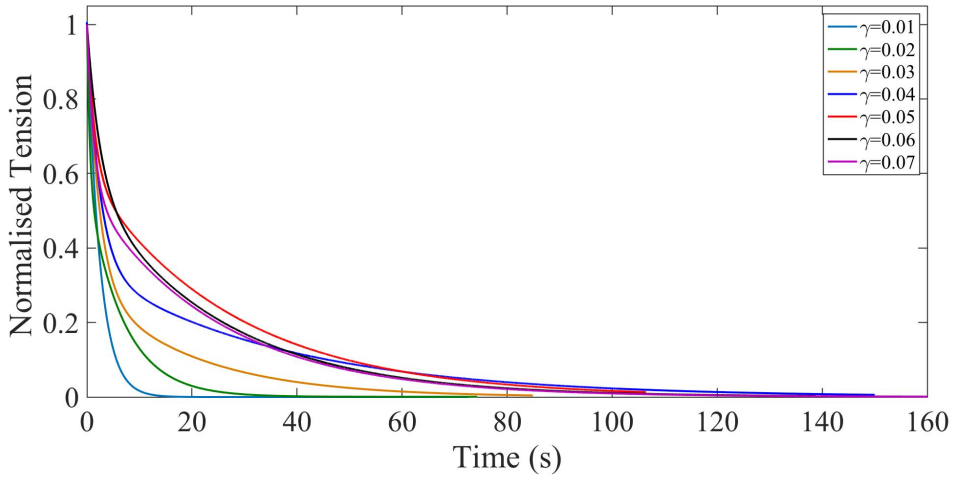


FIGURE 3.9: **Normalised fitted curves for tension relaxation** The fitted curves for the tension relaxation after each step were normalized by the tension immediately after each step and plotted together to better illustrate the variation in relaxation time with step number. The normalized tension is calculated as $\mathcal{T}_N = [\mathcal{T}(t) - \mathcal{T}_{\text{ss}}]/(\mathcal{T}_{\text{peak}} - \mathcal{T}_{\text{ss}})$, where $\mathcal{T}(t)$ is the axonal tension, $\mathcal{T}_{\text{peak}}$ is the peak value of tension for each step, and $\mathcal{T}_{\text{ss}}$ is the steady-state tension after the force has relaxed.

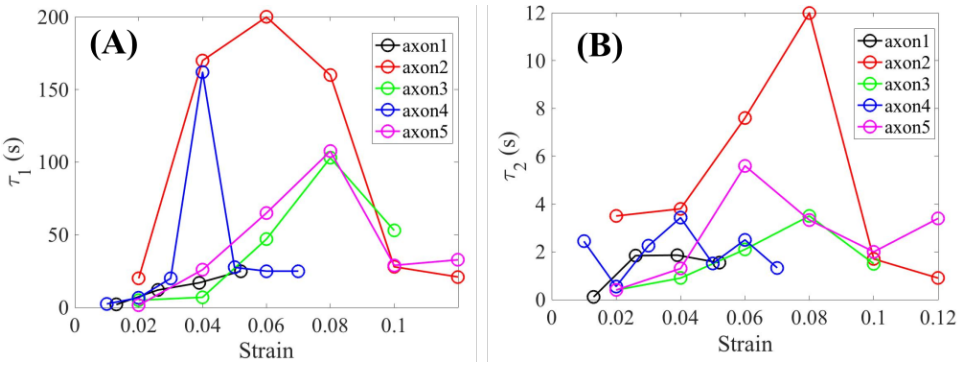


FIGURE 3.10: **Relaxation times** Plot showing the long ($\tau_1$) and short ($\tau_2$) relaxation times as a function of strain for different 2-DIV axons. The relaxation times show non-monotonic dependence on the imposed strain.

## 3.6 The role of different cytoskeletal filaments in axonal response to stretch

After showing that axons exhibit viscoelastic solid-like and strain-softening response. We investigated that which cytoskeletal component of the axonal cytoskeleton would be responsible for the observed behavior. It is known that the axonal cytoskeleton consists of three main types of filaments– F-actin, microtubules, and neurofilaments. In this thesis, we have mainly focussed on F-actin and microtubules. Until now, microtubules are supposed to be the main load bearer in axons because they are in the core of the axon and form a bundle. To probe the effect of these filaments on axonal behavior due to mechanical stretch, we have performed a variety of experiments such as stabilization and disruption of the individual filaments and quantified their effect on the axonal mechanical stretch, which is described in below sections. We have quantified the individual role of these filaments as well as the mixed effect of them.

### 3.6.1 Effect of filament dynamics on axonal response

Since the turnover of cytoskeletal elements, such as actin and microtubules, can be strain-dependent, for example, via the opening of stretch-activated $Ca^{++}$ channels, it is conceivable that the strain-softening response arises due to cytoskeletal remodelling. We first speculated that polymerization and de-polymerization could

be responsible for the strain-softening response due to mechanical stretch. To investigate this, we used stabilizing drugs to probe axonal mechanical response. We first tested the response of axons treated with the microtubule stabilizer drug Taxol, which arrests the microtubules dynamics at 10 μM for 30 min, and the resulting data are shown in Fig. 3.11. The observed force relaxation is qualitatively similar to control axons. The elastic moduli show a strain-softening response similar to normal axons, albeit with higher values of the moduli. To get more insights into the axonal cytoskeleton, we have arrested the dynamics of actin-cytoskeleton.

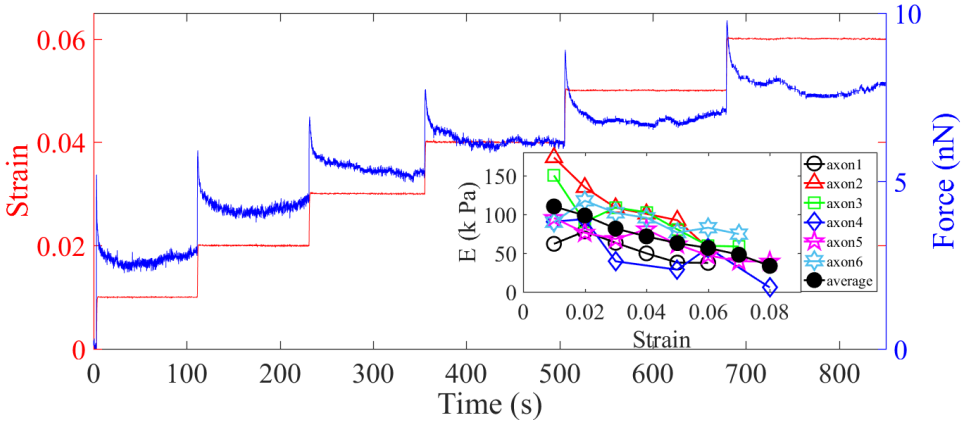


FIGURE 3.11: **Microtubules Stabilization** A typical force response of a 2-DIV axon treated with 10 μM Taxol for 30 min. The inset shows elastic modulus plotted as a function of strain for several axons which exhibit strain-softening behavior.

In order to check whether F-actin dynamics could lead to strain-softening, we treated neurons with 5 μM of the F-actin stabilizing agent Jasplakinolide for 30 min, as shown in Fig. 3.12. F-actin-stabilized axons exhibit a more substantial increase in the elastic moduli compared to Taxol treatment while displaying pronounced strain-softening. Experiments from both stabilizing drugs show that strain-softening is still prominent and elastic moduli higher than that of normal axons, as shown in Fig. 3.13.

Since the stabilization of microtubules or F-actin did not change the strain-softening behavior, we tried a broad, non-specific, and permanent cross-linking of protein-protein bonds using the fixative Glutaraldehyde (see methods), which makes the axon a purely passive material. Glutaraldehyde treated axons showed a much

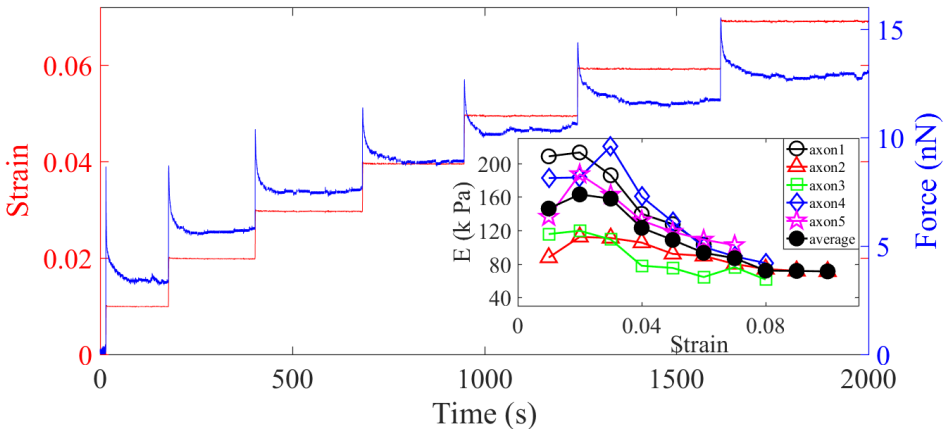


FIGURE 3.12: **F-actin Stabilization** A typical force response of a 2-DIV axon treated with 5 μM Jasplakinolide for 30 min. The inset shows elastic modulus plotted as a function of strain for several axons which exhibit strain-softening behavior.

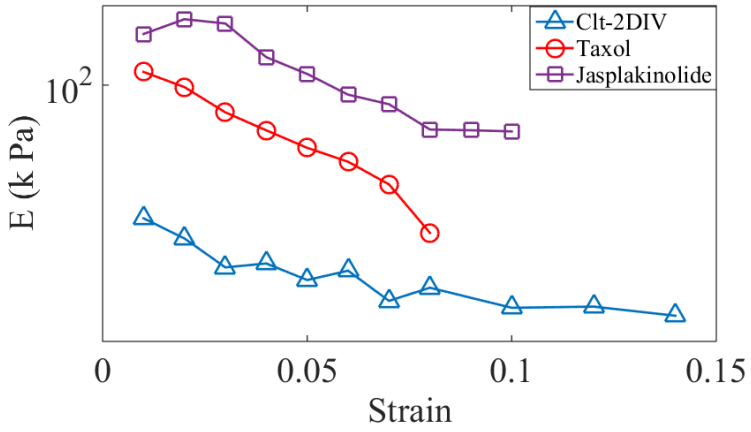


FIGURE 3.13: **Modulus comparison** The average moduli is plotted as a function of imposed strain for control, Taxol, and Jasplakinolide treated axons. The Taxol and Jasplakinolide treated cells still show strain-softening but higher moduli compared to control axons.

larger increase of the elastic moduli compared to normal axons, yet this treatment, too, preserved the softening response of axons Fig. 3.14. When glutaraldehyde treated axons are released from the cantilever from the maximally strained state, they recovered their initial lengths within a second, which is in agreement with the increase in elasticity compared to control axons where the recovery was much slower (∼10 s). The initial few force steps show an elastic response, but towards higher strain, it seems that the cross-linking bonds detach, and correspondingly, we observe a viscoelastic nature of the axonal response. This may be due to after protein fixation bonds need higher forces to unfold. Due to this reason, we observe initial elastic response (no bond unfolding), whereas at sufficiently

high forces, the bonds started to unfold, and we observe the viscoelastic response. The force observed after protein fixation is two magnitudes higher than that of control axons (Fig. 3.14).

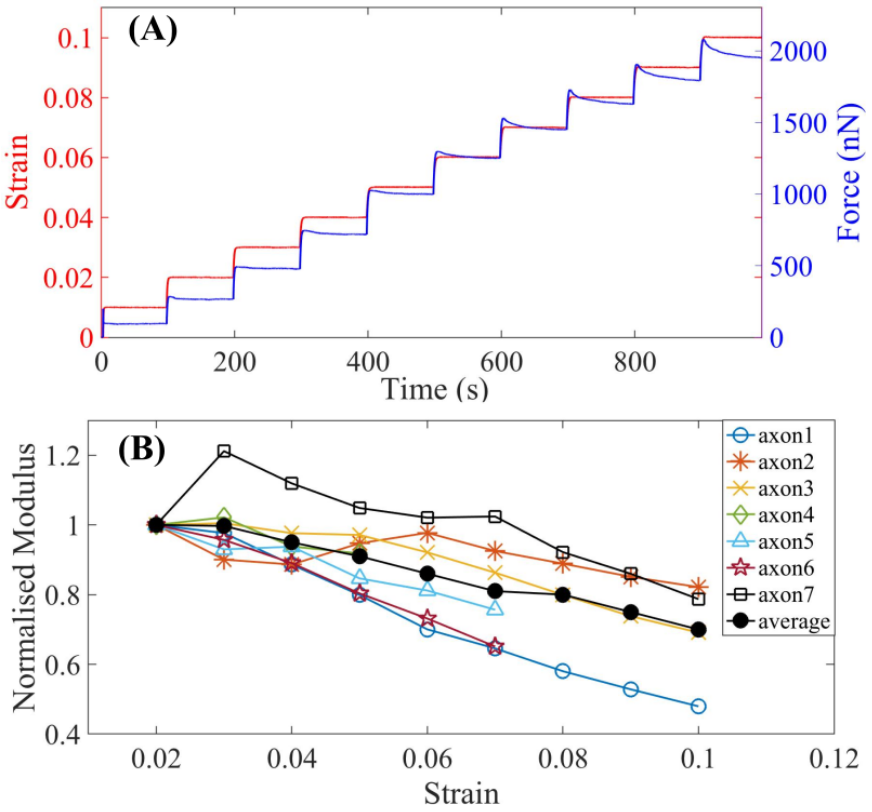


FIGURE 3.14: **Protein-protein fixation (A)** A typical force response of 2-DIV axon treated with fixative solution shows higher force values compared to control axons. **(B)** Normalized modulus for several axons shows strain-softening response.

Hence, the origin of strain-softening is not because of the filament turnover. Therefore, we probed the effect of destabilizing drugs in the next section.

### 3.6.2 Effect of filament destabilization on axonal response

To further investigate the possible role of the microtubule and F-actin cytoskeleton, we performed axon stretch experiments after specifically disrupting each of these elements. These treatments leave the axons very fragile, and they detach easily when pulled. Hence a cyclic step-strain protocol with $\gamma = 0.01$ was employed (Fig. 3.15). Moreover, to reduce scatter in data due to natural axon to axon variation, the same axon was probed before and after treatment. We first applied

cyclic strain on control axons for extended periods to ensure that axons are not damaged under such conditions (Fig. 3.15). As $\mathcal{T}_0$ cannot be determined from cyclic steps of single step size, we compared the net tension for the same axon before (Ctl) and after 5 min and 30 min of treatment.

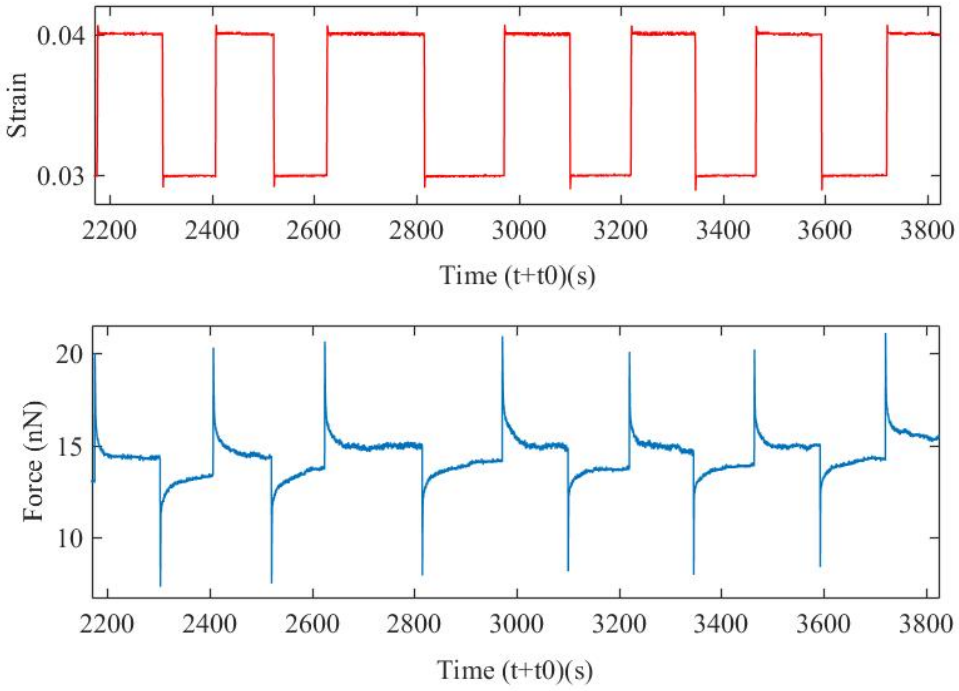


FIGURE 3.15: **Cyclic strain protocol** An example of an axon that was pulled to a strain of 3% and then cyclic strain has been applied over an extended period to show that there is no damage with the number of cycles. The data also show that the force evolution for up and down steps are similar except for the sign. This protocol is then used to study the effect of specific cytoskeleton disrupting agents–Latrunculin-A for F-actin, Nocodazole for microtubules.

We performed measurements after depolymerizing F-actin using Latranculin-A (Lat-A) at 1 μM for up to 30 min. After this treatment, we observe a huge reduction in the force response, as shown in Fig. 3.16. The figure shows a cyclic perturbation of axons before and after the treatment with Lat-A. We have measured the force for control cell, 5 min after treatment with Lat-A, and 30 min after treatment with Lat-A using cyclic strain protocol (Fig. 3.16). Treatment with 1 μM Latrunculin-A (Lat-A) for up to 30 min and observed that this treatment produced a dramatic reduction in the steady-state tension, as shown in Fig. 3.17A. In this case, we obtained $\mathcal{T}_{ss}(\gamma = 0.01) = 13.0$ nN±2.5(control), 3.5 nN±1.0(Lat-A: 5 min), 1.8 nN± 0.4(Lat-A: 30 min), where the values are mean ± SE (see Fig. 3.17A).

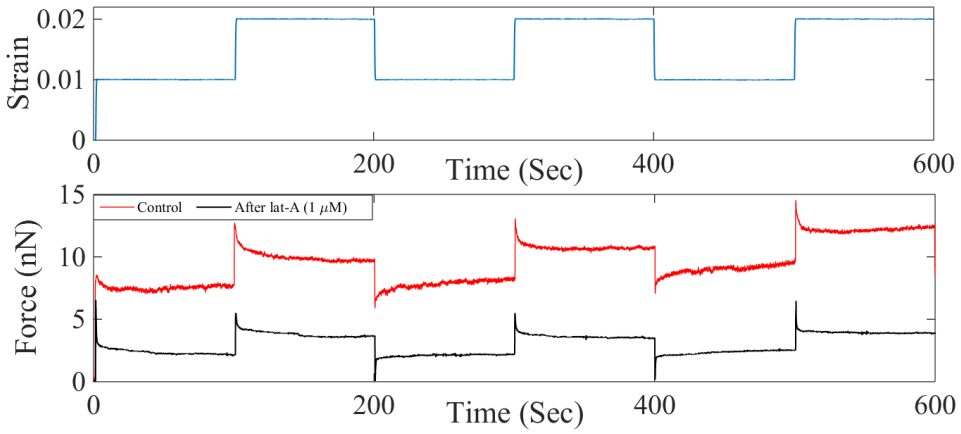


FIGURE 3.16: **Force measurement on Lat-A treated cells** A typical cyclic strain protocol to investigate the axonal response after treatment with Lat-A. The force response of the control axon (red) and the force response after treatment with Lat-A (black) show reduction after Lat-A treatment.

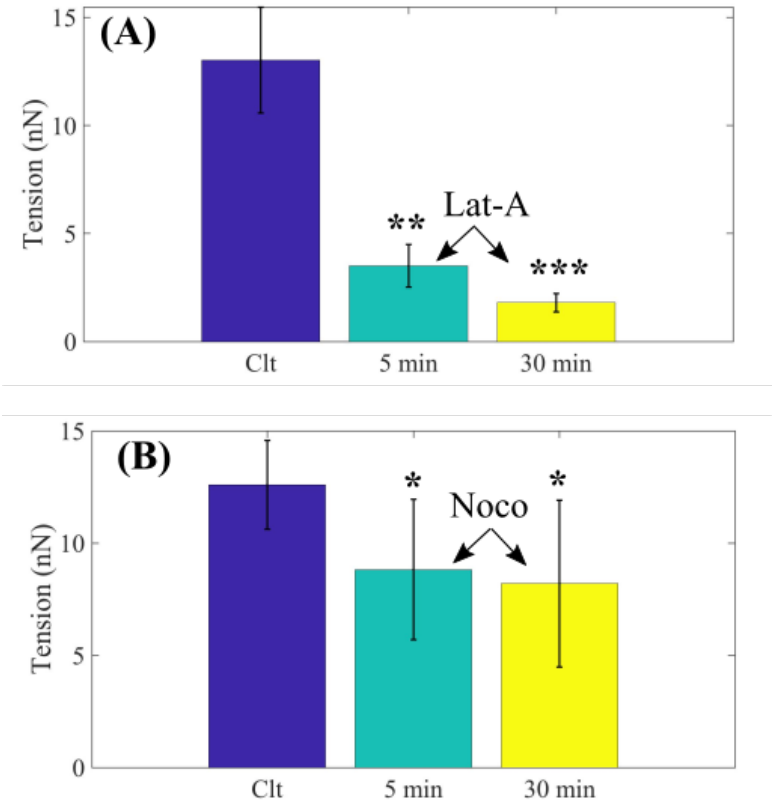


FIGURE 3.17: **Effect of destabilizing drugs:** Change in steady-state tension $\mathcal{T}_{ss}$ obtained after treating 2-DIV neurons with either the F-actin disrupting drug Latrunculin-A (1 μM) or the microtubule disrupting drug Nocodazole (10 μM) (n = 10 each). The data show a significant decrease in axonal tension after F-actin disruption and a relatively smaller decrease after disrupting microtubules. Bar plots of $\mathcal{T}_{ss}$ showing the significance of the two treatments. The tension was measured for the same axons 5 min and 30 min after exposure to the drug (error bars are SE).

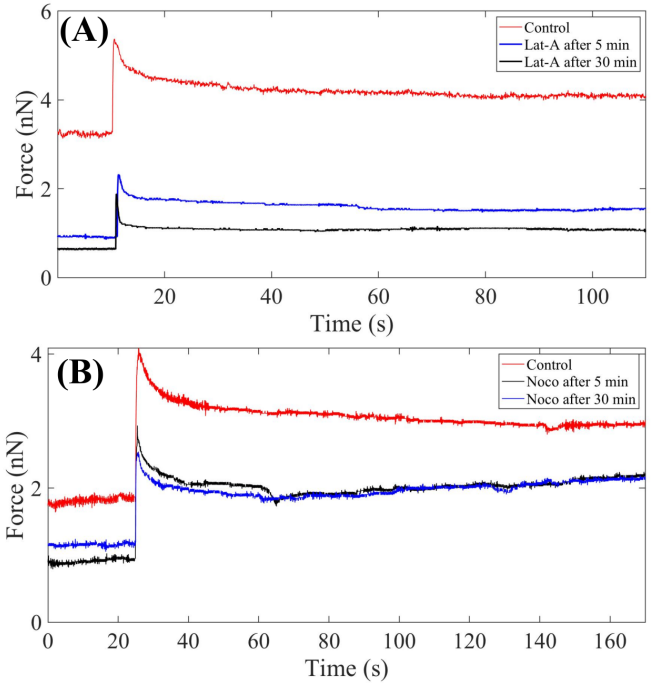


FIGURE 3.18: **Relaxation behavior after drug treatment** (A) Plot showing the force relaxation (at 2% strain) before and after application of Latrunculin-A (Lat-A) for 5 min and 30 min. (B) Plot showing the force relaxation (at 2% strain) before and after application of 10$\mu$M Nocodazole (noco) for 5 min and 30 min. Unlike in the case of microtubule disruption, F-actin depolymerization causes a significant reduction in the modulus (at 2% strain) and the relaxation time. There is no appreciable change in the relaxation time (at 2% strain) after microtubule disruption.

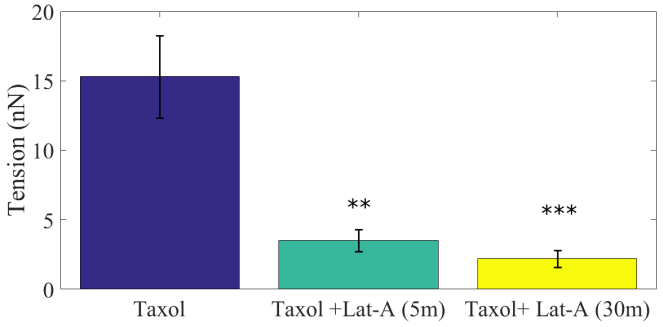


FIGURE 3.19: **Taxol and Lat-A treatment** Plots of $\mathcal{T}_{ss}$ for axons initially treated with Taxol for 30 min, and for the same axons subsequently treated with Lat-A for 5 min and 30 min (n = 7).

We then performed measurements after depolymerizing microtubules using Nocodazole (Noco) at 10 µM for up to 30 min. After this treatment, some axons exhibited pronounced beading, as is expected when microtubules are lost [67]. As can be seen from Fig. 3.17B, on the average, treated axons showed a reduction in steady state tension: $\mathcal{T}_{ss}(\gamma = 0.01) = 9.3$ nN $\pm$ 1.6(control), 6.4 nN $\pm$

2.1(Noco: 5 min), 5.8 nN ± 2.0(Noco: 30 min), where the values are mean ± SE (see Fig. 3.17B).

We found that F-actin has a larger effect on axonal mechanics due to stretch (Fig. 3.17). This also correlates well with the tendency of Jasplakinolide to cause a larger increase in axon elastic modulus as compared with Taxol (see Figs. 3.12, 3.11, 3.13). We also observe that the tension relaxation is much faster for Latrunculin-A treatment as compared with either Nocodazole-treated or control axons, suggesting that F-actin plays a leading role in strain-softening in axons (Fig. 3.18).

The larger effects seen after F-actin stabilization or disruption, when compared to microtubule perturbation, comes as a surprise as axonal mechanics is thought to be dominated by microtubules. Since there are interdependencies between the stability of these two components, we tested whether the sharp decrease in moduli after F-actin disruption could be due to microtubules too becoming destabilized subsequent to Lat-A treatment. For this, we first treated axons with Taxol to stabilize microtubules and then exposed these axons to Lat-A (all concentrations and time as above). We found that Lat-A treatment on microtubule stabilized axons, too, causes a huge reduction in the tension, as shown in Fig. 3.19. This unravels F-actin as a more relevant than microtubules in axonal mechanical response. This data, presented in Fig. 3.19, shows a drastic reduction in the steady-state tension after Lat-A treatment of microtubule stabilized axons. The values are $\mathcal{T}_{ss}(\gamma = 0.01) = 15.0$ nN ± 3.0(Taxol), 3.5 nN ± 0.8(Taxol+Lat-A: 5 min), 2.2 nN ± 0.6(Taxol+Lat-A: 30 min).

The emergence of F-actin as more relevant than microtubules to the axon mechanical response under stretching is surprising, given that microtubules usually form an aligned and tightly cross-linked bundle at the core of the axons. This finding prompted us to explore in more detail how F-actin regulates the axon stretch response, in particular via the periodic lattice of rings it forms together with $\alpha$ and $\beta$ spectrin tetramers [7, 41] (described in the next chapter).

### 3.6.3 Contribution from ATP driven processes

It has been shown that axons exhibit acto-myosin contractility [10, 55, 56]. In order to check the contribution from the ATP-driven processes in the experiments, we have performed experiments using Blebbistatin (myosin-II inhibitor) and the data show that the response of treated axons are similar to control cells (Figs. 3.20, 3.21)). There is no significant change in the axonal response either in force response or in elastic modulus when acto-myosin contractility is inhibited. This is because, in order to explore the passive mechanical response and to suppress active responses and to arrest growth-cone migration, we had chosen to do all measurements at room temperature (as active processes have an Arrhenius dependence on temperature a reduction by about 10 degrees reduces these contributions significantly) [87, 88]. The mechanical response of the active axons and extend the passive model to one that includes activity needs further investigation.

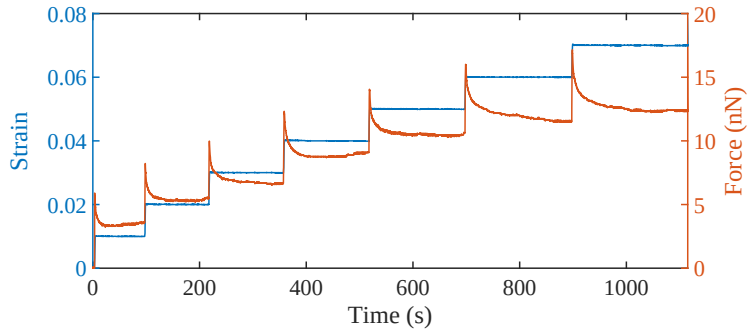


FIGURE 3.20: A typical force vs. strain plot for an axon treated with Blebbistatin (myosin-II inhibitor) (30 μM) for 30 mins at 37°C prior to force measurements. The force vs. strain plot shows qualitatively similar behaviour as control axons.

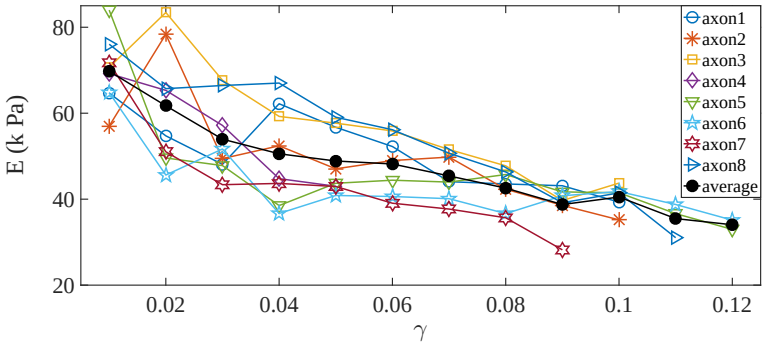


FIGURE 3.21: The elastic moduli for various axons treated with Blebbistatin which exhibit strain softening similar to control axons.

### 3.6.4 Contributions to axonal mechanics from other cytoskeletal components

As shown schematically in Fig. 1.2, the axonal cytoskeleton is a composite structure consisting of bundled microtubules, neurofilaments, and cortical F-actin structures other than that membrane periodic skeleton consisting of actin and spectrin skeleton. Our results show that F-actin is a major contributor to axonal mechanics due to mechanical stretch, whereas microtubule has a lesser effect. The dependence of stress relaxation on strain also has to be accounted for while considering which filament plays a major role. Dissecting this for a particular filament would be difficult. In fact, we show that the relaxation is really fast when F-actin is destabilized whereas microtubule destabilization leads to a similar relaxation time as control axons. This alone may suggest that microtubules probably have no role in observed non-monotonic relaxation behavior. But, it is also a possibility that F-actin disruption leads to breakage of actin-microtubules crosslinks.

Despite the variety of perturbation experiments, we report, delineating the individual contributions from these elements become challenging because of the mutual dependencies between them. Perturbing one cytoskeletal component could destabilize others as well. Hence, the effects of microtubule perturbation, for instance, maybe more complex than a simple change in their numbers. Microtubule bundles alone can account for softening if their cross-linkers (MAPs) exhibit binding-unbinding dynamics, but such models give a long time fluid-like response [79, 80] and also can not account for the peak in the relaxation time vs. strain plot. Thus, while microtubules may be making a direct contribution to the effective moduli we measure, microtubule elasticity alone can not account for the entire set of experimental observations we report. Another possibility is that microtubules become disrupted under dynamic loading. In fact, microtubules were shown to be weak under dynamic stretching of axons as they undergo depolymerization at high strain or strain rates [21]. Such catastrophic decay of microtubules under stretch, if it occurs, makes the mechanical support more critical in ensuring axonal integrity under fast stretch. However, we note that our experiments where we first stabilize microtubules with Taxol and then disrupt with Lat-A still causes a reduction in

stiffness comparable to that of Lat-A treatment alone. This suggests that the F-actin plays a major role, and spectrin skeleton associated with F-actin could possibly be a major contributor even in the presence of stabilized microtubules.

Neurofilaments, too, can play a role in axon mechanics as they form ionic crosslinks and connections to microtubules via motor proteins that transport them. It is also shown that neurofilaments can bear a stretch of up to about 400%, which can protect neurons while they are stretched under extreme strain conditions. Although, *in vitro* studies show that these networks stiffen considerably before any plasticity sets in, which is not in agreement with softening observed in axons at the very beginning at the smallest strain applied [73, 89].

## 3.7 Conclusion and Summary

Axon mechanics play an important role in normal neuron functioning and dictate how neurons respond to large stretch deformations. Although a number of studies have explored both active and passive axonal mechanics, the relation between the axonal cytoskeleton and its mechanical response remains poorly understood. In this chapter, we have quantified the role of their cytoskeletal elements to mechanical stretch. For this, we used an optical fiber based force apparatus, and with the help of various biochemical perturbing drugs, unravelled unique axonal mechanical behavior.

We have demonstrated that–
(i) axons passively (at 25°C, and timescales of minutes) behave as a viscoelastic solid-like material.
(ii) axons exhibit a strain-softening behavior due to their ability to buffer mechanical tension when stretched (tension homeostasis).
(iii) the relaxation times obtained from tension relaxation curves depend non-monotonically on the imposed strain.
(iv) F-actin emerges as a prominent contributor to the axonal mechanics.

The strain-softening response in sharp contrast to other cell types [74] reveals unique behavior in axons, which was not reported earlier. The relaxation times

reveal a unique feature of organization and dissipative processes happening inside axon due to stretch. We have also shown that axons are in pre-tension even before any applied stretch deformation.

We have explored the axon mechanical response in contrast to its cytoskeleton, by using experiments that either stabilize or destabilize specific filaments. Filament stabilization of microtubules using Taxol and F-actin using Jasplakinolide enhances the elastic moduli compared to control axons, but strain-softening is still prominent (Figs. 3.11, 3.12). This suggests that filament dynamics (polymerization or depolymerization) can not be accounted for observed strain-softening behavior. The increase in elastic moduli after Taxol can be accounted for by either increase in microtubule number or prevalence in ring structure due to crosstalk.

Filament destabilization of F-actin using Lat-A and of microtubules using Noco show that F-actin plays a major role in axonal behavior. After Lat-A treatment, the steady-state tension drops drastically, whereas Noco treatment has a lesser effect on steady-state tension (Fig. 3.17). To investigate the mechanical behavior in the presence of stabilized microtubules, we first stabilized the axons with Taxol for 30 mins and then treated with Lat-A. We found that the steady-state tension drops drastically after Lat-A treatment (Fig. 3.19). This suggests that F-actin contribute significantly than microtubules to the axonal mechanical response. In fact, our result of relaxation time behaviour also reveals that after F-actin disruption, the relaxation becomes faster, whereas microtubules disrupted axons show similar relaxation behavior as control axons (Fig. 3.18). Although, our experiments are performed at room temperature to suppress motor activity [87, 88], we checked whether the axonal response is influenced by acto-myosin contractility as reported in [55, 56]. Blebbistatin treated cells show similar response as control cells (Figs. 3.20, 3.21).

F-actin emerges as a major contributor than microtubules, Neurofilaments too can be excluded as they stiffen due to entropic elasticity, whereas our results show the softening at even smaller strains. Binding-unbinding process of microtubules sliding also can not be accounted for the observed viscoelastic solid-like response. Having these results and observations in mind, where axons exhibit

strain-softening and F-actin plays a major role in axonal mechanics, what possible mechanism could be responsible for the axonal behavior. The recent discovery of a periodic lattice of actin rings connected by longitudinally aligned spectrin tetramers [7, 41] is thought to protect axonal integrity. Along with these results, we explored in Chapter-4, the structure–function relationship of the axonal cytoskeleton in contrast to the actin-spectrin cytoskeleton.

# Chapter 4

# The role of spectrin in axonal mechanics

## 4.1 Introduction and Motivation

This chapter discusses the role of recently discovered periodic membrane skeleton (actin-spectrin skeleton) in axonal mechanics. Axonal cytoskeleton has three main types of filaments namely microtubules, actin, and neuro-filaments [3]. Microtubules are found in bundled form and thought to be main load bearer in axons [80]. It has been also shown that neurofilaments regulates the diameters of axons [40]. Apart from actin-spectrin skeleton, actin is also found in the form of waves, trails, etc. [44]. Recently, it has been discovered that actin and spectrin and other associated proteins are arranged in a periodic fashion inside the axons [7, 41]. The role of these periodic arrangement has not been fully understood and it has been hypothesised that these periodic structure can protect the mechanical integrity of axons [7, 14]. Apart from these filaments, axonal cytoskeleton has several proteins (for example, Tau) which can also contribute to mechanical response [79, 80]. Since, actin along with the crosslinking protein spectrin forms a ring like periodic skeleton, we investigated the role of spectrin in axonal mechanics. In this chapter, I will discuss the role of spectrin in axons in relation to actin-spectrin periodic skeleton.

Spectrin elasticity is known to maintain the mechanical integrity in Red Blood Cells (RBCs). Strain-softening response has been reported in the RBCs which is presumably known due to unfolding of spectrin repeat units [84]. In *C. elegans*, axons lacking spectrin break when stretched during normal body bends but axonal growth remains unaffected [13]. Together with these observations and our finding that F-actin as a major contributor which forms actin-spectrin membrane periodic skeleton motivated us to think about spectrin as contributor to axonal mechanics and developed a minimal model to account for all observed behaviours.

## 4.2 Structure of spectrin

The native spectrin molecule is a tetramer made up of two $\alpha$ and two $\beta$ subunits. The spectrin subunits $\alpha$ and $\beta$ bind side by side to form antiparallel $\alpha$-$\beta$ heterodimers. These dimers associate in a head to head arrangement to form $\alpha$-II–$\beta$-II tetramers [90, 91]. The contour length of the spectrin protein has been found to be $\sim$200 nm by electron microscopy [90].

The bulk of the spectrin polypeptide is made up of successive triple helical repeats of approximately 106 amino acids, known as spectrin repeats. $\beta$-spectrins contain 16 full repeats whereas $\alpha$-spectrins contain 20 full repeats (Fig. 4.1) [90, 91]. The partial repeats from N-terminus of $\alpha$ and C-terminus of $\beta$-spectrin leads to a formation of another repeat while forming the tetramer [90]. While the formation of a dimer, $\alpha$ and $\beta$ spectrin subunits interact via partial repeats of N-terminus of $\alpha$-spectrin and the C-terminus of $\beta$-spectrin subunits [91]. These partial repeats of $\alpha$ and $\beta$-spectrin can interact with the corresponding partial repeats of another dimer to form a tetramer [91]. Thus, the tetramer is formed by reconstituting a full triple helix from the pair of partial triple helices.

In RBCs, spectrin tetramers cross-linked to short actin filaments underneath the plasma membrane into a 2D polygonal network (mostly comprised of hexagons and pentagons)[92, 93]. Treating RBCs with Lat-A significantly reduces their stiffness [94].

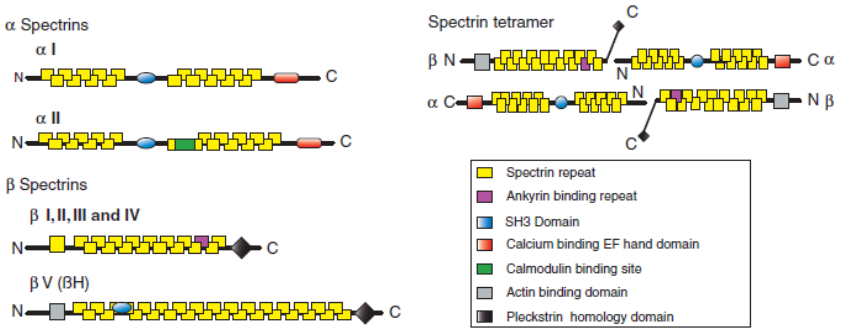


(a) (b)

FIGURE 4.1: **Structure and variants of spectrin proteins:** (a) Molecular domains of spectrins–two $\alpha$ and five $\beta$-spectrins are shown. Spectrins consist of modular units called spectrin repeats (yellow) and other domains such as the ankyrin binding domain promote interactions with binding targets important for spectrin function. (b) The spectrin tetramer is the fundamental unit of the spectrin-based membrane skeleton. The spectrin repeat domains of $\alpha$ and $\beta$ spectrin associate end-to-end to form heterodimers. Heterodimers associate laterally in an antiparallel fashion to form tetramers ( figure and caption adapted from Bennett *et al.* [95]).

Spectrin crosslinks directly or via adaptor proteins to trans-membrane proteins, membrane lipids and the actin cytoskeleton [91]. Moreover, the local concentration of spectrin is a key determinant for the preferential formation of sub-membrane periodic structure in axons [14, 96].

Spectrin may have isoform specific functions, since the isoforms are distributed differently in individual neurons. $\beta$-spectrin maintains a good deal of functionality even in absence of $\alpha$-spectrin [90]. $\beta$-spectrins contain the essential binding sites for actin and adducin and can form functional homo-oligomers at vertebrate synapses. Since the amino acid sequence of the actin binding domain (ABD) is highly conserved in spectrin proteins, it highlights the importance of actin binding activity of the protein [90, 92]. Spectrin is an actin-binding protein, important for development and stabilisation of axons and maintenance of neuronal polarisation [97].

## 4.3 Spectrin and its significance in various cell types

Spectrin is a large and abundant protein comprising 2.4% of total protein in mammalian brain [90]. It was first discovered in human erythrocytes and found to be

a component of the sub-membrane cytoskeletal scaffold wherein, it was either directly anchored to the plasma membrane or via anchoring protein ankyrin. Spectrin is found across many species and cell types such as *C. elegans*, RBCs, including neurons [90]. Members of the spectrin family are expressed in most animal cells (including neurons) but are not present in bacteria, plants or fungi [95]. Spectrin has been known to adopt a periodic organisation in neurons of a variety of animal species like *C. elegans*, fruit flies, chickens, mice and human brain slices [96]. In *C. elegans*, $\beta$-spectrin is encoded by a single gene, UNC-70 [13]. A polygonal lattice structure similar to one in RBCs membrane has been observed for spectrin in *Drosophila* neuromuscular junction [98]. $\beta$-spectrin abundant in the vertebrate brain, is expressed more strongly in neurons than other tissues. Fruit flies and nematodes have a single $\alpha$ subunit and two $\beta$ subunits. Vertebrates (mammals) have five conventional $\beta$ spectrins ($\beta$I to $\beta$V) and two $\alpha$-spectrins ($\alpha$-I and $\alpha$-II) . $\alpha$-I and $\beta$-I spectrin are expressed most abundantly in mammalian erythrocytes. $\beta$-II spectrin is abundantly expressed in both axons and dendrites [95].

Spectrin is found in synapses as well and plays major roles in synapse stabilization and dendritic spine morphogenesis. The membrane periodic skeleton (MPS) was disrupted at the pre-synaptic sites whereas a significant fraction of MPS was observed in the spine necks [96]. This disruption and irregularity in $\beta$-II spectrin periodicity and distribution respectively at the synaptic boutons suggests that the stable MPS structure might be inhibiting synapse formation and maturation [96].

## 4.4 Role of spectrin in mechanics

Spectrins are required for the organization of cells in tissues of multicellular animals [91]. Spectrin has a range of interactions that control membrane protein accumulation and activity [91]. The mechanical contribution to cells could arise from its intrinsic ability to reversibly unfold in response to mechanical stretch [13, 82, 84]. For example, RBCs must withstand deformation and shear as they pass through capillaries even smaller than their diameter. $\beta$-spectrin is essential for their membrane stability and elasticity [84]. This function depends on the

dynamic rearrangement of the spectrin dimers/tetramers under the mechanical shearing forces experienced in circulation [91].

In *C. elegans*, $\beta$-spectrin is not required for neuronal functions such as growth cone migration and axon elongation. But it plays a major role in maintaining physical integrity and stability of neuronal processes as strain resistance. Axons lacking $\beta$-spectrin break due to their inability to resist strain deformation while worm executes body bends [13]. Similarly in fruit flies, $\beta$-spectrin lacking axons grow normally but later show disorganized axon tracts and midline crossing defects [90, 99].

Neurons exhibit remarkable elastic properties as stretching up to 65% of their length without breaking [100]. This makes a role of spectrin in neuronal elasticity consistent with its known function of membrane elasticity in RBCs. $\beta$-spectrin is abundant in brain and is found in both the axonal and dendritic processes of all neurons. Thus, the elasticity of neurons may also be determined in large part by $\beta$-spectrin and the periodic membrane skeleton [13]. In neurons, spectrin is also responsible for roles ranging from stabilization of axons, formation of AIS (axon initial segment) and nodes of Ranvier and long term stabilization of synapses [41, 90, 96].

## 4.5 Physiological impact of spectrin loss and dysfunction

In RBCs, mutations in genes encoding $\alpha$ and $\beta$-spectrin leads to hereditary spherocytosis and hereditary elliptocytosis. These lead to abnormal shape and size of RBCs and causes anemia [90]. Neurons that lack $\beta$-spectrin have a specific defect in strain resistance. Some inherited neuronal diseases are direct result of mutations in $\beta$-spectrin [13]. Loss of $\beta$-spectrin in *C. elegans* (Unc -70 mutants) leads to spontaneous breaking of axons because they cannot withstand the movement but $\beta$-spectrin is not required for many neuronal functions such as axonal elongation and growth cone migration [13]. $\beta$-spectrin loss in fly neurons leads to disorganised axon tracts whereas loss in mice resulted in nervous system defects [90]. Spectrin

mutations are associated with neurological disorders like spinocerebellar ataxia [101] and early infantile epileptic encephalopathies [102].

Knocking down $\beta$-II spectrin using shRNA disrupted the MPS structure in axons. $\beta$-II spectrin knockdown also seem to have affected stability of $\beta$-III and adducin so subsequent reduced protein levels could have facilitated the MPS disruption. Moreover, this disruption was comparable to that caused by actin disrupting drug Latrunculin-A [14].

## 4.6 Actin-spectrin membrane periodic skeleton

Actin forms a ring like structure in axons with periodically spaced spectrin tetramers beneath the plasma membrane (Fig. 4.2). The actin ring is assumed to be formed by short capped actin filaments of about 35 nm [7]. However, recent study revealed that actin can be also found in long filamentous form and have a braid like structure. This braided structure is connected by spectrin mesh [103]. Spectrin tetramers isolated from the brain exhibit about 200 nm in length and are comparable to the spatial periodicity observed for actin rings [7, 14, 41].

During development, first actin and spectrin arrange themselves in periodic fashion and at later stages other proteins such as adducin, sodium channels forms a periodic arrangement [14, 41]. It is speculated that actin having capping protein adducin at its growing end and this protein adducin help in binding with spectrin. The role of adducin has been shown to regulate the axonal diameter. Adducin knockout experiment shows bulging of axonal diameter approximately 1.2 times the control which indicates the role of capping of actin filaments [104]. Whereas mechanical role of adducin in axonal integrity has not been shown. The removal of the adducin is predicted to dysregulate actin filament length, resulting in increased filament size and consequently in an increased diameter of actin rings. The other role of adducin is still unclear in axonal ring system. More studies with the help super-resolution imaging will need to shed light on this. Adducin is not essential for ring system although it plays a role in maintaining axonal diameter [104].

The data also suggest that the N-terminus of spectrin actin-binding domain is sufficient for actin ring binding to the spectrin lattice and adducin has probably transient role in forming the actin ring skeleton [14, 104]. Spectrin tetramers forms a longitudinal array to bind with actin filament. The free and resting length of spectrin tetramer is $\sim$ 55-65 nm [105]. In actin ring system it is found to be around 180-190 nm long which is the extended tetramer length. This 1-D periodic lattice arranged all over axons and also found in dendrites [41]. Spectrin is assumed to be under tension as it is found in an extended form in axons. This has been confirmed with FRET sensor and laser axotomy experiments that spectrin is already under tension in neurons [68]. Depletion of $\beta$-spectrin or disruption of F-actin leads to dis-assembly of MPS whereas knockout of $\beta$-spectrin leads to axonal breakage [13, 14]. Microtubule stabilization by Taxol enhances prevalence of MPS [14]. It is also shown that MPS plays a maintaining role for microtubules [97]. The last two results clearly indicate an interdependency between MPS and microtubules.

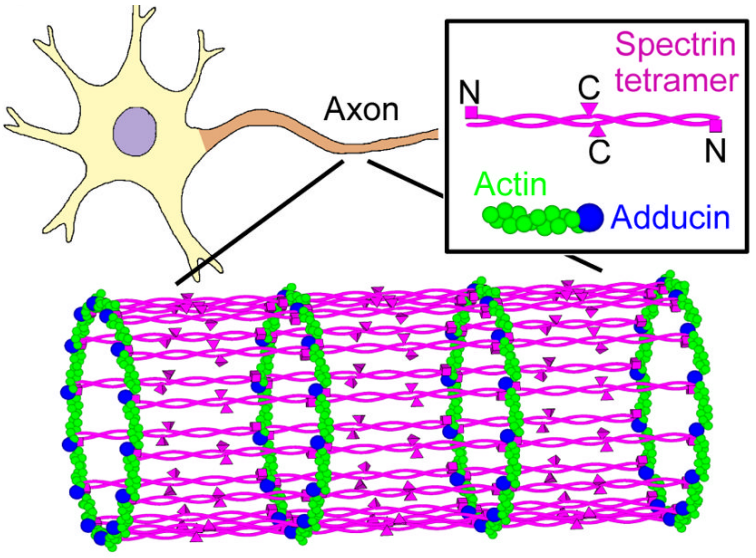


FIGURE 4.2: **Description of Actin-spectrin skeleton in axons** Spectrin tetramers are connected with short actin filaments and with capping proteins adducin. The N-terminus of spectrin tetramers are connected by capping proteins adducin (figure adapted from Xu *et al.* [7]).

The origin of the ring system and why it arranges itself in a periodic fashion is not fully understood. The role of these ring structures in axons in transport and mechanical integrity yet to be understood. With mechanical point of view, it maintains the integrity of axons but studies dedicated to show the role of ring

system in mechanics are very rare and there are no quantitative studies to show the same. It has been also shown that actin rings are present in variety of neuronal cells types and species [96].

In this thesis, we have shown the role of actin spectrin skeleton in axons under mechanical stretch.

## 4.7 Super-resolution Imaging

### 4.7.1 Super-resolution Imaging protocol

Neurons were fixed using 4% (w/v) paraformaldehyde (PFA) and 0.5% (v/v) glutaraldehyde in phosphate buffered saline (PBS: 5.33 mM $KCl$, 0.44 mM $KH_2PO_4$, 4.16 mM $NaHCO_3$, 137.93 mM $NaCl$, 0.33 mM $Na_2HPO_4$, 5.55 mM D-Glucose) for 10 min at room temperature (RT). Neurons were permeabilized with 0.2% (v/v) Triton X-100 in PBS for 5 min at RT and incubated in a blocking buffer of 3% (w/v) Bovine Serum Albumin in PBS at RT for 1 h. The fixed neurons were rinsed three times with PBS and incubated with anti-$\beta$-II spectrin antibody (BD Biosciences, 612563; 1:1500 dilution in blocking buffer) overnight at 4 °C. After rinsing again, the neurons were incubated with anti-mouse IgG conjugated to fluorescent Alexa Fluor 568 (A-11004, Thermo Fisher Scientific) or Alexa Fluor 488 (A-11001, Thermo Fisher Scientific ) used at 1:1000 dilution in the blocking buffer for 1 h at RT. Prior to mounting for microscopic examination, the cells were rinsed again and post-fixed with 4% PFA and 0.5% glutaraldehyde in PBS for 10 min at RT. For super-resolution microscopy, the neurons cultured for various days *in vitro* (DIV) were mounted in Mowiol (10% Mowiol 4-88 in poly(vinyl alcohol), 81381, Sigma-Aldrich) and DABCO (2.5% w/v, 1,4-diazobicyclo[2.2.2]octane, D27802, Sigma-Aldrich) and kept overnight in the dark at 4 °C prior to imaging.

Stimulated Emission Depletion (STED) nanoscopy was carried out using a Leica TCS SP8 STED system (Leica Microsystems). The fixed and mounted samples were imaged with the STED WHITE oil objective lens (HC PL APO 100×/1.40 OIL). CMLE JM deconvolution algorithm from Huygens Professional software (version 17.04) was used for deconvolution and processing of images.

### 4.7.2 Super-resolution imaging of axons

Before probing with super-resolution imaging, we imaged chick-neurons with spectrin labelling in confocal microscope. We found that spectrin is spread all overs axons which is shown in Fig. 4.3.

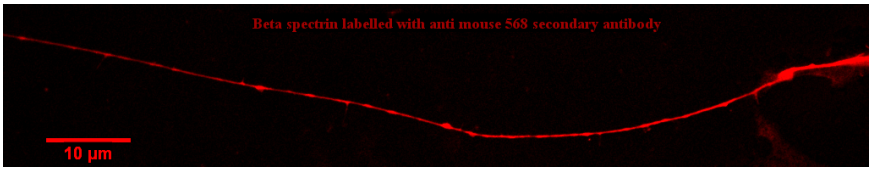


FIGURE 4.3: Confocal image showing spectrin distribution in an axon labelled using a primary antibody anti $\beta$-II spectrin and a secondary antibody anti-mouse IgG conjugated to Alexa Fluor-568. Spectrin is seen distributed all along all axons of all ages in confocal images.

Next, we imaged chick primary neurons with the help of STED nanoscopy $\beta$-II spectrin antibody staining. We imaged axons at various DIVs (Days in Vitro/ days in culture) and investigated the prevalence of actin-spectrin skeleton with age (Table. 4.2). At 1-DIV the rings are distributed in sporadically located patches showing periodic organisation along the axonal length but in older cultures (4-DIV) the periodic organisation is found throughout the axonal length. Going by our experiments with various drugs, we imaged axons after treatments of cytoskeletal perturbing drugs. We imaged and analysed the images after treatment with Taxol, Jasplakinolide, Latrunculin-A. The typical super-resolution images are shown in the figures below.

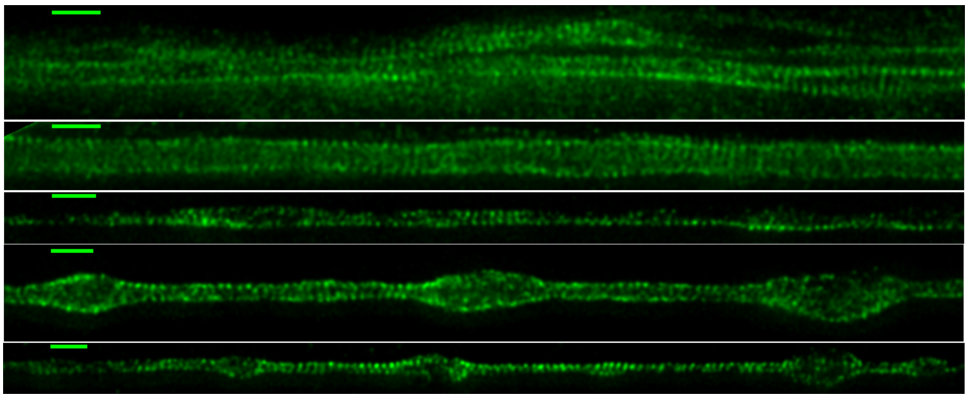

FIGURE 4.4: A typical Super resolution images of a DMSO vehicle control axon using STED nanoscopy labelled using a primary antibody anti $\beta$-II spectrin and a secondary antibody anti-mouse IgG conjugated to Alexa Fluor-488 (Scale bar = 1µm).

We performed super-resolution imaging on 2-DIV cells after treating them with the stabilizing drugs Taxol or Jasplakinolide that stabilizes microtubules or F-actin respectively for 30 min. The periodic skeleton is well preserved after treatment with either of these drugs (Figs. 4.5, 4.6). In vehicle control, 32 out of 36 showed rings; after treatment with Jasplakinolide, 28 out of 31 showed rings; and after exposure to Taxol, 31 out of 32 showed rings. We also did treatment with Latrunculin-A and no clear signature of periodic rings could be seen in 17 out of 19 axons.

Super-resolution imaging revealed that in Lat-A (induces F-actin depolymerization) treated cells rings are largely disrupted. We did autocorrelation analysis for control and Lat-A treated cells. A line of 1µm was drawn with a line width on the edge of the axon and the intensity profile is obtained using ImageJ. For these segments, 1-D autocorrelation was calculated using Matlab. Then an average of the autocorrelation was obtained for all axons. The amplitude of autocorrelation is defined as the difference between the maxima ($\sim$ 200 nm (first peak)) and minima ($\sim$ 100 nm) of the 1-D autocorrelation. The average amplitude is obtained by averaging over all the axons. 1-D autocorrelation amplitude for several axon segments of 1µm averaged over many axons (n=10). Vehicle control axons show a clear periodicity of $\sim$200 nm and strong correlation where as Lat-A treated axons show very weak correlation which suggests that the spectrin periodicity is largely disrupted in Lat-A treated axons (Fig. 4.7B). Effect of various drugs on actin-spectrin cytoskeleton is presented in Table. 4.1.

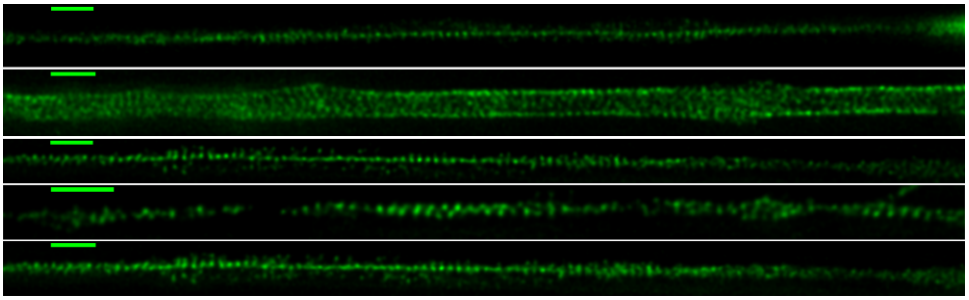

FIGURE 4.5: Super resolution image of an axon after treatment with Taxol for half an hour using STED nanoscopy labelled using a primary antibody anti $\beta$-II spectrin and a secondary antibody anti-mouse IgG conjugated to Alexa Fluor-488 (Scale bar= 1µm).

| **Drugs** | **Effect on rings** | **References** |
|---|---|---|
| Lat-A (20 µM) & Lat-A (200 nM) | Disrupt rings, prone to younger culture | Zhong *et al.* 2014 & Qu *et al.* 2016 [14, 106] |
| Nocodazole (50 µM for 1h) | Disrupts rings | Zhong *et al.* 2014 [14] |
| Taxol (5 nM for 3 days ) | Rings seen in all axons like processes | Zhong *et al.* 2014 [14] |
| Jasplakinolide | Rings present | Wang *et al.* 2019 [107] |
| Cyto-D (50 µM) & Cyto-D (800 nM) | Disrupts rings | Zhong *et al.* 2014, Qu *et al.* 2016 [14, 106] |

TABLE 4.1: Drug treatment and their effect on periodic membrane skeleton.

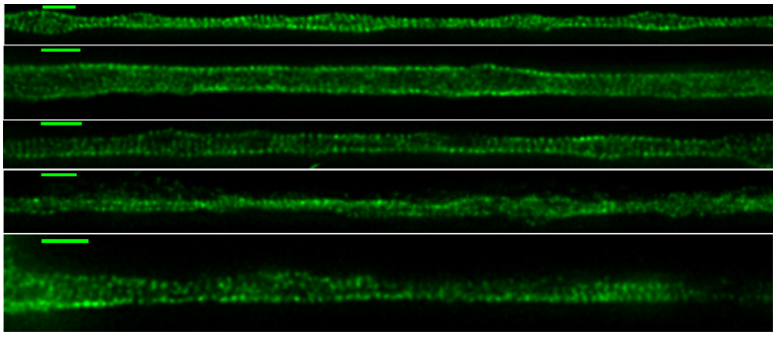

FIGURE 4.6: Super resolution image of an axon after treatment with Jasplakinolide for half an hour using STED nanoscopy labelled using a primary antibody anti $\beta$-II spectrin and a secondary antibody anti-mouse IgG conjugated to Alexa Fluor-488 (Scale bar= 1µm).

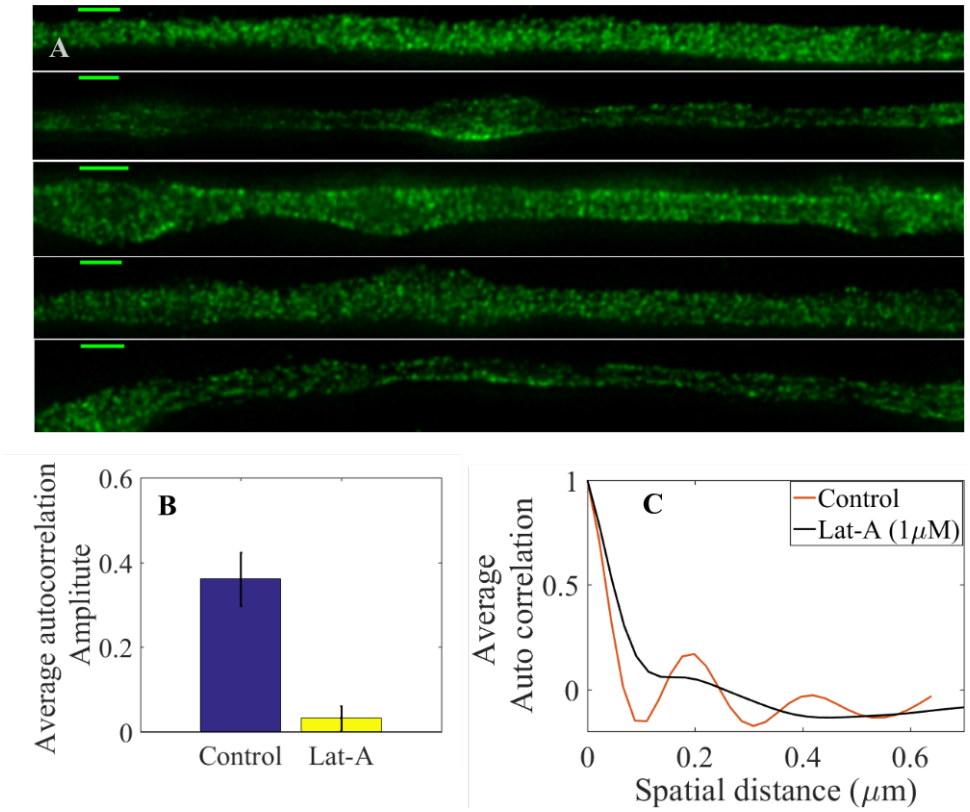


FIGURE 4.7: (A) Super-resolution images of 2-DIV axons treated for 30 min with 1 $\mu$M Lat-A labelled using primary antibody anti$\beta$-II spectrin and secondary antibody anti-mouse IgG conjugated to Alexa Fluor 488 (Scale bar = 1 $\mu$m). It is clearly seen that the periodicity seen in control axons (Fig. S11) is absent in these images. (B) 1-D autocorrelation amplitude for several axon segments of 1µm averaged over many axons (n=10) which suggests that the spectrin periodicity is disrupted in Lat-A treated axons. (C) Intensity-intensity autocorrelation of DMSO vehicle control axons and those treated with Lat-A (1µM) for 30 min, averaged over many axons (n=10). Vehicle control axons show a clear periodicity of ∼200 nm and strong correlation where as Lat-A treated axons show very weak correlation.

### 4.7.3 STED Super Resolution Microscopy analysis of different DIV axons

We did a quantification of actin rings observed in super-resolution imaging. At early stages rings are seen as patches, as the age of culture increases the rings are seen in clearly visible ladder-like distribution. The table summarizes the quantification of development of rings (Table. 4.2).

The periodicity in actin-spectrin lattice is reported to be ∼200 nm which is the tetramer length [7, 14]. Here we have quantified the periodicity in many axons

| DIV | No. of axons | regular ladder | | ladder in patches | | no visible ladder | |
|---|---|---|---|---|---|---|---|
| | | Number | % | Number | % | Number | % |
| 1 | 14 | 3 | 21.4 | 3 | 21.4 | 8 | 57.1 |
| 2 | 13 | 4 | 30.8 | 6 | 46.2 | 3 | 23.1 |
| 3 | 13 | 8 | 61.5 | 5 | 38.5 | 0 | 0 |
| 4 | 10 | 7 | 70.0 | 3 | 30.0 | 0 | 0 |
| 5 | 13 | 10 | 76.9 | 3 | 23.1 | 0 | 0 |

TABLE 4.2: STED image analysis for quantification of rings: Here we quantify the occurrence of periodic rings (ladders) seen at various DIVs within an imaging field of view. It is evident from the table that as axon mature the rings develop all over the axons.

for various DIVs (Fig. 4.8). A table summarises representing an early detection of ring system in various cells is represented in (Table 4.3).

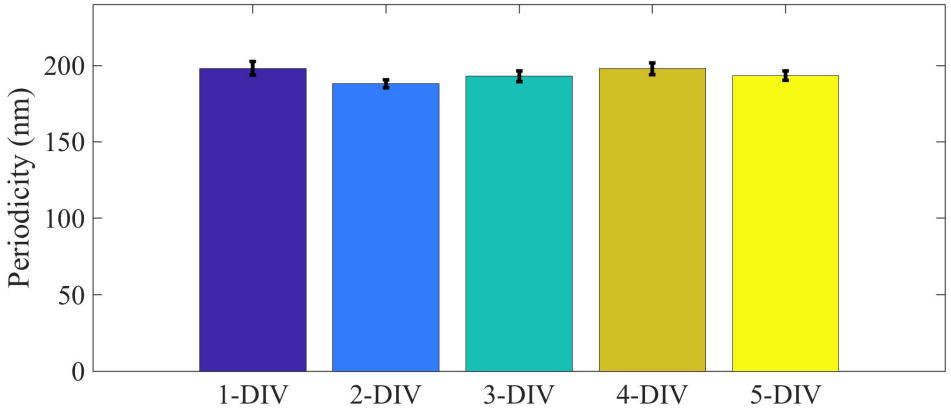


FIGURE 4.8: Periodicity of spectrin lattice in axons of different age measured using STED microscopy. Number of axons used in each case was n(1-DIV) = 23, n(2-DIV) = 23, n(3-DIV) = 24, n(4-DIV) = 20, n(5-DIV) = 24 This analysis was done using LAS AF version 3.3.0.10134 from Lieca Micro-systems by drawing a line along the axon and the average distance between adjacent peaks were measured for each axon.

### 4.7.4 Super-resolution imaging using Structured Illumination Microscopy (SIM)

We also did super-resolution imaging with SIM microscopy on our neuronal culture at IISER, Pune, imaging facility. A similar fixation and immunostaining protocol as STED nanoscopy was used for SIM imaging. SIM imaging was performed using a DeltaVision OMX SR (GE Healthcare) with a 60×, numerical aperture (NA) 1.42 oil immersion PSF lens and FITC/AF488 or Texas Red/AF568 filters. The OMX Master Control software, AcquireSR and softWoRx reconstruction and

analysis software were used to project images. Typical SIM images of 3-DIV axons are shown in Fig. 4.9 which are labelled using a primary antibody anti $\beta$-II spectrin and a secondary antibody anti-mouse IgG conjugated to Alexa Fluor-568. The images show periodic structure along the axon similar to those of STED nanoscopy images (Fig. 4.9).

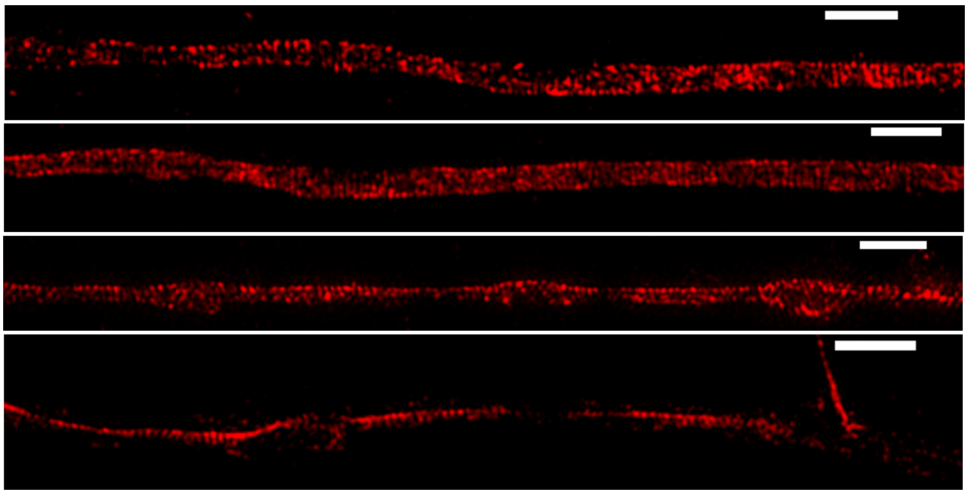

FIGURE 4.9: **SIM images** Typical images of control axons using Structured Illumination Microscopy (SIM) labelled with a primary antibody anti $\beta$-II spectrin and a secondary antibody anti-mouse IgG conjugated to Alexa Fluor-568 (Scale bar= 2µm).

| **Rings present at** | **Cell culture type** | **Rings abundance** | **References** |
|---|---|---|---|
| 2-DIV | Hippocampal neurons | Rings in form of strips and bundles | D'stle et al. 2015 [41] |
| 2-DIV | Hippocampal Neurons | Rings present at proximal regions | Zhong et al. 2014 [14] |
| 6 HIV (hours in vitro) onwards | fly neurons | 20% abundance at 6 HIV | Qu et al. 2016 [106] |
| 1-DIV | DRG explants from mice | no quantification | Unsain et al. 2018 [108] |

TABLE 4.3: Presence of rings in various cell types and their abundance .

### 4.7.5 Force measurement on 4-DIV axons

Developmental studies on actin-spectrin skeleton reveal that actin rings become more prevalent with age in culture [14, 41]. Our own experiments with super-resolution imaging show that rings become more prevalent with age. This result

prompted us to do mechanical measurements on 4-DIV axons. The force measurements on 4-DIV axons unravel interesting phenomenon. We found that the rest tension of 4-DIV cells axon are higher than that of 2-DIV axons which supports the fact that with age actin-spectrin skeleton gets prevalent (Fig. 4.10) (2-DIV: n= 10, mean = 3.7, SE = 1.2; 4-DIV: n = 7, mean = 5.3, SE = 2.2).

The steady state tension of 4-DIV axons shows tension saturation which indicates tension-homeostasis (Fig. 4.11). Remarkably, average elastic moduli for 4-DIV axons shows higher value than that of 2-DIV axons which is well correlated with prevalence in actin-spectrin skeleton (Fig. 4.12).

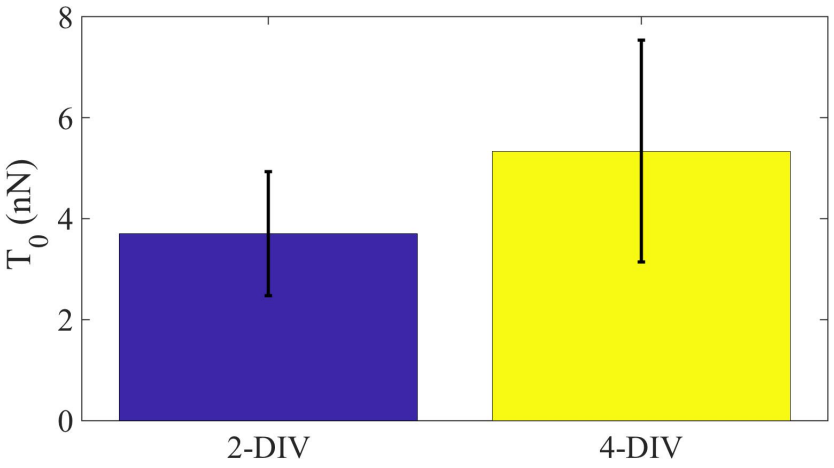


FIGURE 4.10: Plot showing the difference in rest tension $T_0$ with age for 2-DIV and 4-DIV axons. 2-DIV: n = 10, mean = 3.7, SE = 1.2; 4-DIV: n = 7, mean = 5.3, SE = 2.2. Note that the actin-spectrin lattice becomes more prominent and extensive with DIV.

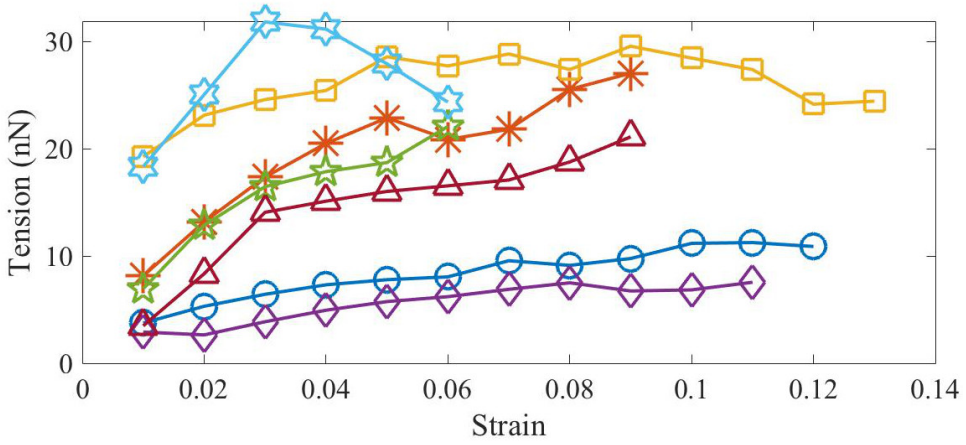


FIGURE 4.11: Evolution of the steady state tension as a function of strain for axons grown for four days in culture (4-DIV). Tension tends to saturates towards higher strain indicates tension homeostasis.

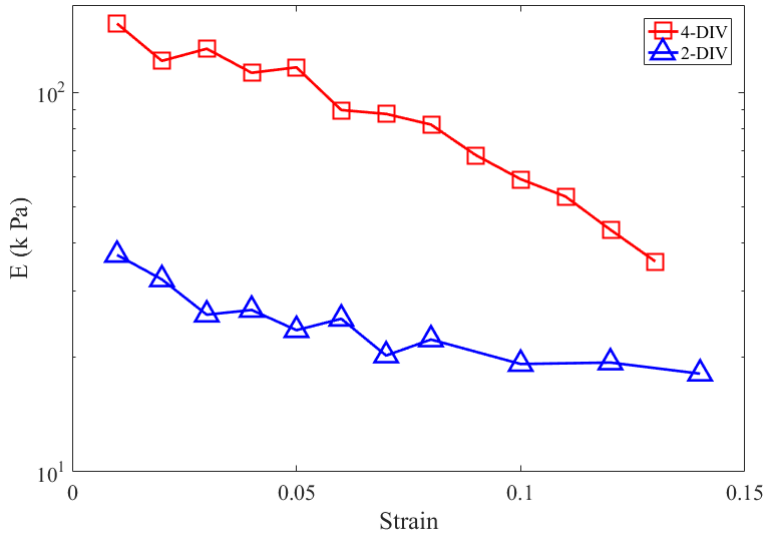


FIGURE 4.12: Log-linear plots of averaged Young's modulus vs strain for axons at 2-DIV (n = 5) and 4-DIV (n = 7) show a marked increase in moduli with age, and correlated with the prevalence in the actin-spectrin lattice.

## 4.8 Spectrin Knock-down

The results from different cytoskeleton perturbing drugs, we have shown in previous chapter that treatment with Lat-A, an actin monomer sequester, shows significant reduction in force response. Whereas, Nocodazole, a microtubule destabilizing agent, shows mild effect on force response. The stabilizing reagents of

microtubules and f-actin, Taxol and Jasplakinolide, respectively show similar response as control cells but higher in modulus. Earlier report shows that axon breaks in spectrin knockout cells in *C. elegans* [13]. We speculated that spectrin might be the protein which could contribute to force response significantly, keeping in mind that the actin-spectrin ring system in axons. It has been shown that rings are interdependent on actin and spectrin [14] where they show that depolymerising actin or knocking down spectrin leads to disruption of actin-spectrin rings. Having this motivation in mind, we have quantified the spectrin levels in axons using confocal microscopy. To do this we have first stained cells with spectrin anti-body and checked levels of spectrin in control and knock-down cells. We have used Morpholino oligo (MO) which is used to modify gene expression using Endo-Porter as a drug delivery tool.

### 4.8.1 Endo-Porter as a delivery tool

Endo-Porter is a reagent to delivering Morpholino oligos or proteins into the cytosol of cultured cells. Morpholino oligos are used for knocking down gene functions. Endo-Porter is a peptide-based reagent which retains the mechanism that relies on endocytosis, works in the presence of serum, and allows delivery of multiple oligos at a range of oligo concentrations. Delivery is least toxic when the process does not disrupt the plasma membrane. The mechanism of Endo-Porter delivery (see figure) relies on Morpholinos and Endo-Porter being taken up from the media into the same endosome. Endo-Porter is an amphiphilic peptide with a sharp transition pH, with a hydrophobic face which associates with cell membranes once added to culture medium. Natural acidification of the endosome protonates Endo-Porter that, in its ionic form, permeabilizes the endosome and releases the endosome contents into the cytosol (Ref: Genetools Inc.).

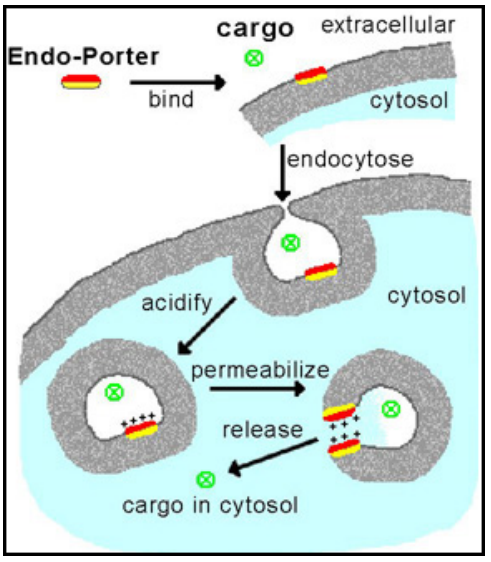


FIGURE 4.13: **Endo-Porter delivering Morpholino Oligos and the process** Endo-Porter binds to plasma membrane and taken inside of cytosol along with cargo through endocytosis. After being taken inside the cytosol the it permeabilizes and cargo is released inside the cytosol (adapted figure from Genetools Inc.).

## Methods

### 4.8.2 Endo-Porter protocol

Cells were grown on Poly-l-lysine coated coverslips so that axons remains adhere to the surface which will be beneficial in imaging. Cells were allowed to adhere to the glass surface for 3-4 hours after culturing and observed for slight neurite outgrowth in the microscope. Then, Morpholino was added (either untagged control or $\beta$-spectrin specific Morpholino) 20 µM directly over the plated cells and swirled gently. The tagged standard Morpholino was used at 10 µM while standardising protocol which will be described in later. 100 µl of the medium was taken gently from the sides of the coverslip area and was collected in a eppendorf tube. To this, Endo-Porter (2 µM) (in PEG solution) was added and mixed well while avoiding bubble formation. Then, the medium containing Endo-Porter was added directly back to the coverslip area and swirled gently. Cells were incubated at 37°C, for 48 hr.

(**Note**: Since Endo-Porter enters aqueous medium and forms aggregates, swirling

is advised so as to disperse these aggregates and limit their size. Ideally, Endo-Porter particles settle slowly to the bottom of plate and come in contact with the adherent cells.)

After 48 hr, plates with grown cells were rinsed twice with pre-warmed HBSS(+/+). Then fresh prewarmed L-15 (without methocel) medium with supplements were added. Cells were incubated for 30 mins at 37°C for stabilizing prior imaging.

For force measurements on Morpholino oligo transfected cells, the culture medium was replaced by supplemented L-15 lacking methyl cellulose 30 min prior to the experiments. Also, the coverslip was not coated with Poly-l-lysine in this case.

### 4.8.3 Fixation and Immunostaining

Cells were fixed using 4% paraformaldehyde (PFA) and 0.5% glutaraldehyde solution in PBS (ideal fixative) for 10 minutes at Room temperature. Cells were washed thrice using $1X$ PBS for 10 minutes per wash. Then, cells were permeabilised using 0.2% Triton X(100) in PBS for 5 minutes at Room temp. Again, Cells were washed thrice using 1X PBS for 10 minutes per wash. fixed cells were incubated and permeabilised in blocking buffer i.e. 3% bovine serum albumin (BSA) for 1 hour at Room temp. Then, Cells were incubated with 1:1500 dilution (in 3% BSA) of anti-$\beta$-II spectrin mouse antibody (BD Biosciences, Catalogue No.–612563) for overnight (approx. 16–18 hour) at $4°C$. Cells were washed thrice using 1X PBS for 10 minutes per wash after removing primary antibody ( primary antibody can be reused). Next, proceed with a 1:1000 dilution (in 3% BSA) of anti-mouse secondary (568) antibody for 1 hour at Room temp. Again, cells were washed thrice using 1X PBS for 10 minutes per wash and post fixed using 4% paraformaldehyde (PFA) and 0.5% glutaraldehyde solution in PBS (ideal fixative) for 10 minutes at Room temp. After washing the plates with PBS imaging were done.

### 4.8.4 Experimental conditions

Experiments were optimized for better cell growth, health and any morphological changes compared to control cells. Endo-Porter is toxic in nature which harms the cells in culture. To minimize this, we have done toxicity test and compared the cells with normal cells (control cells without Endo-Porter). We tested with different concentrations of Endo-Porter in culture and found out that final concentration of 2µM works better. This optimized concentration of Endo-Porter was used for all spectrin knockdown experiments including force measurements.

### 4.8.5 Image Analysis

The images were acquired using confocal microscope under green and red channel as well as in bright field (using trans PMT). Using ImageJ software, these images are then analysed for intensity of $\beta$-II spectrin immunolabel. Using the segmented line tool in ImageJ, a line is manually drawn along the length of positively transfected (as determined by GFP signal) as well as untransfected axons. The width of the line is then adjusted to the diameter of the axon (as per the image). Then mean, minimum, maximum of intensity values, and area under segmented line were measured using Measure tool of ImageJ. To get background, the same line is just shifted outside the axon (i.e. aligned next to it). Mean, minimum, and maximum of intensity values were measured.

Then background mean intensity values were subtracted from the mean intensity of the axon to get final mean intensity values for each axon. The final mean intensity values for all axons in both control and specific Morpholino treated conditions were plotted and analysed. Using Origin V9 and MATLAB perform descriptive statistics to calculate average, standard deviation, standard error mean, variance, etc. Non parametric column comparison tests (e.g. Mann Whitney) has been carried out to determine significance of co-relation between the two.

### 4.8.6 Intensity analysis on spectrin knockdown cells

We did an intensity analysis on spectrin distribution in spectrin specific MO knock-down and control MO cells using confocal microscopy and image analysis describe in earlier section. We found that there is significant reduction in spectrin intensity in Morpholino knock-down cells which is shown in Fig. 4.14 (Control Morpholino n = 90, Specific morpholino n = 91, p-value = $3.4437 * e^{-08}$) (SE is standard deviation from mean).

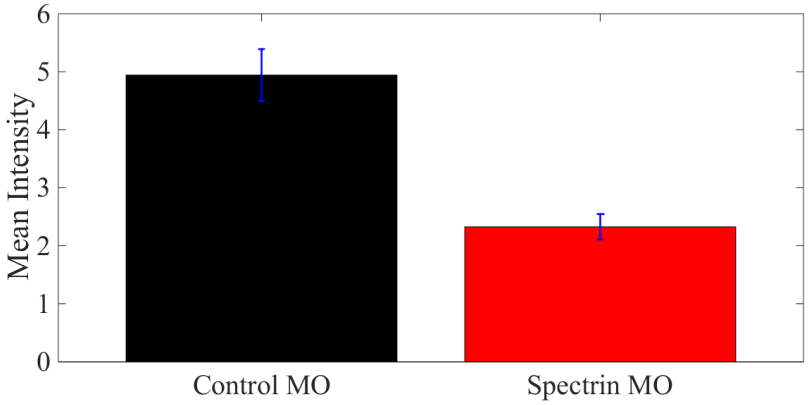


FIGURE 4.14: Intensity analysis for spectrin distribution in axons labelled using a primary antibody anti $\beta$-II spectrin and a secondary antibody anti-mouse IgG conjugated to Alexa Fluor-568. The plot shows reduction in spectrin intensity distribution after spectrin knockdown.

## 4.9 Force measurements on spectrin knock down cells

Motivated by our results and observation—F-actin as a major contributor to axonal mechanics and fascinated by our super-resolution imaging, we investigated the role of spectrin in axons by doing force measurements on spectrin knock down cells. Depletion of $\beta$-II spectrin has been reported to abolish the periodic organization of the actin-spectrin membrane-associated skeleton [14]. In *C. elegans*, the axons of spectrin knock-out animals are known to snap during normal wiggling of the worm, although the exact nature of axonal deformation (buckling vs stretch) that causes damage is unclear. In *C. elegans* experiments axons grow normally but snap while wiggle. In our experiments, we do not observe any physiological change compared to normal axons. Spectrin knock down axons do not breaks even after

application of stretch deformation. The reason could be in *C. elegans* they did a drastic knockout experiment whereas we did spectrin knock-down where some amount of spectrin available to prevent them from breakage.

By Intensity analysis on spectrin knocking down axons, we found that there is significant reduction in spectrin intensity distribution. Super-resolution images show spectrin rings all along axons and become more prevalent with days in culture. We grown axons similar methods described in methods section for 2 days in culture. We found that MO treated cells are healthy for 2 days in culture. But become unhealthy after 3 days in culture. Due to this reason we are only able to make force measurements on 2-DIV axons. We did force measurements on 2-DIV axons for both specific MO and control MO transfected cells. We found that spectrin knock down cells have much lower average steady state tension than to control MO cells as shown in Fig. 4.15. The extrapolation of tension vs strain data and fitting becomes poor in knockdown cells, hence rest tension could not be obtained. Due to this reason, we could not calculate the elastic modulus in spectrin knock down cells.

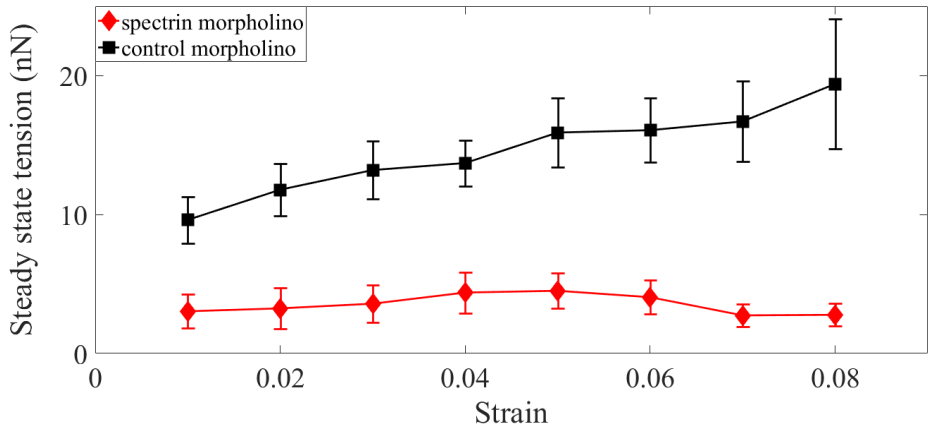


FIGURE 4.15: Plots of the averaged steady state tension Tss as a function of strain for 2-DIV neurons treated with a non-specific, control Morpholino (n = 10) and for those treated with an anti-$\beta$-II spectrin Morpholino (n = 10).

We could not observe any difference in growth characteristics or caliber between knock-down and control cells. Thus, these results clearly demonstrate the significance of the actin-spectrin skeleton in axonal response to stretch deformations.

The surprising result of spectrin knock down cells reveals another major cytoskeleton component to axonal mechanics. Having known that spectrin can unfold via its repeated units and the prevalence with age of actin-spectrin skeleton, we then turned to theoretical modelling to gain further insight into how this skeleton may contribute to the observed axonal response.

## 4.10 Folding-unfolding of spectrin buffers axonal tension

Motivated by our observations and key results–strain softening, F-actin is major contributor to axonal mechanical behaviour and significant reduction in steady state tension in knock down axons compared to control axons. We have developed a minimal model to account for our observations. The model is developed by Andrew Callan-Jones from Paris Dedirot University, Paris (updated model is presented in Appendix-B and can be found in [109]. F-actin disruption and spectrin knock down both have been shown to abolish actin-spectrin periodic skeleton [14]. Our force measurement on either F-actin disrupted cells or spectrin knock down cells shows significant reduction in the steady state force. These results shows that actin-spectrin play a major role in protecting from damage.

In RBCs, it is shown that strain softening arises due to spectrin unfolding [84]. Spectrin as described earlier has its folded domains and under applied force these domains reversely unfold.

Spectrin repeats having 106 amino acid residues folded in to triple helical coiled-coiled structure. Under force these repeats unfold and refold when force is removed. Single molecule force measurements on spectrin molecule with Atomic Force Microscopy (AFM) reveals that spectrin has several folded domains and force required to mechanically unfold these repeats to be 25 to 35 pN [82]. Typical example of this observation has been given in Figs. 4.16, 4.17. When a stretch using an AFM has been applied force reaches to a maxima which is the threshold force needed to unfold single domains. There are several domain unfolding events

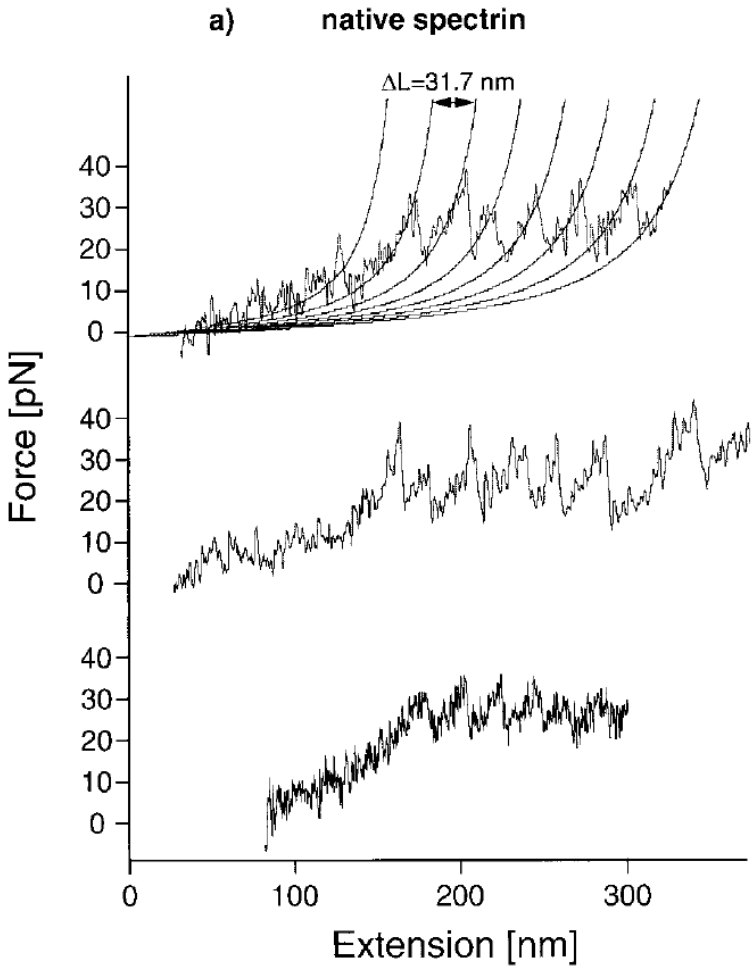


FIGURE 4.16: (a) Three unfolding traces of native spectrin. The continuous lines superimposed to the first curve are WLC fits ($p = 0.8A^0$ ). The gain in length upon each unfolding event is 31.7 nm, which corresponds to the 106 amino acid residues folded in each spectrin repeat (figure and caption adapted from Rief *et al.* [82]).

in native spectrin which are shown in Fig. 4.16. The increase in length $\triangle L$ after every unfolded domain is the length corresponding to 106 amino acid residues folded in each spectrin repeat [82].

Keeping these observations in mind, we then developed a minimal model of the axon mechanical response. Acknowledging that the axon cytoskeleton is complex [110] which has various filaments and organelle. We focused only on the actin-spectrin membrane skeleton for simplicity. This is partly justified by the predominant role played by the actin-spectrin skeleton in our experiments where actin and spectrin played a major role..

When an axon is suddenly stretched at constant strain, the tension is not constant,

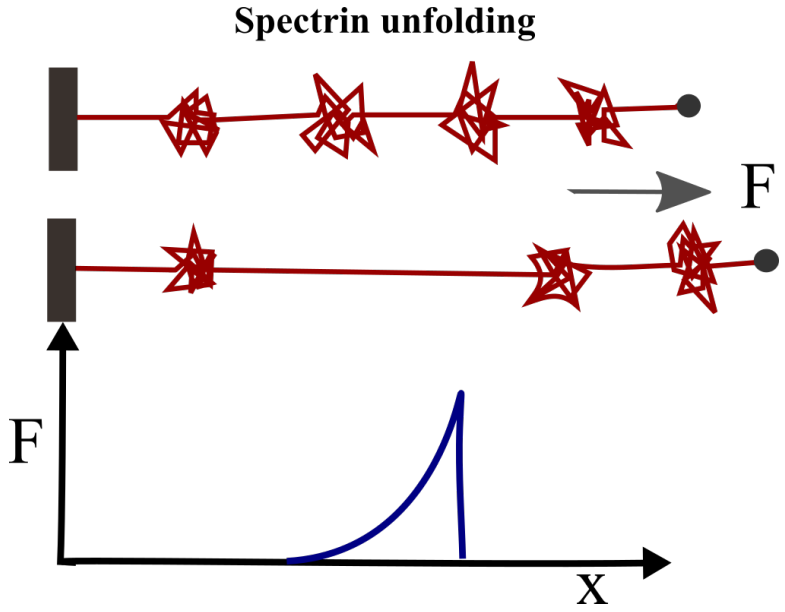


FIGURE 4.17: **Unfolding of spectrin repeat units:** Spectrin repeat units unfold while application of force. The force initially rises and when it crosses the threshold force which is to unfold a domain, suddenly falls when the domain is unfolded. Corresponding to each unfolded unit there is an increase in total length of the tetramer. This increase in the length corresponds to residues folded in each spectrin repeat.

but instead relaxes over time, indicating that dissipative processes are occurring at the microscopic scale. Noting that axon viscoelastic solid-like behaviour precludes unbinding processes, such as between spectrin tetramers and actin rings, we model tension relaxation as arising from unfolding/re-folding of repeats along a spectrin tetramer, which is known to yield softening at the single tetramer level [111, 112]. These unfolding events lead to dissipation of stored elastic energy.

With these assumptions in mind, our model consists of $M$ spectrin tetramers per axon cross-section (Fig. 4.19), such that each tetramer is attached at its two ends to an actin ring, as shown in Fig. 4.18. A spectrin tetramer is modelled as a polymer chain with $N = 76$ repeats [112], and each repeat can be in an unfolded ($u$) or a folded ($f$) configuration. Then, we let $N_{\mathrm{u}}(t)$ be the number of unfolded repeats on a tetramer at time $t$; therefore $N_{\mathrm{f}}(t) = N - N_{\mathrm{u}}(t)$ is the number of folded ones. Transitions from $u \leftrightarrow f$ depend on the typical tension per spectrin tetramer $\mathcal{T}_{\mathrm{s}}$. Since, there are $M$ spectrin tetramers per cross-section and tension is shared by $M$ tetramers. Then in an axonal cross-section, tension per spectrin tetramer is given by, $\mathcal{T}_{\mathrm{s}} \approx \mathcal{T}/M$, and, in turn, $\mathcal{T}_{\mathrm{s}}$ will depend on the state of folding along the tetramer.

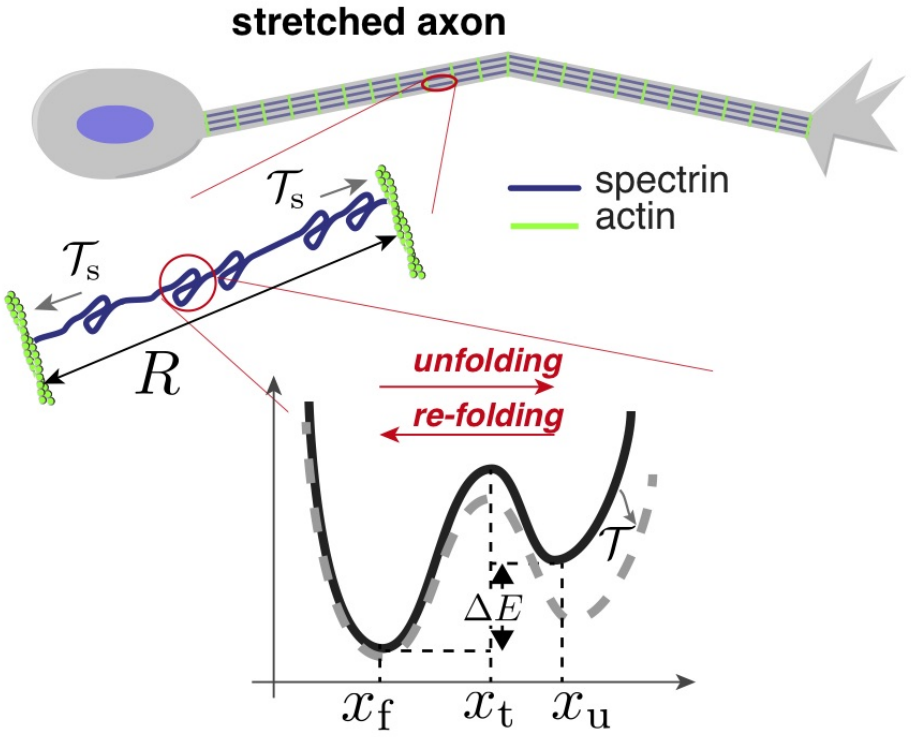


FIGURE 4.18: Schematic illustration of stretched axon, showing unfolding and re-folding of spectrin repeats as underlying tension relaxation mechanism. Zoom shows schematic illustration of energy landscape for a unfolding/re-folding of a spectrin repeat.

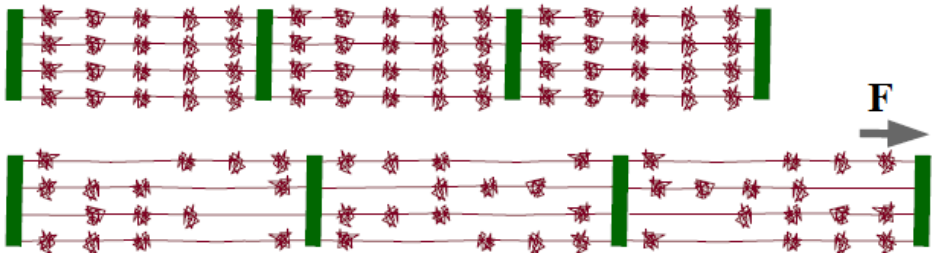


FIGURE 4.19: An axon can be considered as spectrin tetramers in parallel as well as in series with actin rings in between. When force is applied an axon, the folded domains unfolds randomly along the axon and stored energy dissipate. The observed tension relaxation can be accounted for unfolding and refolding events happening inside the axonal cytoskeleton.

In a mean-field approach, $N_u(t)$ evolves according to the kinetic equation

$$\frac{dN_u}{dt} = \nu_u(N - N_u) - \nu_f N_u \,, \tag{4.1}$$

where $\nu_u$ and $\nu_f$ are, respectively, the unfolding and folding transition rates, and are assumed to depend on the tension [112, 113]:

$$\nu_{\mathrm{u}}(\mathcal{T}) = \tau_0^{-1}\exp\left[\frac{\mathcal{T}(x_{\mathrm{t}} - x_{\mathrm{f}})}{Mk_{\mathrm{B}}T}\right]$$
$$\nu_{\mathrm{f}}(\mathcal{T}) = \tau_0^{-1}\exp\left[\frac{\Delta E + \mathcal{T}(x_{\mathrm{t}} - x_{\mathrm{u}})}{Mk_{\mathrm{B}}T}\right]. \tag{4.2}$$

Here, the inverse time constant $\tau_0^{-1}$ is the unfolding rate at zero tension. Furthermore, $x_{\mathrm{f}}$, $x_{\mathrm{t}}$, and $x_{\mathrm{u}}$ are position-related reaction coordinates in the folded, transition, and unfolded states, such that $x_{\mathrm{u}} > x_{\mathrm{t}} > x_{\mathrm{f}}$ (Fig. 4.18) Finally, $k_{\mathrm{B}}$ is Boltzmann's constant, $T$ is temperature, and $\Delta E > 0$ is the energy difference between the $u$ and $f$ states.

In the next step, we model the force-extension relation of a spectrin tetramer using an interpolation formula from the wormlike chain (WLC) model for polymer elasticity [111, 114]:

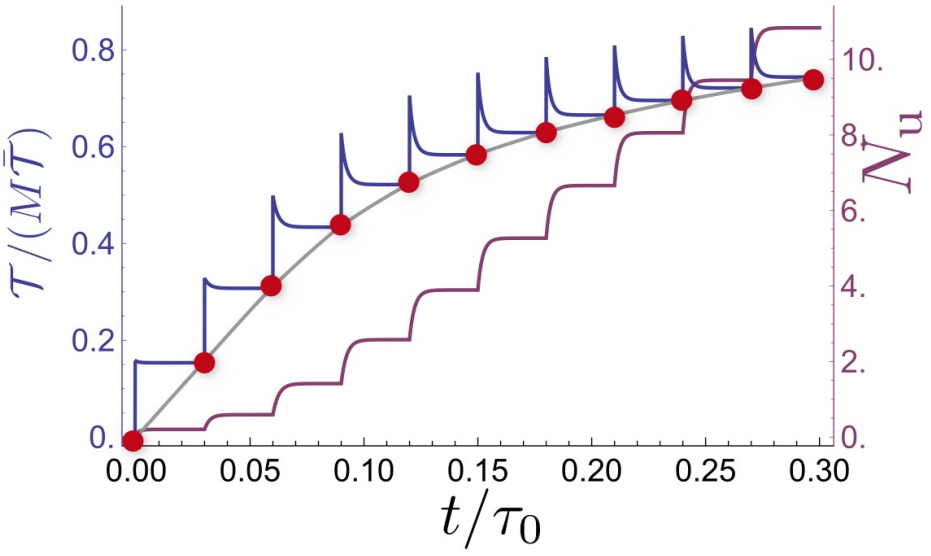


FIGURE 4.20: Model calculation for a single spectrin tetramer for multiple step-strain protocol. Tension versus time (blue) shows a jump after strain increment is applied, followed by relaxation to a steady state value (red points, passed through by the equilibrium force versus extension curve (gray)). This relaxation coincides with progressive spectrin unfolding, as indicated by the number of unfolded repeats, $N_{\mathrm{u}}$ (burgundy). Note that the tension scale used is $\bar{\mathcal{T}} \equiv k_{\mathrm{B}}T/l_p$.

$$\mathcal{T}(R) = \frac{Mk_{\mathrm{B}}T}{l_{\mathrm{p}}}\left(\frac{1}{4(1 - R/\mathcal{L})^2} - \frac{1}{4} + \frac{R}{\mathcal{L}}\right), \tag{4.3}$$

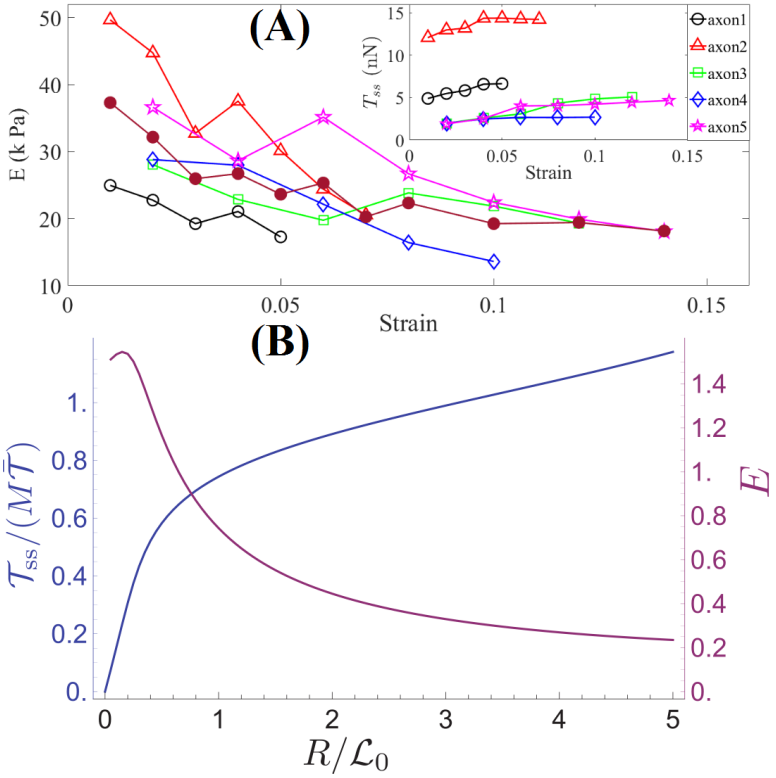


FIGURE 4.21: (A) Strain softening behaviour observed in axons experimentally and steady state tension response which tends to saturate at higher strains (inset). (B) Equilibrium tension and Young's modulus versus extension curve for a single spectrin tetramer. The tension curve (blue) is obtained by solving Eqs. 1-4 at equilibrium ($dN_u/dt = 0$). The tension is normalized by the number of spectrin molecules per cross-section, $M$, and by the tension scale $\bar{\mathcal{T}} \equiv k_B T/l_p$. The Young's modulus curve (purple) is obtained by dividing the normalized tension by the spectrin end-to-end extension $R/\mathcal{L}_0$. The small bump in the $E$ vs. extension curve is related to the entropic elastic contribution in the wormlike chain interpolation formula (Eq. 4.3). Since axons are under tension at rest, with a distance of $R \approx 200$ nm between adjacent actin rings, this bump is not seen experimentally.

where $R$ is the end-to-end extension of the tetramer; $l_p$ is its persistence length; and $\mathcal{L}$ is its contour length. A key ingredient in the model is that $\mathcal{L}$ is not constant, but rather depends on the folding state of the molecule. That is,

$$\mathcal{L} = \mathcal{L}_0 + N_u \, \Delta\mathcal{L} \, , \tag{4.4}$$

where $\mathcal{L}_0 \approx 200$ nm is the contour length with all repeats folded and $\Delta\mathcal{L} \approx 30$ nm is the gain in length when a repeat unfolds [111]. Model calculations were done using the following parameters: $k_B T = 4$ pN.nm, $l_p = 0.6$ nm (average of values obtained from [111]), $\mathcal{L}_0 = 200$ nm, $\Delta\mathcal{L} = 31.7$ nm, $N = 76$, $x_t - x_f = 3.5$ nm, $x_u - x_t = 3.5$ nm, $\Delta E = 8$ pN.nm.

With this model in hand, we can readily understand the axon tension relaxation and strain-softening seen experimentally. By solving Eqs. (4.1)-(4.4) for a sequence of equal strain steps, each applied at constant time intervals, our model can qualitatively reproduce the axon stretch response. Following a jump in strain, the tension rises quickly and then relaxes, as spectrin repeats progressively unfold (Fig. 4.20). At long times after the strain step, the tension tends to a steady state $\mathcal{T}_{\rm ss}$, such that the locus of values of $\mathcal{T}_{\rm ss}$ follows the steady state tension versus strain curve (red dots in Fig. 4.20). This reflects the tension buffering behaviour seen in Figs. 4.21A, 4.11 and Ref. [112]. The curve reveals the characteristic strain-softening effect predicted by this model: for small extension, $R$, most repeats are folded, $N_{\rm u} \approx 0$, and the tetramer behaves like a polymer with fixed contour length and with an elastic response $\mathcal{T} \propto R$. For larger $R$, the number of unfolded repeats increases, as does the contour length and, so to speak, the reference state of the polymer. This slackening of the tetramer gives rise to softening with increasing strain (Fig. 4.21).

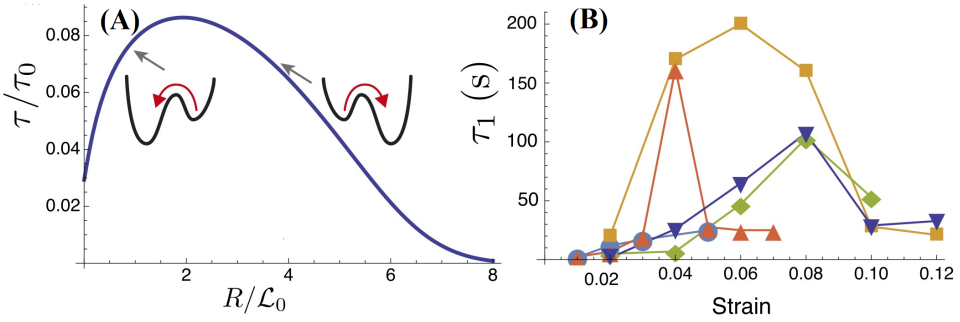


FIGURE 4.22: (A)Tension relaxation after a small change in applied strain is approximately exponential, with a relaxation time, $\tau$, that depends non-monotonically on strain. The inset cartoons reveal that $\tau$ is largely controlled by re-folding at low strain, and by unfolding at high strain. The relaxation time shows non-monotonic behaviour on imposed strain. (B) Fitting the tension relaxation data to a double-exponential function we obtain two relaxation times– a long and short relaxation time which are qualitatively similar dependence on strain as with the model.

### 4.10.1 Dependence of tension relaxation time on strain

To accounts for the non-monotonic dependence of the relaxation time on strain, at steady state the model axon, is subjected, at some $t = 0$, to a sudden, but small (constant) change in extension, from $R$ to $R+\Delta R$. Following this change in strain,

$\mathcal{T}$ and $N_{\mathrm{u}}$ change from their steady state values, $\mathcal{T}_{\mathrm{ss}}$ and $N_{\mathrm{u,ss}}$, at extension $R$ by small amounts $\Delta\mathcal{T}$ and $\Delta N_{\mathrm{u}}$. Right after the change in strain, there is an elastic increase in tension, followed by relaxation, as spectrin repeats gradually unfold as seen in Fig 4.20. By linearising Eqs. 4.1-4.4 around the steady state at $R$, we find an exponential relaxation for $\Delta\mathcal{T}$ and for $\Delta N_{\mathrm{u}}$, with inverse time constant

$$\tau^{-1} = (\nu_{\mathrm{u}} + \nu_{\mathrm{f}}) + \left.\frac{\partial \mathcal{T}}{\partial N_{\mathrm{u}}}\right|_R \left(\frac{-\nu_{\mathrm{u}}(N - N_{\mathrm{u,ss}})(x_{\mathrm{t}} - x_{\mathrm{f}}) + \nu_{\mathrm{f}} N_{\mathrm{u,ss}}(x_{\mathrm{t}} - x_{\mathrm{u}})}{M k_{\mathrm{B}} T}\right), \quad (4.5)$$

where the transition rates $\nu_{\mathrm{u}}$ and $\nu_{\mathrm{f}}$ and the partial derivative of $\mathcal{T}$ with respect to $N_{\mathrm{u}}$ are all evaluated at the steady state with extension $R$. We can obtain a simpler expression for the relaxation time, which then allows us to understand its non-monotonic dependence on strain, as seen experimentally. Noting that $\partial\mathcal{T}/\partial N_{\mathrm{u}} \sim \mathcal{T}\Delta\mathcal{L}/\mathcal{L} \sim 0.03\,\mathcal{T}$ for $N_{\mathrm{u}} \sim 30$, we can show numerically using Mathematica (Mathematica 11.0. Wolfram Research, Inc., Champaign, Illinois, 2018) that the second term in Eq. (4.5) is small compared with the first. Thus, we find that, to a very good approximation, $\tau$ can be calculated as below Eq. 4.6. We find exponential relaxation with time constant -

$$\tau \simeq \frac{1}{\nu_{\mathrm{u}} + \nu_{\mathrm{f}}}\,. \quad (4.6)$$

Here, $\nu_{\mathrm{u}}$ and $\nu_{\mathrm{f}}$ are the transition rates in the state $R$.

Thus, Our model predicts surprising behaviour in the axon tension relaxation, specifically a non-monotonic dependence of the relaxation time on strain (Fig. 4.22).

Remarkably, this expression captures very well the experimental dependence of the tension relaxation time with strain (Fig. 4.22B), and the underlying physics can be readily understood. For small $R$, given that $\Delta E/k_{\mathrm{B}}T > 1$ [112], $\nu_{\mathrm{u}} \ll \nu_{\mathrm{f}}$, and thus $\tau \approx 1/\nu_{\mathrm{f}}$. That is, the folding rate initially dictates the rate of tension relaxation. Since, the folding rate decreases with tension, it then follows that $\tau$ increases with $\mathcal{T}$, or equivalently with $R$. For large $R$, the energy landscape for unfolding and re-folding becomes sufficiently tilted that $\nu_{\mathrm{u}} \gg \nu_{\mathrm{f}}$ (Fig. 4.22A). Then, $\tau \approx 1/\nu_{\mathrm{u}}$, and since $\nu_{\mathrm{u}}$ increases with $\mathcal{T}$, we find that the relaxation time decreases with strain.

In summary, our model predicts key experimental features like the viscoelastic solid-like response and the non-trivial dependence of the tension relaxation time, which first increases and then decreases at larger strain. These two responses are possible signatures of the role of spectrin unfolding and re-folding in tension relaxation, and argues against a few other possible mechanisms. For example, a tension relaxation scenario involving actin-spectrin unbinding—or any other crosslink unbinding—would lead to a relaxation time that monotonically decreases with strain and a long time fluid like response. The minimal model, we present ignores possible contributions from other axonal cytoskeletal elements. But by knowing the fact that the axonal structure is very complex [42], a composite model would be needed to account for the role of microtubules and other filaments response due stretch.

### 4.10.2 Contribution from other filaments/ Microtubule based models

Microtubules sliding based models has been developed in past to account for stretch injuries in axons. Both the models by Shenoy group [79] and Kuhl group [80] have assumed that there are parallel microtubules filaments in bundle and are connected by a stabilizing crosslinking protein called Tau. Rooij *et al.* [80] modelled the axon as a parallel arrangement of longitudinally aligned microtubules that are crosslinked by tau protein. The crosslink can detach and reattach according to the Bell model under external force. Axonal damage is defined as the loss in axon stiffness triggered by a gradual loss of crosslinks that promotes microtubule depolymerization and destabilizes the axonal cytoskeleton. Shenoy group [79] model is motivated by [21] where microtubules are disrupted after sudden stretch. This study also makes an assumption of tau protein detachment and reattachment while axon is under stretch. They find that MTs disintegrate in the form of rapture or detachment from the bundle.

These models assume that axonal damage is solely caused by the disruption in tau protein crosslinks and ignored other filaments as well as other crosslinking proteins. We made an estimate of contribution from microtubules in axonal mechanical behaviour. A part of the mechanical stress is expected to be borne by microtubules

which form bundles cross-linked by Microtubule Associated Proteins, tau being a major component of this in axons. Assuming affine deformation of the microtubule bundle, we can estimate the relative sliding between adjacent microtubules as $\delta x = (L - L_0)/n$, where $n$ is the number or microtubules needed to span the length of the axon. Taking an average microtubule length of 4 μm [115], a typical axon length of $L_0 = 200$ μm, and an applied strain of 10%, we get a relative displacement for microtubules as $\delta x = 400$ nm. Taking tau to be the major cross-linking protein in axon, and a relaxed tau-tau dimer length of $l_0 = 80$ nm, each dimer is stretched by an amount $\sqrt{l_0^2 + (\delta x/2)^2} - l_0 \simeq 135$ nm. At such displacements, tau proteins may either stretch without dissociating or stretch and dissociate depending on the loading rate and strain, as modelled in detail in Ref. [79]. It has been shown that such a bundle cannot sustain load over long times as it behaves as a fluid by allowing microtubules to slide [79]. The changes in the zero-frequency moduli after microtubules perturbations can be accounted for by incorporating cross-links with long bound-time or can occur via indirect mechanisms. For example, it has been shown that disruption of microtubules using Nocodazole causes a decay of the actin-spectrin skeleton and stabilizing the filaments using Taxol increases the occurrence of this periodic scaffold [14]. There is also experimental evidence that microtubules are disrupted under fast loading reaching high strains [21]. Such catastrophic decay of microtubules makes the mechanical support rendered by the actin-spectrin skeleton even more critical in ensuring axonal integrity, especially under conditions similar to that causes impact induced brain damage.

## 4.11 Conclusion and Summary

We have shown in the last chapter that F-actin is a major contributor to axonal mechanical behaviour due to stretch and axons show strain softening behaviour. In this chapter, we have shown that spectrin is also major contributor to axonal mechanics.

First, using super-resolution (STED), we imaged control axons which shows rings all along axons (Fig. 4.4). We show that with days in culture, actin-spectrin

skeleton becomes prevalent and is shown by others as well [14, 41]. Our super-resolution experiments either with Taxol or with Jasplakinolide showed rings all over axons (Fig. 4.5, 4.6). These results are in good agreement with our observation that Taxol or Jasplakinolide treated cells show strain softening but with a higher modulus compared to control. Our super-resolution images and quantification of Lat-A treated cells show that the periodic structure is largely disrupted (Fig. 4.7). In fact, Lat-A treated cells show significant reduction in steady state tension which suggests that reduction in steady state tension is due to disruption of MPS.

Quantification of spectrin intensity levels in spectrin specific MO cells (knock-down cells) and control MO cells show significant reduction in $\beta$-II spectrin immunolabelling intensity distribution levels in spectrin knock-down cells (Fig. 4.14). Next, we performed force measurements on spectrin knock-down cells and control MO cells. We found a striking result that spectrin knock-down cells show significant reduction in steady state tension compared to control MO cells.

Motivated by these results, we then developed a minimal model by only considering actin-spectrin skeleton (for simplicity). Our model considers the domain unfolding-refolding of spectrin repeats which are force dependent. While a stretch is applied on an axon there are multiple unfolding events happens due to stretch and energy stored in this domains release and correspondingly, the tension relaxation behaviour is observed (Fig. 4.20). We show that the modulus diminishes with applied strain which is good agreement with observed results (Fig. 4.21). We also show that the relaxation time is non-monotonic on imposed strain which is similar to the relaxation time obtained by fitting tension relaxation data (Fig. 4.22). The relaxation time behaviour, initially dominated by refolding events and later dominated by unfolding events which can explain the non-monotonous behaviour of relaxation times (Fig. 4.22).

An order of magnitude estimate of the maximum possible contribution coming from spectrin tetramers to axonal tension can be made as follows. If we assume the width of a spectrin molecule to be 10 nm, and take a typical axon diameter as 1 µm, the maximum number of spectrin molecules (for a mature axon, say) in a cylindrical cross-section can be estimated to be about $M \sim 300$. A more

conservative estimate can be made using available data from RBCs [93], where the actin-spectrin junction is reported to be 35 nm in width (with each junction connecting to an alpha and a beta spectrin), and this gives $M \sim 180$. If we now take the force needed to unfold a spectrin subunit from AFM experiments as $f_s \simeq 30$ pN [111], we can estimate the axonal tension to be of the order of $\mathcal{T}_{ss} \sim 6-10$ nN. This is in a reasonable range when compared to the experimentally measured plateau tension for 4-DIV axons (Fig. 4.11). Although this is only a rough estimate, and the exact number may depend on the details of the actin rings, it suggest that spectrins could make a significant contribution to axonal mechanics.

Our experiments and theoretical analysis suggest that spectrin can contribute to strain-softening via force-dependent unfolding and re-folding of spectrin repeats. A consequence of the force-assisted unfolding of spectrin domains is that the tension versus strain response at steady state exhibit an extended region where the tension is only weakly dependent on the strain (Fig. 4.21, 4.11). This can have important functional significance as the actin-spectrin skeleton can protect axons against stretch deformations by acting as a tension buffer, or "shock absorber".

In conclusion, we have shown that spectrin is a cytoskeletal component of axons which also plays a major role in axonal mechanics via actin-spectrin lattice to protect the neurons from the mechanical damage.

# Chapter 5

# Mechanical Properties of Spider Silk

## 5.1 Introduction and motivation

Spider silk is one of the strongest bio-material known till date. Silk exhibits unique mechanical properties such as high tensile strength, large extensibility, supercontractility, etc.[6, 116, 117]. The mechanical properties of spider silk had evolved over millions of years. Basically, spiders spin their webs to catch flying prey/insects. When a prey hits the web, its kinetic energy is transferred to the web, which dissipates over time. There should be an optimization of the elasticity and viscosity to dissipate the energy for the survival of the web. A typical web structure is shown in Fig. 5.1. There are more than 40,000 spider species found in nature [5]. Having these many varieties, the mechanical properties of spider silk also vary widely in terms of tensile strength and toughness. Social spiders live in a group called colonies and form a two-dimensional sheet web architecture, which enables us to easily investigate the mechanical properties of these spider silks [118, 119].

Spiders produce silk and store in the silk gland in the form of a dope and spin fibers using the dope whenever required via specialized orifices called spinnerets located on its abdomen (Fig. 5.2). Typically, each spider is capable of producing

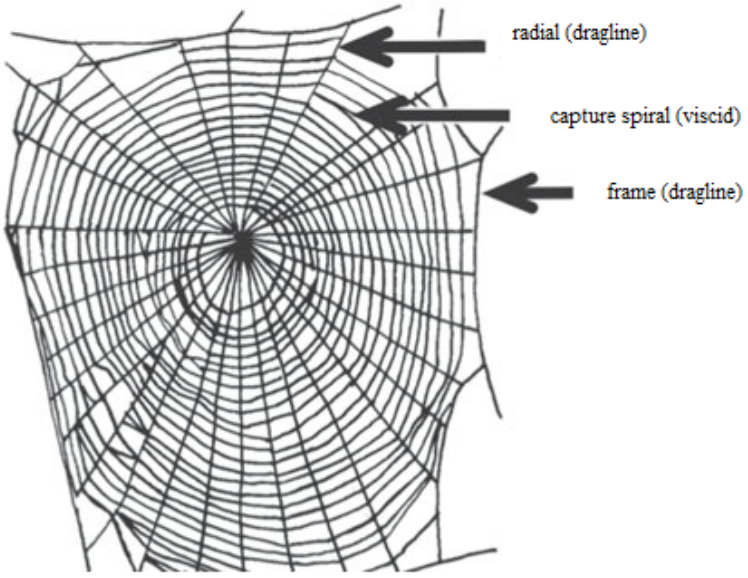


FIGURE 5.1: **Web architecture** Representative orb-web showing the main structural elements. The anchor threads attach to frame threads (dragline silk), which form the periphery of the web. The radial threads (dragline silk) attach to the frame. During web construction, the radials are overlaid with a widely spaced, non-viscid temporary spiral. This is then replaced by the final, closely spaced, viscid capture spiral, creating a more or less evenly spaced mesh (figure and modified caption are adapted from Harmer et al. [116]).

up to seven different silk types, each of which is engineered for a particular function through millions of years of evolution [5, 116, 117, 120].

Dragline silk is produced on a large scale by all spiders, as it forms the main structural part of any spider web and is also used by spiders to escape from predators [5, 116, 117, 120]. It is the most easily procurable and widely studied among all other spider silk types [6, 116, 117]. Capture silk is another widely studied form of spider silk. There are two major types of capture silk – cribellate silk and viscid silk [116], and there are some studies done on both capture silk types [121–125]. Other less studied silk types are Acniform silk, Tubiliform silk, and Piriform silk [126, 127]. The major limitation to study these silk types is the lack of their abundance and difficulty in extracting good quality samples. A typical stress-strain of dragline and capture silk is shown in Fig. 5.3.

As mentioned before, spider silk is an outstanding material, and that's the reason it is of interest to many scientists to study its remarkable mechanical properties. The main challenge is to make a biodegradable material having mechanical properties

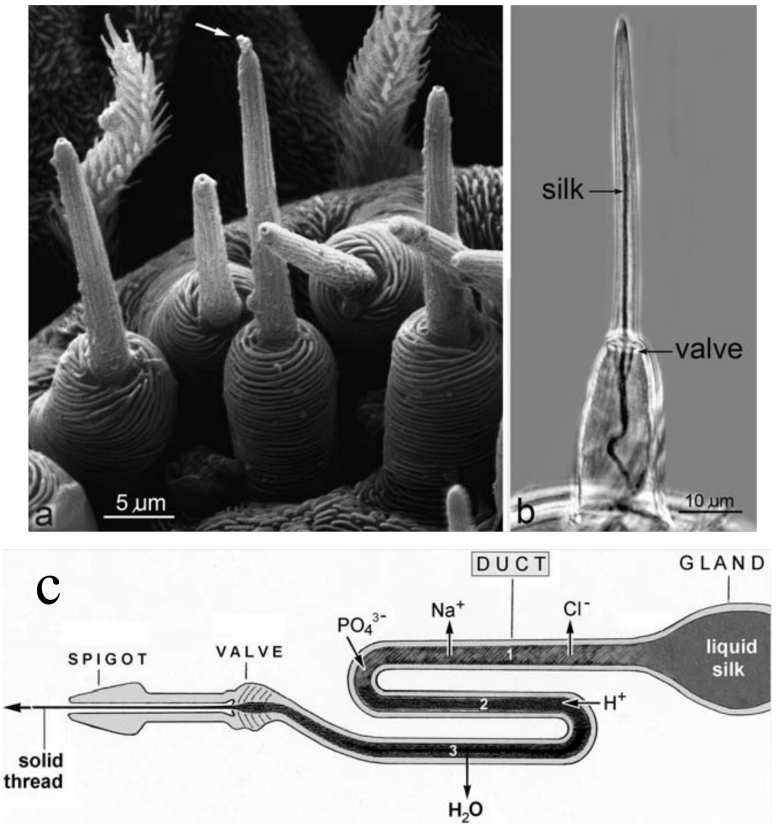


FIGURE 5.2: **Production of silk**:(a) Several spigots of piriform glands on the anterior spinneret of the spider Amaurobius. While most spigots exhibit a distinct terminal pore, one shows remnants of exuding silk (arrow) ( b) Spigot from a spinneret of the jumping spider Marpissa. The silk thread inside the glandular duct is clearly visible when using a phase-contrast microscope. (Photo: Erb.) (c) Diagram of dragline formation. The liquid silk coming from the gland undergoes an ion exchange within the long duct system, and water is removed. Silk proteins gradually align in parallel (1-3) and get packed tightly; the silk turns solid when pulled out of the spigot (arrow) (After R. S. Wilson, 1962b; Lewis, 2006; Scheibel 2009) (image and caption adapted from Biology of Spiders, Foelix [5]).

of spider silk-like high tensile strength and large extensibility. Materials like steel have high tensile strength but limited extensibility. Steel has a modulus of about 200 GPa, Kevlar has around 100 GPa, and dragline silk has few tens of GPa [6].

## 5.2 Structure, type, and properties of spider silk

Several studies have used X-ray, Raman spectroscopy, NMR, etc. to reveal the molecular structure of the silk [129–134]. To reproduce a material like spider silk, it very important to understand the ultrastructure of the silk. The typical ultrastructure of dragline silk has been shown in Fig. 5.4.

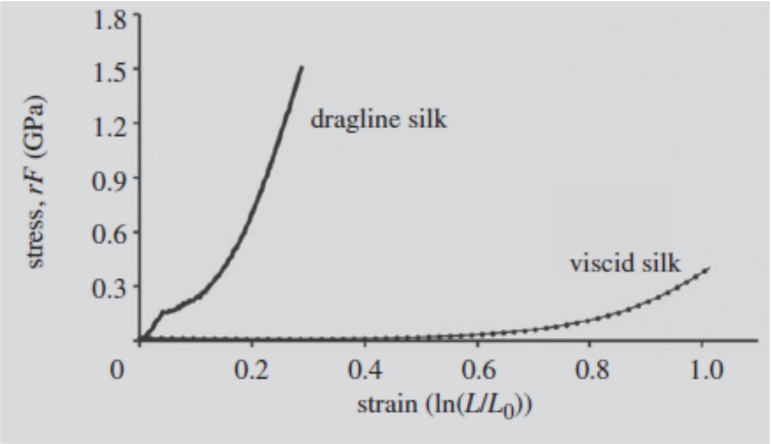


FIGURE 5.3: **Typical stress–strain curve** Representative stress-strain curves for dragline silk and viscid silk in the web of *A. keyserlingi*. The high tensile strength and stiffness of dragline silk allow it to absorb the energy of prey impacts. The extreme compliance of viscid silk, on the other hand, results in lower tensile strength but much greater extensibility (and lower stiffness) than dragline silk. This allows viscid silk to dissipate energy via thread displacement and stretching and prevents insects from ricocheting out of webs. Viscid silks do not show an initial elastic phase, but instead, exhibit high extensibility (more than 200-300%) before an exponential increase in stiffness just prior to failure (image and caption courtesy: Harmer et al. 2011 [116]).

Major Ampullate silk is made up of a lipid-rich layer and a glycoprotein-rich skin covering a fibrous outer and inner core. The core is composed of two types of proteins, or spidroins, called MaSp1 (derived from major ampullate spidroin 1) and MaSp2 (major ampullate spidroin 2) [135, 136]. These proteins contain ordered crystalline and disordered (amorphous) regions. The crystalline regions contain stacked $\beta$-sheets, whereas the amorphous regions arranged as a matrix of helices $\beta$-turns or $\beta$-spirals, and other protein secondary structures depending on the amino acid composition [128].

## 5.3 Effects of Humidity, Temperature, etc. on spider silk

Several environmental factors, such as humidity [137], temperature [138], UV radiation [139], etc. affect the mechanical properties of spider silk. At a fixed temperature, the stiffness of the fiber decreases with an increase in humidity. Conversely, while humidity is fixed, the stiffness of the fiber decreases with rising in temperature [138]. In highly humid or in wet conditions, the properties of dragline silk change significantly. The exposure of water to dragline silk fibers causes an

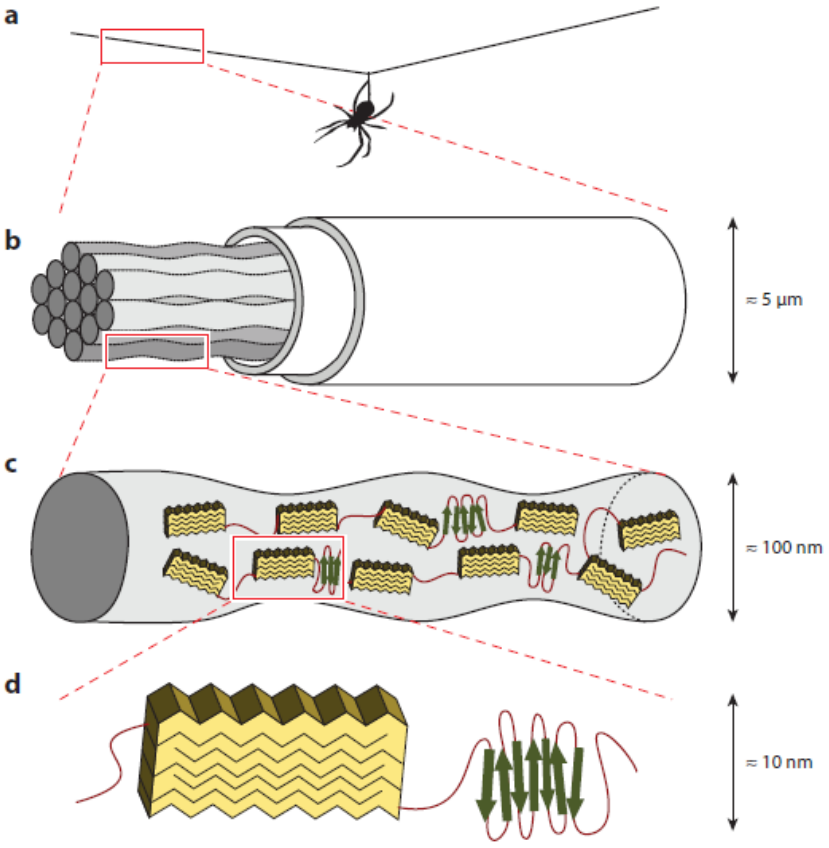


FIGURE 5.4: **The structure of spider silk, from macro to micro-structure** (a) A single thread of Major Ampullate (dragline silk) is shown which is composed of (b) skin-covered fibrils and small parallel threads (c) one single thread is conglomerates of proteins called spidroins (d ) these proteins consist crystalline $\beta$-sheets separated by protein chains of variable structure representing the so-called amorphous region. The scale arrows represent the approximate sizes of the structures (image courtesy: Blamires *et al.* [128], with modified caption).

increase in the diameter of the fiber and a decrease in its length. The effect of reduction in length is commonly referred to as supercontraction [140]. Apart from these, degradation of proteins, diet, reeling speed, etc. too affect the silk mechanical performance [129, 141]. Exposure to UV radiation results in the degradation of amino acids via emission of ammonia gas from the fiber [139]. Thus, it is extremely important to test the mechanical properties of silk fibers in control environmental conditions.

## 5.4 Previous studies on mechanical responses of spider silk

The spider silk is an interesting biomaterial with remarkable mechanical properties that have attracted a lot of recent interest. Typically to test the mechanical properties of single silk fiber, it is pulled at a constant strain rate while the force on the fiber is measured. Using this information, physical quantities are analyzed, such as stress (force per unit area) and strain (relative elongation). Stress vs. strain curve is plotted, and different properties such as stiffness, extensibility, and toughness are determined from this curve. These quantities are defined as – stiffness or Youngs modulus, which is the slope of the initial linear regime of the stress vs. strain curve; extensibility is the strain at fracture; and toughness is defined as the area under the curve [6, 116]. Another type of experiment is done by applying loading and unloading cycles. The closed-loop area of the stress-strain curve gives the energy dissipated for one such cycle, due to molecular friction during loading and unloading.

There are many studies on the mechanical properties of spider silk, where silk is continuously pulled until it breaks. The pulling of the silk has been done at different pulling rates as well. From the stress-strain curve, modulus has been calculated in the linear elastic limit. The silk shows an initial linear regime up to yield point followed by a softening regime. After softening, silk shows a strain-stiffening response until it breaks (or stick-slip happens). This is the typical response shown by many studies on dragline spider silks [6, 116]. The capture silk shows lower tensile strength but much greater extensibility than dragline silk, which allows them to withstand much larger stretchability and dissipate the energy transferred by prey. On the other hand, stress-strain curves for dragline silks typically show an initial phase of high stiffness before yielding at higher strain values [116]. A typical pulling response of silk is shown in Fig. 5.5.

Investigations of silk mechanics are typically performed by generating large force-extension loops by applying cyclic linear stretching or single stretch up to the yield or breakpoint, as described earlier. However, a full characterization of the linear and non-linear rheological properties of single strands of silk requires the ability to

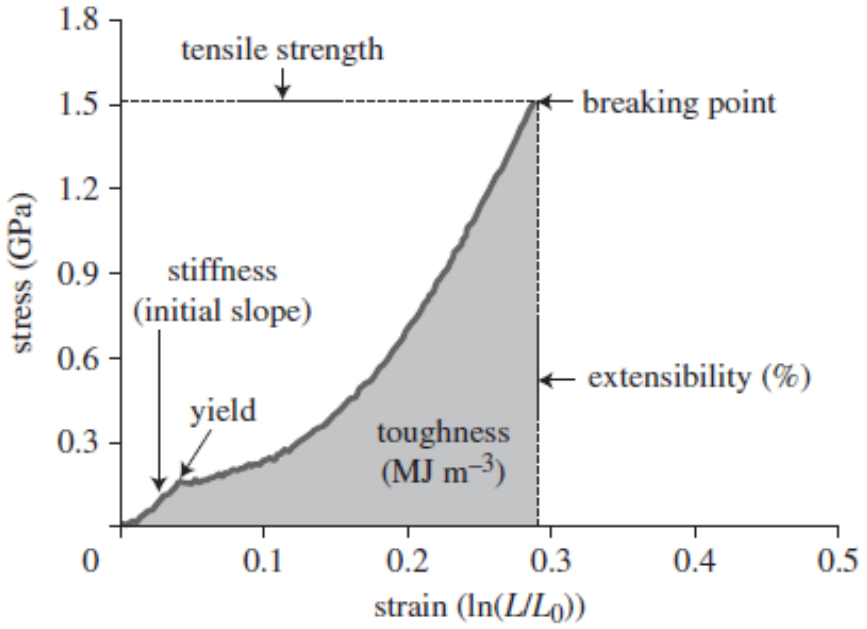


FIGURE 5.5: Representative stress-strain curve of silk showing the key measures of biomechanical properties in spider silks. The mechanical properties are defined as stress, calculated as force divided by the cross-sectional area of the fiber. Tensile strength is the stress at the breaking point of material under uniaxial loading. Extensibility describes the stretchiness of a fiber; for example, the percentage increase in a fibers length at breaking when compared with its original length. Stiffness is defined by Youngs modulus and is calculated from the slope of the initial elastic region of the stress-strain curve. Yield is the point where a fiber transitions from elastic (and reversible) deformation to plastic deformation. Toughness is the energy required to break a thread. It is calculated as the area under the stress-strain curve(figure and modified caption adapted from Harmer *et al.* [116]).

do a variety of rheological protocols in extension mode, which are limited by available techniques. To overcome this, we have investigated silk from social spider S. *sarasinorum* using an improved version of the Micro-Extension-Rheometer (MER) that we had developed earlier. Social spiders give us the advantage that they can be easily reared under controlled laboratory conditions to obtain silk fibers of controlled quality, like feeding, humidity, temperature, sunlight, etc., affect silk mechanical properties. In order to obtain the elastic moduli about equilibrium states with different amounts of pre-strain, we used a sequential step strain protocol where the silk is pre-strained by increasing amounts, and the modulus is measured at steady-state using small amplitude strain oscillations. We observe that silk exhibits an initial strain-softening for up to about 4% strain and then begin to stiffen with increasing strain. In addition, the stress relaxation corresponding to each applied strain step is used to obtain the relaxation times as a

function of strain. The relaxation times thus obtained increase with increasing strain and tend to saturate at high strains. Using a Fourier analysis method, we also extract the frequency dependence of the elastic and viscous moduli from the relaxation process. The rheological data presented here will aid in relating molecular level processes to the unique macroscopic viscoelastic properties of silk.

Social spiders species *Stegodyphus sarasinorum* are of advantage, as they exhibit nest-site fidelity and thus can easily be maintained under controlled laboratory conditions (light, humidity, temperature, etc.), which could affect silk fibers mechanical properties. One of the novelties of our study is that, so far, only silk of solitary spider species have been investigated. Social spider colonies can consist of over a hundred individuals, and their webs can be very large and found to spread over a meter under field conditions. This makes it interesting as a model to study the physical properties of their webs. Since silk is so expansive, it is also re-used by subsequent generations with continuous repair and maintenance.

## 5.5 Material and Methods

### 5.5.1 Preparation of silk samples

**Colony setup:** A total of three spider colonies were collected from Somapura, Karnataka, and Kuppam, Andhra Pradesh, India. In the field, social spiders construct sheet webs on the surface of which prey are intercepted 5.7 (Also see for details [142, 143]). The sheet web is anchored to plants by dragline silk. The spiders live within nests made of dense silk (also called retreats) and used by spiders to rest or hide, and they come out to hunt when sense vibrations from an entangled prey. From these colonies, a group of 20 spiders was randomly selected. Each such group was introduced on a square metal wire frame (45cm x 45cm; wire dia. 0.1cm), as shown in Figs. 5.6 and 5.7(B). To mimic retreats, a small amount of retreat material was placed between two cardboard sheets (6cm x 6cm) attached to the metal frame such that there is a gap between the two sheets Fig. 5.6. Spiders were introduced into this gap, and they reside there when inactive. Usage of a thin frame enabled spiders to build a two-dimensional web (Figs. 5.6(A), 5.7(B)),

and the extraction of silk was easier. The metal frames were suspended on a stand (Fig. 5.6(B)). A thick layer of petroleum jelly was applied at the point of suspension to avoid any ant attack. This also prevents spiders from escaping from the frame. The whole setup was kept in a room with enough ventilation and with 12h:12h day-night cycle. Spiders were kept undisturbed for three days, before the silk extraction process. During the whole experiment, each group of spiders were watered twice a week using a water sprayer and were fed two grasshoppers in a week.

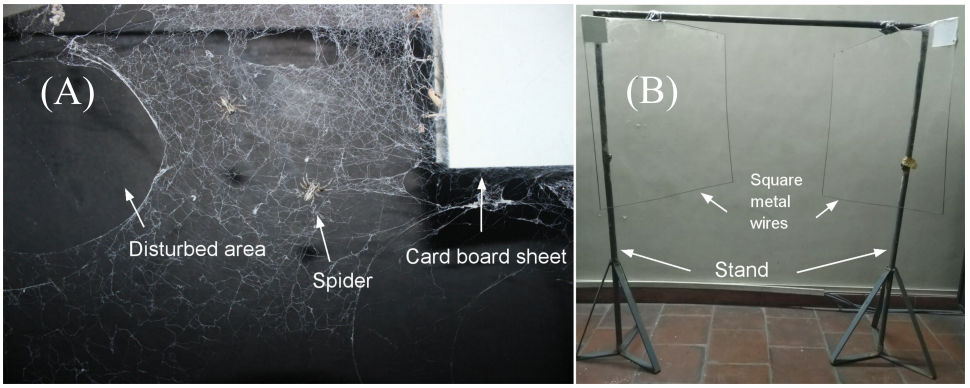


FIGURE 5.6: **Setting up spider colony** (A) The images on the left shows the disturbed area where the spider will spin new silk and the cardboard where spiders reside while taking rest (B) The image shows the two-dimensional square metal wires on which spiders make their colony.

### 5.5.2 Silk extraction process

Two types of silks were extracted in this experiment–dragline and cribellate silk (Fig. 5.7(C)). Dragline silk is the main structural silk, and cribellate silk is the capture silk in *S. sarasinorum* webs. In order to obtain fresh silk samples every day, a small area of the spider web was disturbed one day prior to silk collection. Spiders spun fresh silk strands in the disturbed area while repairing the web overnight. For extraction, a Y-shaped cardboard frame (width: 1.5 cm) (Fig. 5.7(D)) with a small speck of super-glue (Fevi kwik$_{®}$) on both the arms of the "Y" was stuck to the silk fiber on the web. After a few seconds, the surrounding fibre was cut using a pair of scissors. This process ensured that the pre-tension of the silk is not lost. After this, the Y-frame (with the silk fibre on it) was embedded on a

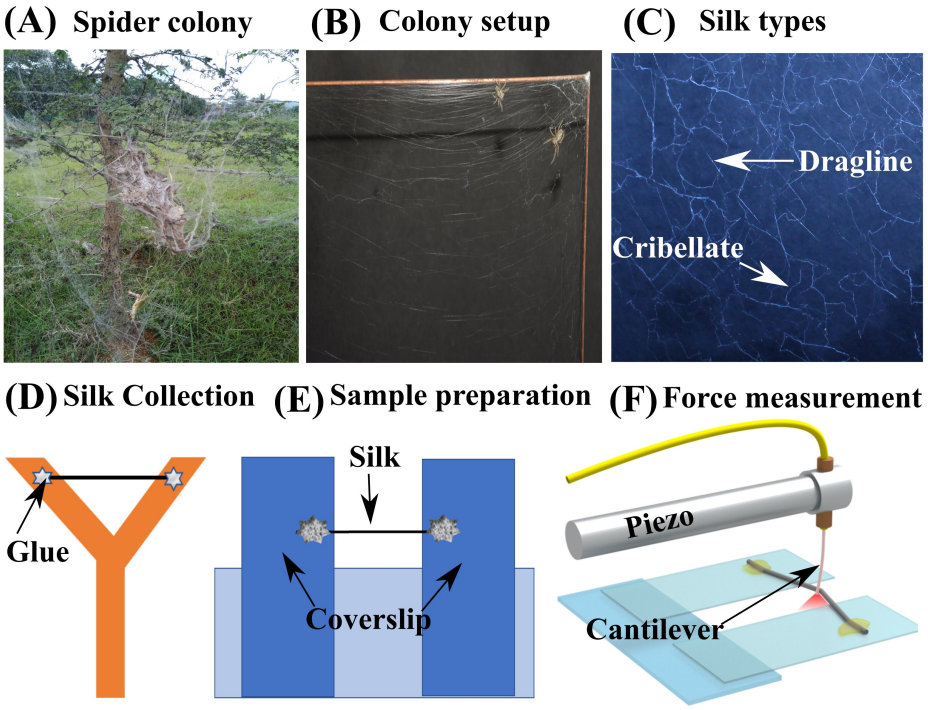


FIGURE 5.7: **Extraction of silk for force measurements** (A) Photograph of a web of social spider Stegodyphus sarasinorum in the wild. (B) Photograph of spiders with their web built on a metal wire frame as detailed in the Material and Methods. (C) Image showing an expanded view of the web with a dragline and cribellate silk indicated by the labels. (D) Schematic of a silk strand transferred to a Y-shaped cardboard frame. (E) Schematic of the silk strand after it has been transferred to a frame made of two coverslips attached to a glass slide. (F) Schematic of a silk fiber stretched using an optical fiber cantilever attached to piezo.

thermocol sheet and stored was in a plastic box before performing tensile measurements. Except for measuring age effects, all samples were studied within a day of the extraction.

### 5.5.3 Sample preparation

For performing force measurements, we prepared a sample mount consisting of two microscope coverslips placed side by side and parallel to each other with a gap of 300-500 µm. The two coverslips were held together by a glass slide to which they were glued (Fig. 5.7(E)). Silk fiber on the Y-frame was placed over the coverslips such that the fiber forms a bridge between the two coverslips, and was glued close to the edges of the coverslips. The sample was kept for drying at room

temperature (24–26 °C; rel. humidity 50–60%). The sample was then transferred on to the microscope stage for rheological measurements.

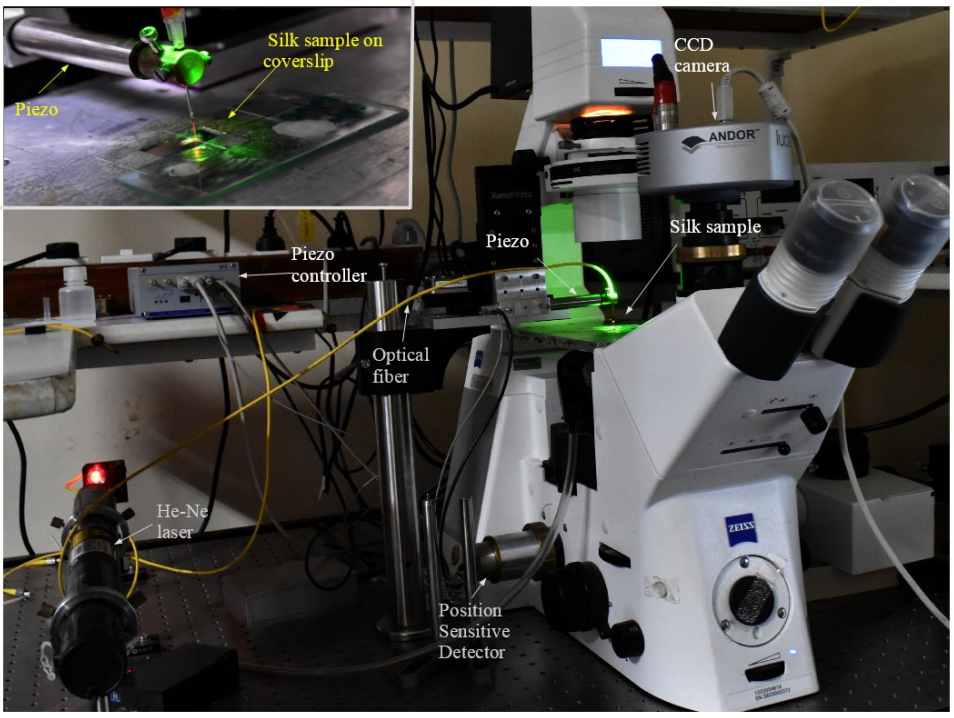


FIGURE 5.8: Photograph of the optical fiber-based force apparatus Micro-Extension-Rheometer (MER) used to investigate the mechanical properties of spider silk. The piezo drive and the Position Sensitive Detector (PSD) are interfaced with a computer to operate the setup in a feedback strain control mode. More details are described in the main text. The inset shows the closed view of the sample, which is being pulled with optical fiber.

### 5.5.4 Rheological Measurements ($\lesssim 4\%$ strain)

Measurements were done using an advanced version of the home-developed Micro-Extension Rheometer (MER) which is an optical fiber based force device (Thesis Seshagiri Rao [144] (see schematic Figs. 5.11 and 5.7(F)). For measurements, cylindrical optical fiber glass cantilevers (125 µm in diameter and lengths of 2.5 mm or 5 mm) were made by cutting a single mode optical fiber (P1-630A-FC, Thorlabs Inc., United States) with a scalpel. The base of the cantilever was attached to a linear piezoelectric drive (P-841.60, Physik Instruments GmbH, Germany) which has a position accuracy of 1 nm and a travel range of 94 $\mu$m. The piezo was mounted on an inverted microscope (Zeiss Observer.D1, Carl Zeiss GmbH, Germany) using a motorized XYZ stage (XenoWorks, Sutter Instruments, USA)

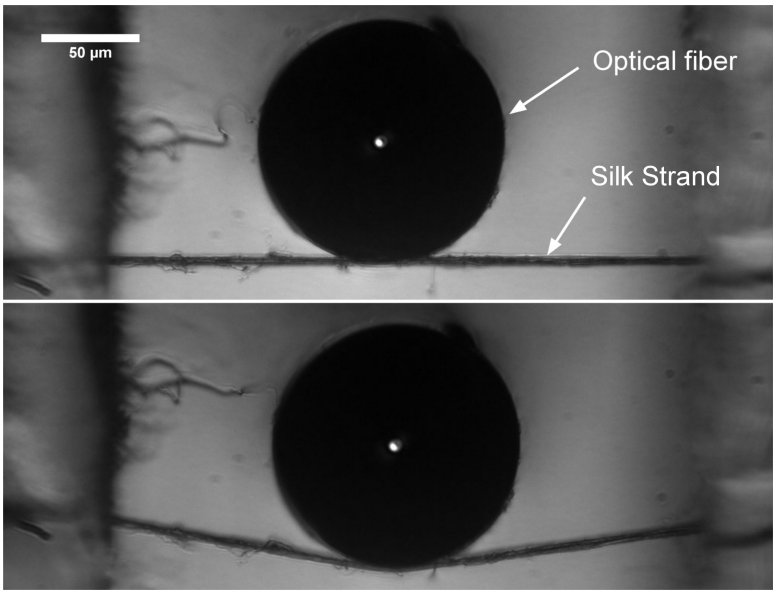


FIGURE 5.9: A typical image of a silk strand that is attached to the optical fiber to pull in a transverse direction. Images of silk strand before pulled (top) and after pulled (bottom).The bright spot is light exiting through the core of the optical fiber, which is detected on Position Sensitive Detector (PSD).

. Laser light (HeNe 632.8 nm) exiting the tip of the cantilever was focussed on to a Position Sensitive Detector (PSD) (S2044, Hamamatsu Photonics, Japan) mounted on a side of imaging port of the microscope. The cantilever deflection was calculated as the difference between the applied piezo displacement and the measured cantilever tip displacement with a final resolution of 35 nm and 70 nm for 40× and 20× objectives, respectively. The piezo and the detector were interfaced via a PC to enable automation and operation in constant strain mode using a feedback loop implemented using a home developed LabVIEW code. The green microscope illumination light and the laser light were separated using appropriate filters to enable simultaneous force measurements and imaging using a CCD camera (Andor Luca R604, Andor Technology, Ireland). A photograph of the setup is shown in Fig. 5.8. The silk fiber glued between the two parallel coverslips (Fig. 5.7(E)) was placed on the microscope stage and was displaced in the transverse direction using the tip of the optical fiber placed at the mid-point of the silk strand Figs. 5.9 and 5.7(F). The desired strain was calculated from the geometry as $\gamma = (\sqrt{L_i^2 + 4d^2} - L_i)/L_i$. The deflection of the cantilever is calculated as $\delta = D - d$, where $D$ is the piezo displacement, and $d$ is the displacement of the tip of the cantilever obtained from the PSD output. The force on the cantilever

is then given by $F = -k\delta$, where $k$ is the cantilever force constant. The force constant is obtained by placing the cantilever in a horizontal position and loading it with small pieces of thin copper wires of known weight.

### 5.5.5 Large strain experiments ($\gtrsim 4\%$ strain)

The maximum strain that can be applied using the piezo drive is limited by the travel range of the piezo (94 $\mu$m). To probe the mechanical response of the silk fibers at higher strains, we manually pulled the silk fibers using the motorized XYZ stage holding the piezo. The stage is controlled by a Joystick with selectable speeds. After manual pulling, we waited for a reasonable wait time to let stress relax on the fiber. After the completion of stress relaxation, the displacement of the optical fiber was calculated from the camera images. Then step-strain along with sinusoidal oscillations were applied to measure the viscoelastic response at that value of pre-strain. Successive manual displacements are applied in this manner to obtain different strain levels. With this method, we were able to probe the viscoelastic response up to 30% strain.

### 5.5.6 Microscope imaging

The silk fibers mounted on the microscope were imaged using 20× and 4× objective to measure its length, and a 40× objectives to measure its diameter. A small displacement was applied to ensure that the ends are not moving. The pixel size of the final CCD images was calibrated using an Olympus Objective Micrometer scale. The fibers were also imaged during experiments. Recovery of strain was also tested by releasing a few fibers from their maximally strained state. Most of the fibers recovered from their strained state ($< 10\%$) to the initial state in a few hours.

### 5.5.7 Electron microscopy Images

Silks are extremely thin fibers having 1-2 $\mu$m in radii, challenging to see by the naked eye. But these fibers can be seen using high resolution microscopy such as

scanning electron microscopy (SEM) or transmission electron microscopy (TEM). Here, scanning electron microscopy images (SEM) were taken using Carl Zeiss Ultraplus-FESEM (EHT = 3-5 kV). Silk fibres were glued on ITO glass and then sputter-coated with platinum (coating thickness  2 nm). Diameters for the silk strands were measured using Smart SEM software for EM images. Typical EM images of dragline and cribellate silk are shown in Fig. 5.10. As discussed earlier, dragline silk is made of many small parallel fibers. Whereas, cribellate silk which is sticky in nature which helps preys to stick with the web and is made of ultra-thin fibrous structure. It is also found that cribellate silk has a central fiber, almost like dragline silk. We speculate that these central fibers mainly contribute to the mechanical response of cribellate silk. Force measurement on cribellate silk is extremely difficult due to the sticky nature of cribellate fibers.

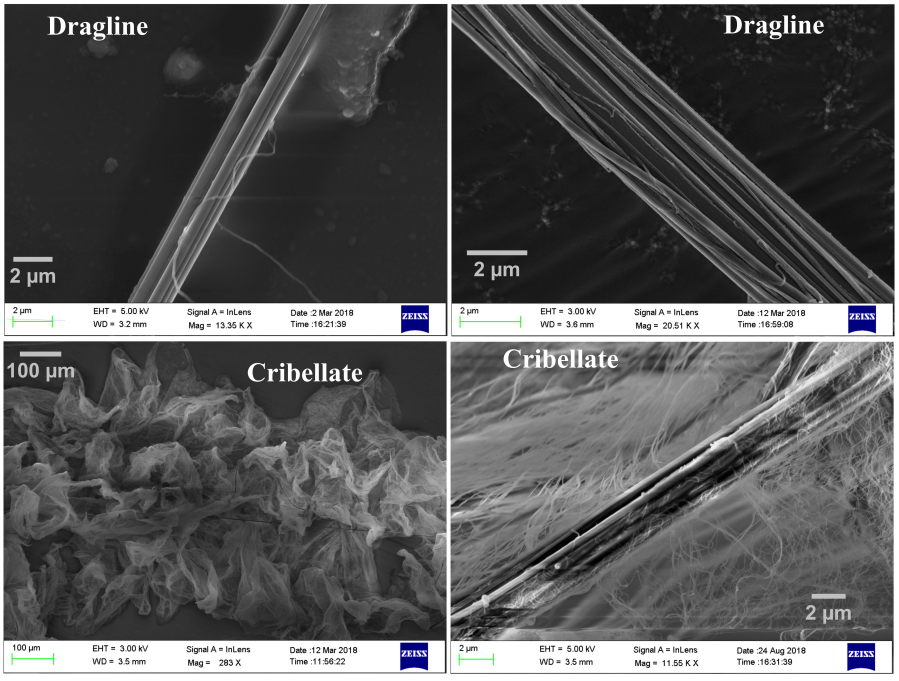


FIGURE 5.10: Electron Microscopy images of dragline and cribellate silk: Dragline is made of many thin fibers, whereas cribellate is consist of a central fiber that surrounded by ultra-thin fibers which are sticky in nature.

## 5.6 Viscoelastic response at small strain regime

First, we probed the mechanical properties of dragline silk fibers in small strain regime. The mechanical properties of the silk strands were probed by displacing the silk strands in the transverse direction using the optical fiber, as shown in Fig. 5.11(A), Fig. 5.7(F) and described in Materials and Methods section. To obtain the viscoelastic responses of silk at different strain values, we applied successive strains steps and recorded the force relaxation response, as shown in Fig. 5.11(B). Once the relaxation is close to the steady-state value, small sinusoidal strain oscillations of fixed strain amplitude and frequencies (0.1 and 1 Hz) were superposed on to the pre-strain. The force relaxation shows the viscoelastic nature of dragline silk. It also shows that silk behaves as solid-like at long times as indicated by the average steady-state force (Fig. 5.11(B)). From force relaxation data, the tension along the fiber is calculated as $T(t) = F(t)/(2\sin\theta)$, where $\sin\theta = \dfrac{d}{\sqrt{d^2 + (L_i/2)^2}}$, $\theta$ is the angle with respect to the initial position, $d$ is the displacement of the tip of the cantilever which is in contact with the silk midpoint, and $L_i$ is the initial length of the silk strand (see Fig. 5.11(A)).

Using $T(t)$ thus obtained, we calculate the elastic moduli for different pre-strain values using the small amplitude oscillations as follows. Corresponding to the imposed strain oscillations $\gamma(t) = \gamma_0 \sin(\omega t)$, we obtain stress oscillation as $\sigma(t) = \sigma_0 \sin(\omega t + \phi)$, where $\sigma(t) = T(t)/A$, $A$ being the cross-sectional area of the fiber. The storage moduli for different strains are then obtained as $E'(\gamma) = \dfrac{\sigma_0}{\gamma_0}\cos(\phi)$, and the viscous moduli as $E''(\gamma) = \dfrac{\sigma_0}{\gamma_0}\sin(\phi)$. The storage moduli exhibit a strain-softening behavior, as shown in Fig. 5.11(C) with a minimum at around 4% strain. The loss moduli could not be determined as the phase lag between the applied strain oscillations and the stress response was below the detectable range of the setup. The tension relaxation curves obtained from the application of sequential step-strains could be fitted well to a double exponential function $T(t) = a\,\exp(-t/\tau_1) + b\,\exp(-t/\tau_2) + c$, where $\tau_1$ and $\tau_2$ are the two relaxation times (see Fig. 5.11(D)). These relaxation times increase with the applied strain, as shown in the inset of Fig. 5.11(D).

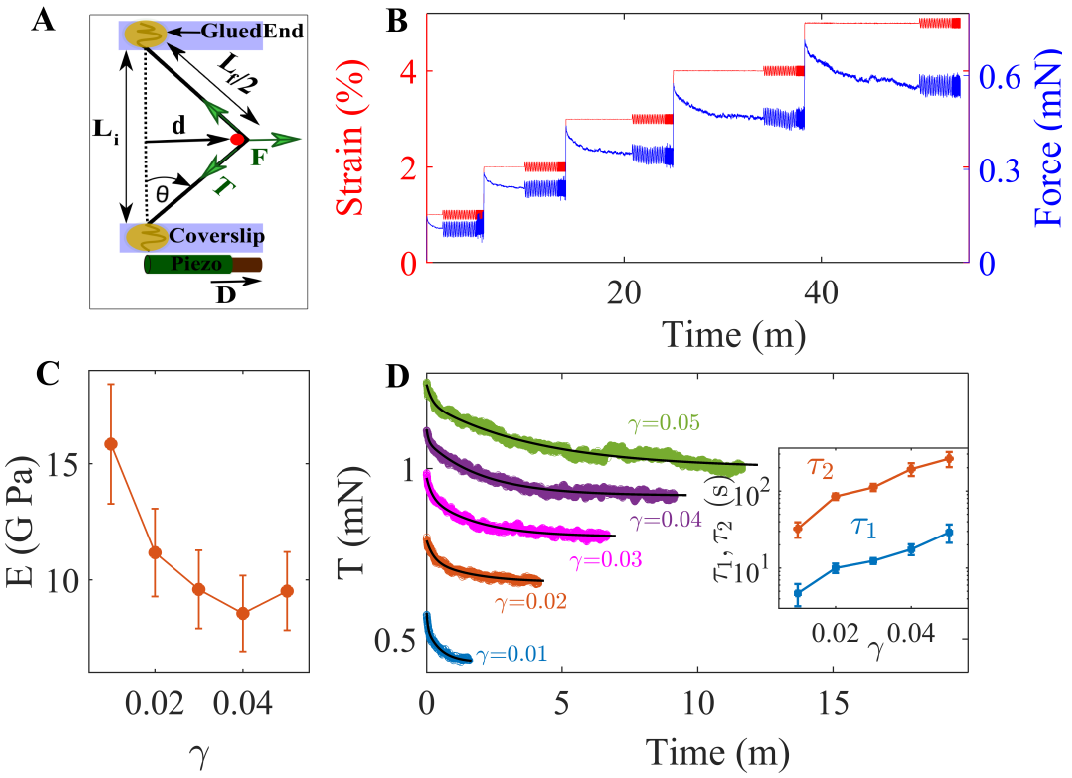


FIGURE 5.11: **Force measurement at small strain** (A) Schematic of a silk strand pulled using the optical fiber in the transverse direction. (B) Typical force response of dragline silk subjected to sequential strain steps with a wait time between steps. The force relaxes to a steady-state value after each step, and this steady-state force increases with strain showing that silk behaves as a viscoelastic solid. Small amplitude sinusoidal oscillations have been superposed towards the end of the relaxation process to obtain the viscoelastic moduli for each pre-strain. We first applied 20 cycles at 0.1 Hz, followed by 50 cycles of 1 Hz. (C) Storage moduli calculated using the sinusoidal oscillations (0.1 Hz) exhibit a strain-softening behavior. The data points are averages of nine strands, and the error bars are standard error of the mean (SE). (D) The tension relaxation curves obtained for each step is fitted to a double exponential to extract the relaxation times $\tau_1$ and $\tau_2$. The black curves are the fits. A log-linear plot of the variation of these relaxation times as a function of strain is shown in the inset (averages for n = 10 strands).

### 5.6.1 Pre-tension on silk strands

The silk strands are in pre-tension while it is on the web. We preserve the pre-tension of the silk strand while transferring it to the coverslip. This pre-tension is calculated by extrapolating the steady-state tension vs. strain to zero strain. We fit the steady-state tension vs. strain data to a quadratic function $-ax^2 + bx + c$. The figure shows fits for many silk strands 5.12(A). The pre-tension varies from 0–9mN range, as shown in figure 5.12(B). SE is standard deviation from the mean.

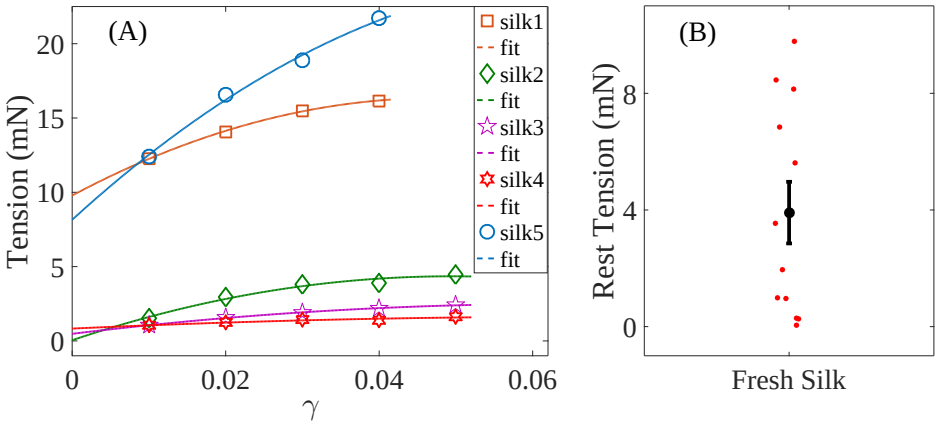


FIGURE 5.12: **Pre-tension** The silk strands are under pre-stress (Pre-tension) on the web. (A) Rest Tension is obtained by extrapolating the steady-state tension vs. strain to zero strain by fitting the data with equation $-ax^2 + bx + c$ for different silk strands. (B) Pre-tension for different silk strands (SE standard deviation from the mean).

The frequency range we could probe using the current version of the Micro-Extension Rheometer was limited by the time constant of the feedback loop that maintains a prescribed strain during the experiments. A similar attempt has been made by Blackledge *et al.* [145], where they applied a single frequency of 20 Hz and measured the loss moduli from the phase lag between the applied strain and the resulting stress response. The loss moduli measured is found to be one order of magnitude less than the storage moduli. In order to obtain the frequency response over a much wider range of frequencies, we performed the following analysis.

## 5.7 Frequency dependence of moduli

The frequency range (max. 1Hz), we could probe using the current version of the Micro-Extension Rheometer was limited by the time constant of the feedback loop that maintains a prescribed strain during the experiments. However, the frequency information is contained in the tension relaxation data, and this can be retrieved as discussed below.

Mechanical responses of viscoelastic materials are generally characterized by applying a sinusoidal stress or strain perturbation. The main advantage of such oscillatory measurement is that the steady-state response can be characterized

independently as a function of the amplitude and frequency of the applied perturbations. To overcome the frequency limitation of our experimental setup, we analyze the tension response to step-strain as follows. For a viscoelastic material, the linear response under an applied step-strain ($\gamma$) can be expressed in the time domain by stress relaxation modulus $E(t) = \frac{\sigma(t)}{\gamma}$, where $\sigma(t)$ is the time dependent stress in the system. Equivalently, such response can also be expressed in the frequency domain by a complex dynamic modulus $E^*(\omega) = E'(\omega) + iE''(\omega)$. Here, $E'$ is the storage modulus that quantifies the elastic response and $E''$, the loss modulus quantifies the viscous response of the material. In our experiments, we apply a strain deformation and measure the stress as a function of time. However, we observe that even for small strain amplitudes ($\sim 1\%$), the accessible frequency range is below $\sim 1$ Hz for the MER setup. In principle, the frequency dependent moduli can be obtained from time domain measurements, since $E(t)$ and $E^*(\omega)$ are related via simple Fourier transforms. However, in practice, reliable interconversion between $E(t)$ and $E^*(\omega)$ becomes nontrivial due to the noise present in the experimental data. A recent paper [146] describes a simple and direct method to obtain frequency dependent moduli from time domain data that is not prone to the artefact due to noise. By using this method, $E^*(\omega)$ can be calculated from time dependent creep compliance $J(t) = \frac{\gamma(t)}{\sigma}$ obtained from step stress experiments. Since, our experiments are strain controlled, direct measurement of $J(t)$ is not possible. Although, $E(t)$ and $J(t)$ are just reciprocal of each other dimensionally, they are mathematically related by a convolution integral [147]:

$$\int_0^t d\tau\, E(t-\tau)J(\tau) = t, \;\; (t > 0). \tag{5.1}$$

If $E(t)$ or $J(t)$ varies smoothly and the variation is slow enough such that the magnitude of the local logarithmic slope, $n = \left|\frac{\partial\, log[\xi(t)]}{\partial\, log[t]}\right|$, where, $\xi(t)$ is either $E(t)$ or $J(t)$ remains small ($n \ll 1$), then $J(t)E(t) \approx 1$ holds. The underlying theory is well summarized in a recent paper [148]. We show the variation of $n$ as a function of time in Fig. 5.14. We find that for all values of strain the maximum value of $n$, as estimated from the steepest portion of the curves, is $\ll 1$. Thus, we can directly estimate $J(t)$ using the relation: $J(t)E(t) \approx 1$. We show the variation of $E'$ and $E''$ of a dragline silk fiber as function of $\omega$ obtained by this method for different step

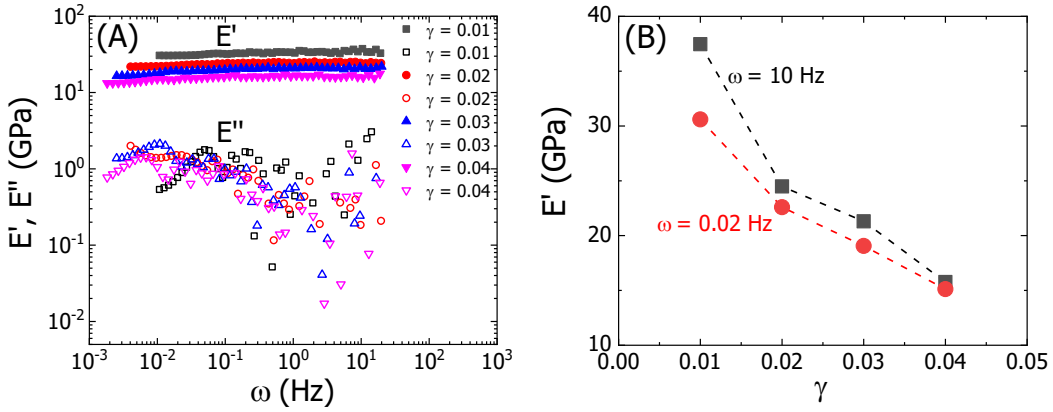


FIGURE 5.13: **Frequency dependence moduli** (A) Elastic moduli $E'$ (solid symbols) and viscous moduli $E''$ (hollow symbols) are plotted as a function of frequency for a dragline silk fiber for different step strain magnitude ($\gamma$ : 1 - 4 %) indicated in the figure legend. (B) Variation of $E'$ with $\gamma$ for two different frequencies as indicated in the figure.

strain magnitudes in Fig. 5.13. We find that over almost 4 orders of magnitude variation in $\omega$, the fiber remains highly elastic with ($E' \gg E''$). The magnitude of the elastic moduli compares well with the steady shear measurements presented in Fig. 5.11(C). Also, the flatness of $E'$ over wide frequency variation indicates the silk fiber is a viscoelastic solid over the observed frequency range. The gradual drop in $E'$ with increasing magnitude of applied step strains is consistent with the softening seen with increasing steady state pre-strains (Fig. 5.11(B)). Such drop in $E'$ as a function of strain is shown for two values of frequency in 5.13(B).

## 5.8 Viscoelastic response at large strain regime

To overcome the limited travel range of the piezoelectric drive, which limits the strain range, we performed experiments by stretching silk fibers using the motorized XYZ stage on to which the piezo was mounted. Then applied a step-strains along with the superimposed strain oscillations using the piezo (see Material and Methods for details). By applying small perturbations is of an advantage as without knowing the history of pre-stress, one can calculate the modulus at that pre-strain, by these small oscillations. The calculations to obtain the storage and loss moduli is described in the Materials and Methods section. We employ a similar strategy here. The storage moduli obtained as in the case of small strain regime shows a clear minimum at around 4–5% strain when plotted as a function of

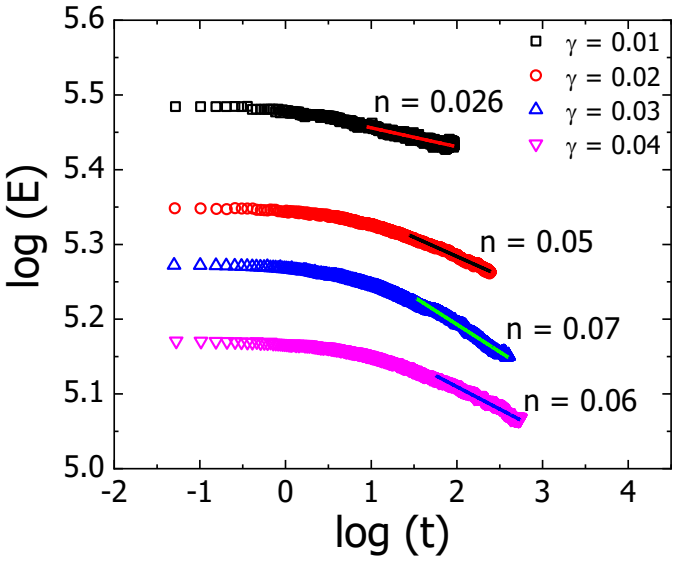


FIGURE 5.14: Variation of stress relaxation modulus $E(t)$ as a function of time. For convenience, the logarithm of the quantities is shown. The values of the logarithmic slope $n$ are indicated in the figure.

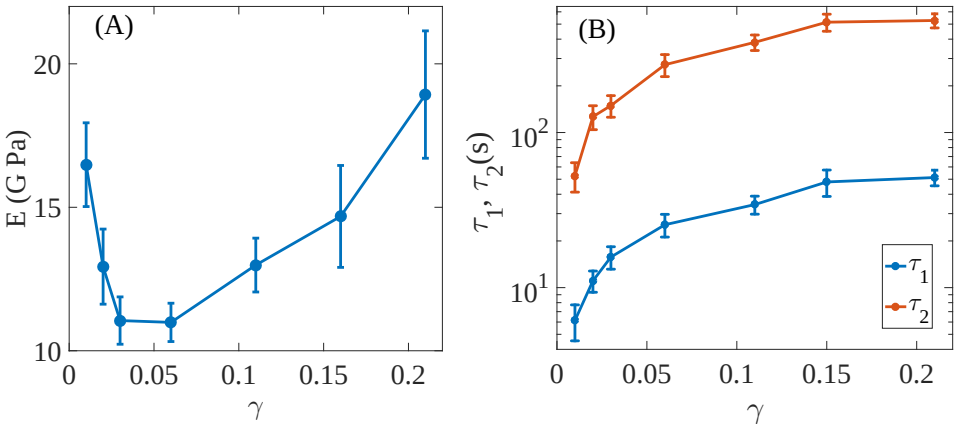


FIGURE 5.15: **Elastic moduli at higher strain** (A) Averaged elastic moduli obtained from large-strain experiments (n=10) show an initial strain-softening followed by strain-stiffening. (B) Log-linear plots of the two relaxation times $\tau_1$ and $\tau_2$ show that they increase with applied strain and tend to saturate towards the higher values of strain (n=7). Error bars are SE.

pre-strain (Fig. 5.15(A)). After initial strain-softening, the elastic moduli shows strain-stiffening response above 5% strain, which is reported for many species by others as well [6]. The relaxation curves were fitted with a double exponential function ($T(t) = a\,\exp(-t/\tau_1) + b\,\exp(-t/\tau_2) + c$, where $\tau_1$ and $\tau_2$ are the two relaxation times). Thus obtained relaxation times and its variation are shown in Fig. 5.15(B). Both $\tau_1$ and $\tau_2$ increases with strain and tend to saturate towards higher pre-strain values. The normalised elastic moduli are shown in Fig. 5.16.

The maximum strain in these experiments was limited to about 30% and we could observe signatures of partial breakage in some cases. Also, most of the strands failed to fully recover their initial length after a stretch of about 30%.

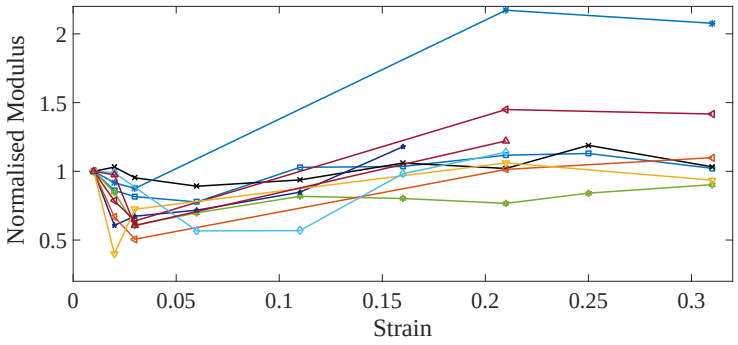


FIGURE 5.16: **Normalised Elastic modulus at higher strain** Elastic modulus (individual curves) normalized with respect to its initial value shows that there is initial softening which is followed by strain stiffening which is in good agreement with the small strain data.

## 5.9 Energy dissipation

The energy dissipated during cyclic deformations is proportional to the area enclosed by the stress vs. strain plot. To probe the energy dissipated during the deformation of the silk strand has any strain dependence, we applied cyclic ramps (triangular perturbation instead of sinusoidal), as shown in Fig. 5.17(A). The application of the triangular perturbation causes an increase in the average pre-strain value. This leads to a relaxation of the average stress, which finally reaches a steady-state Fig. 5.18. Corresponding to this, the enclosed area for each cycle evolves until it too reaches a steady-state (at limit cycle), as shown in Fig. 5.17(B). These limit cycles are used to study the dependence of dissipated energy on frequency or strain. It is also found that enclosed area at various pre-strains too saturates towards higher strains, which indicates that energy dissipation is more at low strain and becomes almost constant at higher strain, as shown in Fig. 5.17(B). In Fig. 5.17(C), we show that the Lissajous figures obtained from a few limit cycles for a ramp frequency of 0.05 Hz and an amplitude of 2% and for different amounts of average pre-strain. The increase in the values of peak stress with increasing average pre-strain value, as shown in Fig. 5.17(C) is due strain-stiffening of the

silk fiber, as discussed earlier. The strain stiffening is concluded from the slope of the enclosed loop. The slope of the enclosed loop is increasing at various applied average pre-strain, which clearly shows a strain-stiffening response. To probe the frequency dependence of the energy dissipation, we applied triangular waves of different frequencies. We found that the energy dissipation is independent of applied frequency in the range 0.01–1 Hz (Fig. 5.17(D)).

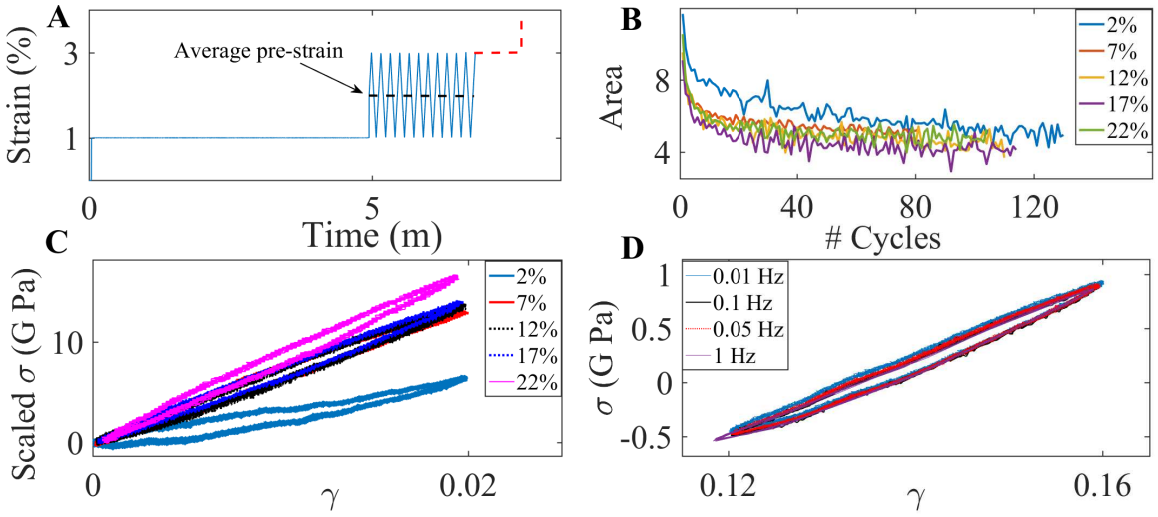


FIGURE 5.17: **Ramp experiment**(A) A schematic of the pre-strain plus cyclic ramp protocol used to obtain stress–strain Lissajous figures in order to estimate the dissipated energy. (B) The evolution of the enclosed area within each cycle with cycle number shows the trend towards a limit cycle. (C) Lissajous figures obtained from limit cycles corresponding to various amounts of pre-strain. The pre-strain in each case is indicated in the figure, and the strain amplitude is 2% for all the cases. The data were rescaled by subtracting the lowest values of strain and stress ($\gamma(t) - \gamma_{\min}$, $\sigma(t) - \sigma_{\min}$) for representation. (D) Experiments performed at different frequencies for a fixed pre-strain (strain amplitude 4% ) show no significant change in the enclosed area of the limit cycle, within the frequency range allowed by the MER technique.

We did an experiment where we first applied a step-strain followed by triangular waves, and after it reaches limit cycles, we stopped the triangular wave, which is called a gap and then waited for some time and again applied triangular waves. A similar experiment, as described earlier in this section but with gap in between the triangular waves as shown in Fig. 5.18 (inset). Peak tension calculated from the force data plotted in Fig. 5.18 clearly shows saturation after the limit cycle, as well as no significant change after the limit cycle is reached even after the gap.

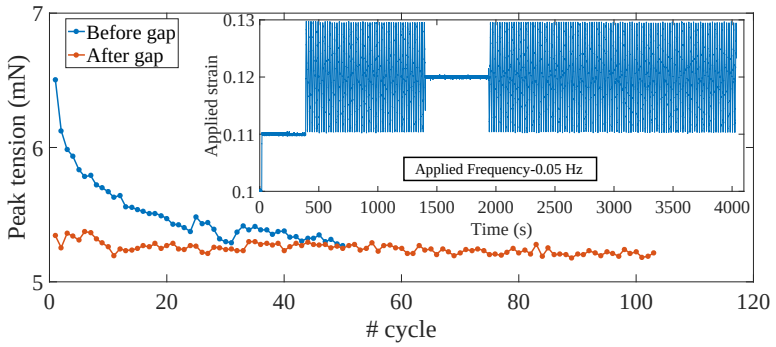


FIGURE 5.18: **Peak tension** Peak tension plotted for the applied triangular wave before and after the gap shows that no change in tension after saturation, which implies dissipation is constant.

## 5.10 Ageing of silk

Silk is expected to age due to effects like loss of water, degradation of the proteins, structural relaxation, etc. It has been reported that various properties (structural and material) such as stiffness, extensibility, and diameter of the strand change due to ageing [138, 139, 149]. In synthetic fibers, the major challenge is to maximize mechanical properties as well to maintain it over time. In contrast, most applications for bio-mimetic silk analogues depend upon long-term durability of mechanical performance. Thus, it is important to understand the change in the mechanical performance of spider silk while aged. One of the main functions of the web is to absorb the kinetic energy of flying insect prey. Then, it also becomes important to understand how this web will be effective in catching prey after a certain period of ageing [138, 139, 149].

In order to check whether the observed non-linear responses of silk are altered with age or not, we compared data obtained from the same fibers about a day after spinning ("fresh") and 10–12 months later ("aged"). The samples were stored in the lab as detailed in Material & Methods. As can be seen from Fig. 5.19(A), the strain-softening behavior is retained in aged silk, albeit with higher values of the storage moduli. This is in good agreement with data reported earlier in dragline silk from different species after one year of ageing [139]. The two relaxation times show the same trend with strain as fresh samples, but the values, for a given strain, decrease with age (Fig. 5.19(B)), consistent with the increase in storage moduli.

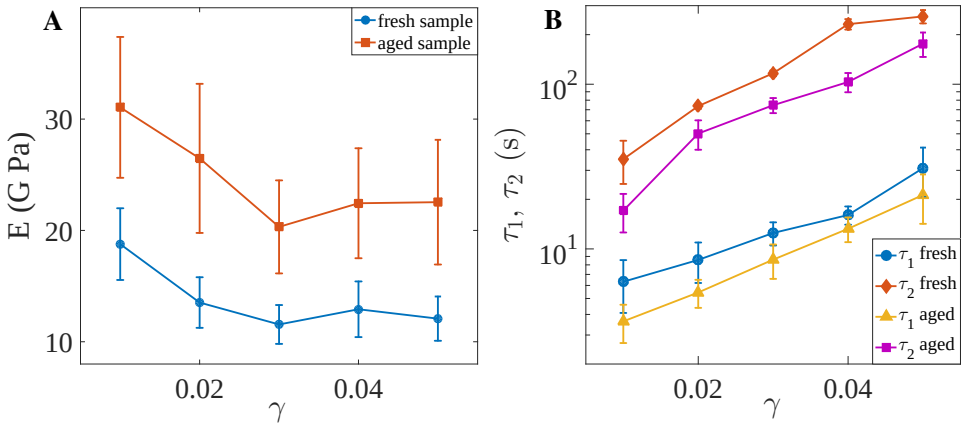


FIGURE 5.19: **Ageing of silk** (A) Change in elastic moduli as a function of strain measured for fresh and aged silk strands. The same strand was measured a day after extraction (fresh) and then 10–12 months later (aged). The error bars are SE (n=10). (B) The relaxation times obtained from fresh and aged silk fibers show a similar increase with strain, but for a given pre-strain, the relaxations become faster with age (n = 7).

The ageing behavior can be of interest in particular to social spiders as they show little tendency to abandon a web unless forced to by external agents (heavy wind or rain) since silk is expensive to produce. On the other hand, many solitary spiders will eat up their silk and go to another site [118, 150]. The increase in elastic moduli can be explained by hypothesizing the orientation and cross-linking of proteins might increase over the long term [139].

## 5.11 Extension rheology of cribellate silk

As described earlier, capture silk has two silk types–viscid silk and cribellate silk. Cribellate spiders have an additional organ call cribellum, which is located in the front of the spinnerets [5]. The cribellar area has many densely packed tiny spigots that produce extremely thin silk threads (∼10 nm), which can also be seen in our electron microscopy images (Fig. 5.10). Cribellate threads contain an axial fiber which is covered with a dense mesh of cribellate silk fibrils. These fibrils are sticky in nature and help spider to catch their prey [5, 116, 124].

Here, we have done force measurements on cribellate silk using similar protocols as dragline silk. It is hard to perform mechanical measurements on cribellate silk

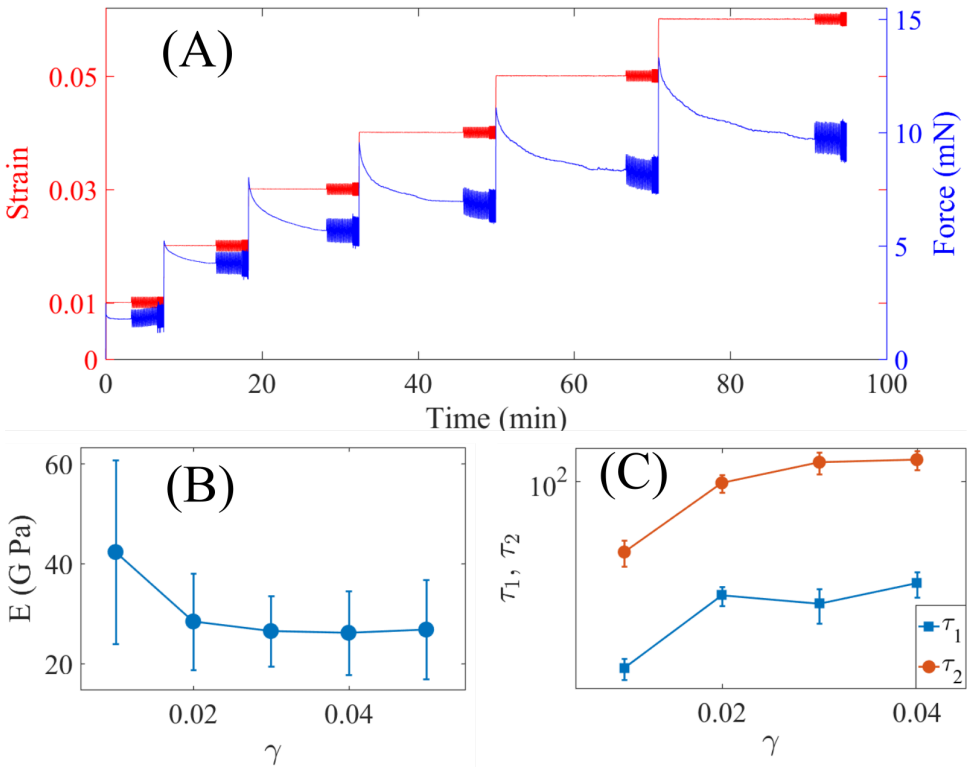


FIGURE 5.20: **Mechanical responses of cribellate silk** (A) Typical force response of a cribellate silk strand on imposed strain probed using successive step-strain along with oscillations. (B) Elastic modulus calculated by using the small sinusoidal perturbations, which shows a faint strain-softening. (C) The relaxation times obtained by fitting the tension relaxation data show similar behavior as dragline silk, which increases with imposed stain (n = 4).

due to its sticky nature. This makes it difficult to extract from the web as well as while transferring the strand to the coverslip.

Fig. 5.20 (A) shows typical force response data from cribellate silk. The force response looks similar to dragline silk behavior. The elastic modulus is obtained from small sinusoidal oscillation described a similar method earlier in the case of the dragline. The relaxation times increase with the applied strain, as shown in Fig. 5.20(C).

Cribellate silk shows similar behavior as a dragline, which could be due to the thick central fibers seen in cribellate silk images (Fig. 5.10). We could not do the measurement on many silk fibers due to its sticky nature. That is why we lack with sample size.

## 5.12 Models explaining spider silk mechanical response

Various models have been proposed to investigate spider silk mechanical properties from elastic models to the bottom-up approach (simulations based models). There are several attempts to explain the force-extension behavior of dragline silk as well as capture silk, including loading, unloading, and reloading of the silk [6]. It is important to understand the silk nanostructure to come up with an exact mechanism to explain various silk mechanical properties. Several techniques have been used to investigate silk nanostructure. Based on these observations, people have come up with several models. Dragline silk proteins Spidroin I and Spidroin II consist of alanine-rich anti-parallel beta-sheets organized as nano-crystallites, which are a few nanometers in size, and glycine-rich amorphous regions which are connected together via hydrogen bonds [128, 135]. Single fiber X-ray diffraction studies show that the crystalline regions are oriented with the beta-sheets parallel to the fiber axis [130]. Recent NMR studies indicate that the amorphous regions are also orientationally ordered with the helical secondary structure aligned along the fiber direction [151]. The degree of order in the crystalline and amorphous regions, as well as their relative fractions, may vary between spider species, and also with humidity [6, 128, 141, 152]. Application of strain results in a reduction in the size of the crystallites, suggesting unfolding of the beta-sheets under force [130]. Although there are several studies on the microstructure of silk using Raman scattering, NMR, and X-ray, the relation between the microstructure and mechanical response is still not fully understood [130–134].

Various models have been proposed to account for the force-extension curves of dragline silk fibers. A model proposed by Termonia [153] represented the dragline silk fibril as a regular 2D lattice of nodes with different stress-strain relationships for the crystallite and amorphous regions. The assumption for this model is that the crystallite regions provide strength, and the amorphous regions provide elasticity, which is now generally accepted. By considering the breaking of hydrogen bonds within the amorphous regions as an activated process with a force dependence, it is possible to obtain the force-extension plots for wet and dry dragline

fibers, similar to those seen in experiments. The polymer chains devoid of hydrogen bonds are modelled as a non-linear elastomer, and the nano-crystals are assumed to be rigid without any force-dependent structural changes. Such a model qualitatively reproduces the experimentally observed responses of dry silk and hydrated silk, where hydrogen bonds are assumed to be in a dissociated state. In the case of dry silk, one observes the characteristic kink in the force-extension curve, which is absent in the case of hydrated silk fibers. This model also predicts that increasing crystalline size will decrease the tensile strength. Even though this model is not structurally correct (silk is not 2D lattice) but it reproduces several characteristics of the stress-strain curve.

Tommasi et al., [16] developed a model where the silk fiber is considered to be a composite material consisting of crystalline and amorphous regions, as described by earlier models. The model having 1-D elasticity and based on loading, unloading, and reloading of the silk fiber. They assume that the material is composed of a soft fraction with entropic elasticity and a hard, damageable fraction. The hard fraction models the presence of stiffer, crystal-rich, oriented regions and accounts for the effect of softening induced by the breaking of hydrogen bonds. To describe the observed presence of crystals with different size, composition, and orientation, this hard fraction is modelled as a distribution of materials with variable properties. The soft fraction describes the remaining regions of amorphous material and is here modelled as a worm-like chain. The stiff crystalline regions are assumed to be a linear elastic material which can undergo a transition to amorphous beyond a threshold strain. This is motivated by AFM experiments on single silk proteins, which show the force-induced unfolding of domains [154]. The amorphous regions are treated as Worm-Like-Chain (WLC) entropic springs with a characteristic non-linear strain-stiffening response. By changing the relative amounts of these two regions, pure stiffening (high amorphous content) or softening followed by stiffening (intermediate amorphous content) responses can be obtained. The initial softening is due to the unfolding events which dominate at small strains, above a force threshold, and the subsequent stiffening may be attributed to the non-linearity of the WLC elasticity. The success of this elastic model is based on

the strain-induced conversion of the crystallites into amorphous structures. Although, this is not entirely correct because the elastic behavior stems from a loss of hydrogen bonding in the amorphous phase, and crystallites unfold only near the fracture.

Another model by Nova *et al.*[155], where the features of the force-extension curves can be replicated using a series arrangement of 1-D non-linear springs representing the amorphous and crystalline regions. More specifically, the stiffness of the amorphous regions is modelled using three regimes: a stiff regime representing the homogeneous stretching of chains, followed by a softer regime representing the breaking of secondary structure elements and, finally, a high-stiffness regime corresponding to the stretching of covalent bonds.

However, these elastic models give a simple explanation of spider silk mechanics but fail to explain with silk nanostructure response. To do that, many people have used the bottom-up approach to mimic the silk mechanical response [156, 157]. The simulations showed four regimes in the force-extension profiles, with a relative stiffness that depends on hydrogen bonding and the secondary structures. After an initial stiff regime, hydrogen bonds in the amorphous region break, leading to softening. Then, as the amorphous chains become highly extended, substantial stiffening is observed. In the fourth regime, hydrogen bonds in the crystallite region break [6, 156, 157].

While these models are able to reproduce some of the main qualitative behaviors of silk fibers, and provide some insight into the microscopic processes occurring in dragline fibers under extension, they lack the ability to predict time-dependent properties like the stress relaxation or the frequency dependence of the elastic and loss moduli presented in this article.

The experiments we report in this chapter show two prominent features. The Young's modulus exhibits an initial strain softening and subsequent stiffening with clear minima at around 4% strain, whereas the two relaxation times increase with strain and tend towards saturation. Dissociation of the hydrogen bonds within the amorphous region or unfolding of the nano-crystallites alone cannot account for

either a strain-dependent relaxation time or dual relaxation times. In such cases, one expects a single relaxation time given by the characteristic rate of unbinding.

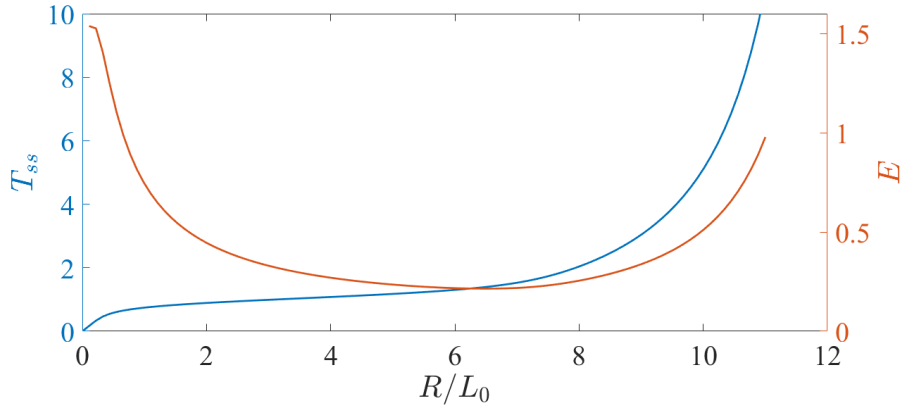


FIGURE 5.21: **Tension and modulus response of protein unfolding-refolding model** Equilibrium tension and Young's modulus versus extension curves for a structure containing spectrin molecules with domains that can unfold and refold in a force-dependent manner. The Young's modulus shows strain-softening followed by stiffening response. The stiffening occurs when most of the domains are in the unfolded state, and the molecules behave as a WLC. $T_{ss}$ is the steady-state tension, $E$ is the Young's modulus, $R$ is the spectrin end to end distance, and $L_0$ is contour length. (REF: Dubey *et al.* [12]).

A model where protein domains can reversibly unfold and refold has been developed recently to account for strain softening in axons of neuronal cells [12]. Such a model incorporates two molecular level timescales–one for the unfolding process and one for refolding. This model generates an initial strain softening and a subsequent stiffening (see Fig. 5.21)–the former is due to stress relaxation from domain unfolding and the latter due to the non-linear stiffening of the polymer, which is treated as a WLC. Although this model can account for the relaxation process, it predicts a peak in the relaxation time vs. strain plot, which we do not observe in our silk data.

We may speculate that a possible resolution to this may be to include both the molecular processes considered by Termonia [153] and Tommasi *et al.* [16]. In such a case, the softer bonds (presumably the hydrogen bonds in the amorphous region) dissociate at small strains leading to a softening (see Fig. 5.22) [153]. The force relaxation arises from the dissipation of stored elastic energy when bonds dissociate. As strain increases, the amorphous region loses most bonds, and the

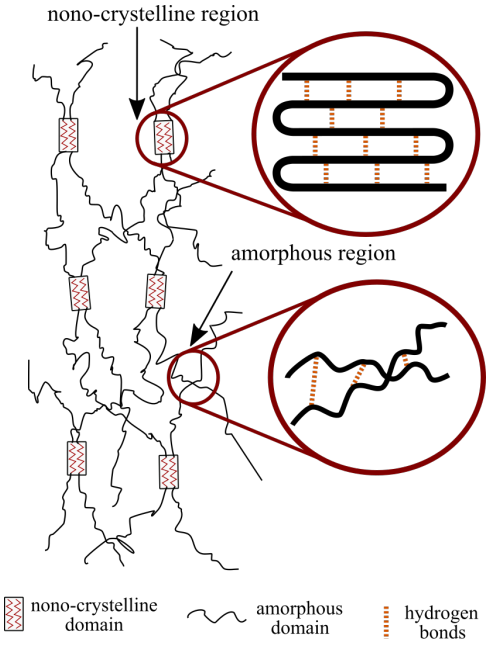


FIGURE 5.22: **Ultrastructure of silk** A schematic of the ultrastructure of dragline silk showing the two types of domains–namely, nano-crystalline and amorphous regions as indicated in the figure. The red dotted lines represent hydrogen bonds.

polymer chains begin to behave more like a WLC, which stiffens with strain. However, the unfolding of the nano-crystallites, which require a higher force [16, 153], take over, and the relaxation process is now dominated by nano-crystal unfolding. As the amorphous region is well into the stiffening regime, the unfolding of nano-crystallites alone may not be sufficient to cause softening. Moreover, the two relaxation times may have their origins in these two dissociation processes (hydrogen bond dissociation and nano-crystal unfolding), which are expected to have different characteristic rates. These speculations need to be tested by further quantitative models.

## 5.13 Conclusion and summary

The results presented in this chapter are summarised as follows. We have probed the elastic response of social spider dragline silk fibers by applying a sequential step-strain plus small amplitude sinusoidal oscillation protocol. We show that silk fibers exhibit strain-softening at low strain (below 4%), followed by strain stiffening at higher strains (Fig. 5.15). The relaxation times obtained from tension

relaxation curves show monotonic behavior with the applied strain (Fig. 5.11). It will be interesting to investigate the origin of these relaxation times.

By Fourier decomposition of the stress relaxation subsequent to each step-strain, we extracted the frequency response of the storage and loss moduli for different values of pre-strain. With this method, we are able to record the variation of moduli as a function of frequency and show that a weak dependence of the frequency (0.001–20 Hz) on the moduli (Fig. 5.13).

The ageing behavior we show here is in good agreement with previous studies and could help in unravelling of spider silk mechanical properties. The increase in elastic moduli can be explained by hypothesizing the orientation and cross-linking of proteins might increase over the long term (Fig. 5.19) [139]. It has been reported that various properties (structural and material) such as stiffness, extensibility, and diameter of the strand changes due to ageing [138, 139, 149]. Thus, a major challenge is to make a synthetic bio-polymer of longer durability while preserving its mechanical properties.

We expect that these novel results will help to understand the nanostructure of the dragline silk fibers having these unique properties. The relaxation time behavior could help to understand the dissipative mechanisms happening inside the silk. This study should motivate for a model to include kinetics of domain unfolding-refolding or unbinding-rebinding to explain unique mechanical features of spider dragline silk.

# Chapter 6

# Conclusions and Remarks

## 6.1 An overview of axon and silk mechanical responses

Strain softening is observed in many materials including, biological cells. In materials like concrete, rocks, and metals, the softening response arises due to dislocations, defects, or damage [158]. Mechanical properties of polymer networks (F-actin) are influenced by cross-link rupture, and force-induced unbinding is shown to be the dominant mechanism in strain-softening [159]. Networks that are weakly connected—pure F-actin solutions, weakly cross-linked actin networks, and pure microtubule networks, show softening behavior [35]. But strain-softening seen in these systems has no memory of their initial states. So under large stretch deformations, these mechanisms will fail to recover the initial zero strain condition or to preserve shape or length of the biological systems like cells or silk.

The two materials—axons and silk, studied in this thesis have highly anisotropic shape and nanostructure. These two materials occur in nature as micron thin and extremely long strands and are constantly subjected to stretch deformations. In the case of axons, due to limb movement or shear deformation of the brain, and in the case of silk, due to impacts of insects or movement of branches. Axons have anisotropic internal structure because of various aligned filaments and the 1-D periodic actin-spectrin lattice inside, whereas silk nanostructure has anisotropic arrangements of amorphous and crystalline domains. Both of these materials show

an initial strain softening response. According to our model presented in Chapter-4, in axons, the strain-softening response is observed due to reversible unfolding of spectrin repeated units. Our measurements on silk presented in Chapter-5 shows an initial strain-softening followed by a stiffening response. Strain-softening is observed due to either unfolding of nano-crystals or dissociation of hydrogen bonds. At higher strains, the amorphous region loses most of the hydrogen bonds, and the polymer chains begin to behave more like a Worm-like Chain (WLC), which gives rise to the strain stiffening response [16, 156]. The axon model of force-dependent folding-refolding too predicts strain stiffening response at higher strains. But, we could not probe in the high strain regime due to practical limitations.

From the above proposed mechanisms, it seems that nature has employed a similar mechanism to protect these materials from large stretch deformations–unfolding of spectrin units in the case of axons and unfolding of nano-crystals or dissociation of hydrogen bonds in the case of silk. These materials protect themselves due to their ability to buffer tension under large stretch deformation. However, other mechanisms such as reversible unbinding do not provide the memory of initial states and hence lack the ability to protect from the mechanical stretch.

There are other proteins as well, which are reported to have significance in maintaining mechanical integrity due to unfolding events. Strain softening due to the protein unfolding mechanism of spectrin has been shown in Red Blood Cells (RBCs) [84]. Proteins with repeat domains that can reversibly unfold under tension are used in other contexts in biological systems. In muscle, titin protein which operates like a mechanical battery storing elastic energy efficiently by unfolding domains. Titin folding and myosin activation act as inextricable partners during muscle contraction [160]. Talin, a cytoskeletal protein found in focal adhesions, acts as shock absorber via force-dependent stochastic unfolding and refolding kinetics. The ability of talin to act as a force buffer may have importance for the maintenance of cell adhesion integrity [161].

## 6.2 Future directions

The thesis investigated the role of individual cytoskeletal elements using various cytoskeletal perturbing drugs. However, the interdependencies between the filaments need attention. For example, the effect of disrupting drugs such as Lat-A and Nocodazole on other filaments has been probed. The results we present in the thesis at room temperature (25°C). The room temperature suppresses the activity in the axonal cytoskeleton. Further investigation is needed to do experiments at biological temperatures (37°C) where molecular motors and other proteins will be involved actively in mechanical response. In fact, the comparison between room temperature and biological temperature could reveal several interesting phenomena that are occurring inside the axonal cytoskeleton.

We have probed the role of the actin-spectrin skeleton and found that spectrin is also a major load bearer in axons. However, the folding-refolding mechanism needs to be tested experimentally in the cell while the force is applied. Our model currently includes only the actin-spectrin skeleton for simplicity. However, a composite model is needed to mimic the axonal cytoskeleton, which should include other filaments and their interactions such as microtubules and neurofilaments.

In silk mechanics, we add an extra constraint on theoretical models to include relaxation time behavior of dragline silk. Assuming that two processes happening inside the silk ultrastructure—dissociation of hydrogen bonds and unfolding of beta-nano-crystals, one may explain the observed relaxation processes. A computational model is needed to consider softer and harder bonds kinetics, which could get insights into silk ultrastructure.

Appendix A

**Primary neuronal culture**

Material required :

- Fertilized chicken eggs 8-9 days old.
- Fine forceps and Sterile 35 mm petri plates(460035) TARSONS.
- Hank Balanced Salt solution HBSS(1X) (+ Ca/+Mg )(Life Technologies 14025-092).
- Hank Balanced Salt solution HBSS(1X) (-Ca/-Mg)(Life Technologies 14175-095).
- 0.5% Trypsin-EDTA (5X)(Life Technologies 15400-054).
- L-15 medium (Life Technologies 21083-027) thickened with 0.6 g/100 ml methyl cellulose (Colorcon, ID34516) and supplemented with 10% Fetal Bovine Serum (Life Technologies 10100-147), 2% D-glucose (Sigma G6152).
- Neuronal Growth Factor(NGF) NGF-7S (Invitrogen 13290-010).
- 0.5 mg/mL Penicillin-Streptomycin-Glutamine (PSG) (100X) (Life Technologies 10378-016).

Protocol of sensory chicken neurons (Gallus gallus)

1. 8-9 days old chick embryo's is dissected in HBSS(+Ca/Mg) using fine forceps in 35 mm petri plate.
2. Dorsal root ganglion (DRGs) were isolated from the chicken embryo's.
3. Isolated ganglion were washed twice with HBSS(-ca/Mg) and later centrifuged .
4. The supernatant was discarded and then ganglion were put in 100 $\mu$l 5X trypsin.
5. Incubate for 15 minutes.

6. Remove Trypsin and wash with HBSS(-Ca/Mg) twice.
7. Dissociate cells in 200$\mu$l HBSS (-Ca/Mg).
8. Put cells in petri plates or rings stuck with glass coverslip on bottom containing medium.
9. Supplement medium with NGF and PSG.
10. Keep the plates in incubator and allow them to grow.
11. Cells are ready for experiment after 16-20 hrs.

**Fixative preparation**

**PHEM buffer preparation:**

| Component | Mol. Wt. | Conc.in (5X)(mM) | Conc.in 1X(mM) | amont for 1L 5X stock(g) |
|---|---|---|---|---|
| Pipes | 302.4 | 300 | 60 | 90.72 |
| Hepes | 238.3 | 125 | 25 | 29.8 |
| EDTA | 380.4 | 50 | 10 | 19.02 |
| MgCl2.6H2O | 203.3 | 10 | 2 | 2.03 |

Fixative : For 5 ml of fixative contains–

- 1 ml of 16% Para formaldehyde (Electron Microscopy Sciences Catano.15710)
- 1 ml of 5x PHEM buffer
- 3 ml of Milli-Q water
- 10 $\mu$l of 25% gluteraldehyde (Electron Microscopy Sciences CataNo.16200)

Appendix B

# Revised Axon Model

## Folding-unfolding of spectrin buffers axon tension:

The axonal cytoskeleton is complex [42] and delineating the contributions of the different components is not trivial. It has been generally assumed that bundled microtubules are the main mechanical element in axons [79, 80]. However, our results demonstrate that F-actin and spectrin play a very prominent role in axonal mechanical response. Furthermore, we have shown that axons behave as strain-softening, viscoelastic materials with long time solid-like behavior, unlike the long time flowing state predicted by pure microtubule-based models that invoke cross-link detachments [79, 80]. These observations thus motivated us to consider other dissipative mechanisms, not usually encountered in cytoskeletal remodelling, to develop a coherent theoretical description of axon stretching.

Upon sudden stretching, tension in an axon first increases then relaxes to a non-zero steady-state value Fig. 3.3, indicating dissipative processes occurring at the microscopic scale. The observation of a steady state tension at long times precludes unbinding processes—such as between spectrin tetramers and actin rings, and unbinding of microtubules-associated or actin-associated crosslinkers—as repeated unbinding events would relax tension to zero. Strain softening and stress relaxation via filament turnover can also be ruled out based on our stabilization experiments summarised in Fig. 3.13. Instead, our experiments suggest that spectrin tetramers play an important role in determining axon tension. Moreover, AFM experiments show that spectrin repeats sequentially unfold under tension [111]. This suggests that dissipation of the energy stored in the folded structure of the protein might contribute to tension relaxation in the axon. However, spectrin may not be the only protein component susceptible to tension dependent unfolding/re-folding. Tau proteins, which crosslink microtubules in axons, unfold under tension [162], resulting in viscoelastic solid-like behavior [79, 163]. Spectraplakins, which interlink actin, microtubules and neurofilaments [164], and neurofilaments themselves [165] are other crosslinkers that may unfold under tension. To gain physical insight into

the axon response to stretch, we therefore developed a model of tension relaxation arising from unfolding/re-folding of generic protein crosslinkers within the axon cytoskeleton.

We consider a simplified model axon, treated as a cylinder that is homogeneous along its length. As a result, we suppose that each cross-section is pierced by $M$ types of elastic elements in parallel; this is illustrated in Fig. 1A. Each type of element, representing a type of crosslinking protein with folded and unfolded repeats and labeled by the index $i$, is assumed to have $n_i$ copies in a cross-section. At mechanical equilibrium the total axon tension, $\mathcal{T}$, is uniform, and thus it can be expressed as the sum of tensions acting on the $\sum_{i=1}^{M} n_i$ elements:

$$\mathcal{T} = \sum_{i=1}^{M} n_i T_i \,. \tag{1}$$

In this equation, $T_i$ is the tension acting on a typical, or average, element of type $i$. The functional form of $T_i$ depends on the choice of elastic model for the element, which is not a crucial aspect of the problem. Without assuming any particular polymer model for the moment, $T_i$ depends on the ratio of the element's end-to-end extension $\ell_i'$ to its contour, or relaxed, length $\ell_i$: $T_i = T_i(\ell_i'/\ell_i)$. Throughout, primed lengths refer to the end-to-end extension of an element and unprimed lengths refer to its contour distance. We thus expect that $T_i$ decreases with increasing $\ell_i$. This is a first key aspect of the model: $\ell_i$ changes in time because of unfolding and re-folding events, and can thus result in softening. Furthermore, we assume that each elastic element stretches affinely, meaning that the imposed strain $\gamma$ is felt all the way down to the single element level. This implies that $\ell_i' = (1+\gamma)\ell_{i0}'$, where $\ell_{i0}'$ is the initial length of element $i$ before imposed stretching occurs ($\gamma = 0$); this is illustrated in Fig. 1A. As a result, we can express each $T_i$ as a function of strain:

$$T_i = T_i(\Lambda)\,; \quad \Lambda \equiv \lambda \ell_{i0}'/\ell_i \,, \tag{2}$$

where $\lambda = 1 + \gamma$ is the axon deformation.

In the next step, since protein domain unfolding and re-folding will affect its

contour length [111], we propose that the dynamics of the rest length of element $i$ is governed by a rate equation relating to unfolding and folding events:

$$\frac{d\ell_i}{dt} = -\nu_{if}\,(\ell_i - \ell_{if}) + \nu_{iu}\,(\ell_{iu} - \ell_i)\,. \tag{3}$$

Here, $\nu_{if}$ and $\nu_{iu}$ are rates that represent domain re-folding and unfolding, respectively, on element $i$, and $\ell_{if}$ and $\ell_{iu}$, such that $\ell_{if} < \ell_{iu}$, are the rest lengths in the fully folded and fully unfolded states. We note that $\ell_i - \ell_{if}$ and $\ell_{iu} - \ell_i$ are proportional to the number of unfolded and folded domains, respectively, on element $i$. Generally, we expect that tension accelerates unfolding and hinders re-folding: this is a second key aspect of the model. We assume a molecular scale description of unfolding and re-folding, in which the folded and unfolded states of a domain are represented by neighbouring minima of an energy function; see Fig. 1A. The effect of the tension on element $i$ is then to tilt the energy landscape down towards the unfolded state, so that in a first approximation [112], the rates are given by

$$\nu_{iu} = \nu_{iu}(0)\, e^{\beta T_i \Delta x_i^{\mathrm{fu}}} \tag{4}$$

$$\nu_{if} = \nu_{if}(0)\, e^{-\beta T_i \Delta x_i^{\mathrm{uf}}}\,, \tag{5}$$

where $\beta = (k_{\mathrm{B}}\mathrm{T})^{-1}$ with $k_{\mathrm{B}}$ the Boltzmann's constant and T the temperature. In this equation, $\nu_{iu}(0)$ and $\nu_{if}(0)$ are the unfolding and re-folding rates in the absence of tension. The quantities $\Delta x_i^{\mathrm{fu}}$ and $\Delta x_i^{\mathrm{uf}}$ are lengths representing the changes in reaction coordinate in going from the folded to the unfolded state, and vice-versa.

We are now in position to model the experimental protocol and make sense of our results. For a given choice of function $T_i$ and a given deformation $\lambda$, we can solve Eqs. 2-5 for the steady-state rest length $\ell_i^{\mathrm{ss}}$, yielding the relation $\ell_i^{\mathrm{ss}} = (\nu_{iu}\,\ell_{iu} + \nu_{if}\,\ell_{if})/(\nu_{iu} + \nu_{if})$. Note that this equation must be solved numerically since the rates depend on $\ell_i^{\mathrm{ss}}$ through Eqs. 2 and 4-5. Next, at a chosen time denoted $t = t_{\mathrm{step}}$, we apply a small but sudden change in strain, $\delta\gamma$. Right after the step, the tension jumps to a value $T_i(t = t_{\mathrm{step}}) = T_i((\lambda + \delta\gamma)\ell'_{i0}/\ell_i^{\mathrm{ss}})$. The tension will then decay as $\ell_i$ increases from $\ell_i^{\mathrm{ss}}$ due to unfolding. By solving for

the linearized relaxation behaviour, we can show that the total tension relaxes as a sum of exponentials as follows:

We suppose that the model axon is initially at steady state, with rest lengths $\{\ell_i^{\rm ss}\}$ obtained by solving Eq. 3 with $d\ell_i/dt = 0$. From this steady-state, a sudden, small change in strain, $\delta\gamma$, is applied at some time $t = t_{\rm step}$. The lengths $\{\ell_i\}$ will change in time and relax to a new steady state. The total tension $\mathcal{T}$ will evolve, too. Linearizing Eq.3 for small changes $\delta\ell_i$ yields

$$\frac{d\delta\ell_i}{dt} = -(\nu_{\rm if}^{\rm ss} + \nu_{\rm iu}^{\rm ss})\,\delta\ell_i - \delta\nu_{\rm if}\,(\ell_i^{\rm ss} - \ell_{\rm if}) + \delta\nu_{\rm iu}\,(\ell_{\rm iu} - \ell_i^{\rm ss})\,. \tag{6}$$

Here, $\nu_{\rm if}^{\rm ss}$ and $\nu_{\rm iu}^{\rm ss}$ are the folding and unfolding rates at the steady-state prior to $t_{\rm step}$. Writing $\delta\nu_{\rm if} = \delta\ell_i \left.\frac{d\nu_{\rm if}}{d\ell_i}\right|_{\rm ss}$ and $\delta\nu_{\rm iu} = \delta\ell_i \left.\frac{d\nu_{\rm iu}}{d\ell_i}\right|_{\rm ss}$, where the derivatives are evaluated at the steady- state prior to $t_{\rm step}$, we find that Eq. 6 can be re-written in the form

$$\frac{d\delta\ell_i}{dt} = -\frac{1}{\tau_i}\delta\ell_i\,, \tag{7}$$

where the relaxation time $\tau_i$ is

$$\tau_i = \left[(\nu_{\rm if}^{\rm ss} + \nu_{\rm iu}^{\rm ss}) + (\ell_i^{\rm ss} - \ell_{\rm if})\left.\frac{d\nu_{\rm if}}{d\ell_i}\right|_{\rm ss} + (\ell_i^{\rm ss} - \ell_{\rm iu})\left.\frac{d\nu_{\rm iu}}{d\ell_i}\right|_{\rm ss}\right]^{-1}. \tag{8}$$

Thus, after the step, each $\delta\ell_i$ will relax exponentially with characteristic time $\tau_i$. Since each tension $T_i$ is a function of $\ell_i$, the linearized change in tension $T_i$ will also relax exponentially, with the same characteristic time. Thus, the total tension, Eq.1, will evolve according to following equation,

$$\mathcal{T}(t) = \sum_{i=1}^{M} n_i T_i(t = t_{\rm step})\, e^{-(t-t_{\rm step})/\tau_i}\,, \tag{9}$$

with relaxation times $\tau_i$ that depend on the strain prior to the small jump.

To proceed further, we consider only one type of element and henceforth drop the label $i$. We now derive the equation for relaxation time, From eqs. 4 and 5,

$$\frac{d\nu_{\mathrm{u}}}{d\ell} = -\nu_{\mathrm{u}} \frac{\Lambda K(\Lambda)}{\ell} \beta \Delta x^{\mathrm{uf}} \tag{10}$$

$$\frac{d\nu_{\mathrm{f}}}{d\ell} = \nu_{\mathrm{f}} \frac{\Lambda K(\Lambda)}{\ell} \beta \Delta x^{\mathrm{fu}} . \tag{11}$$

Here, $K = dT/d\Lambda$. Equation 8 can then be re-written

$$\tau = \left\{ (\nu_{\mathrm{f}} + \nu_{\mathrm{u}}) + \beta \frac{\Lambda K(\Lambda)}{\ell} \left[ (\ell - \ell_{\mathrm{f}}) \Delta x^{\mathrm{fu}} \nu_{\mathrm{f}} + (\ell_{\mathrm{u}} - \ell) \Delta x^{\mathrm{uf}} \nu_{\mathrm{u}} \right] \right\}^{-1} , \tag{12}$$

where it is understood all quantities are evaluated at the steady-state prior to $t_{\mathrm{step}}$, and we have dropped the superscript ss. Finally, noting that the steady state rest length is given by $\ell = (\ell_{\mathrm{u}}\nu_{\mathrm{u}} + \ell_{\mathrm{f}}\nu_{\mathrm{f}})/(\nu_{\mathrm{u}} + \nu_{\mathrm{f}})$, the above equation, after some algebra, can be simplified to

$$\tau = \left[ (\nu_{\mathrm{u}} + \nu_{\mathrm{f}}) + \frac{\nu_{\mathrm{u}}\nu_{\mathrm{f}}}{(\nu_{\mathrm{u}} + \nu_{\mathrm{f}})} \frac{(\ell_{\mathrm{u}} - \ell_{\mathrm{f}})}{\ell} \beta (\Delta x^{\mathrm{fu}} + \Delta x^{\mathrm{uf}}) \Lambda K(\Lambda) \right]^{-1} , \tag{13}$$

where $K(\Lambda) = dT(\Lambda)/d\Lambda$ is the differential stiffness. In Eq. 13 all strain-dependent quantities are evaluated at the steady-state condition holding prior to $t = t_{\mathrm{step}}$. Also, we note that the first term in this equation is what one would obtain if the unfolding and re-folding rates were constant. The second term accounts for the dependence of these rates on the relaxed length of the element.

Next, we use the worm-like chain (WLC) approximation for the element tension $T$ [114], which has been used previously to model spectrin unfolding [111]:

$$T = \frac{1}{\beta \ell_p} \left( \frac{1}{4(1 - \lambda \ell_0'/\ell)^2} + \frac{\lambda \ell_0'}{\ell} - \frac{1}{4} \right) , \tag{14}$$

where $\ell_p$ is the persistence length, and is assumed to be independent of the folding state. This model predicts strain *stiffening* for constant rest length, that is, the slope $\partial T/\partial \lambda$ increases with $\lambda$. It is thus a useful test case to see to what extent the relaxation of the rest length $\ell(t)$ can lead to softening.

Our model can qualitatively reproduce the experimental axon stretch response (Fig. 3.3). During a jump in strain, the tension rises quickly and then relaxes, as

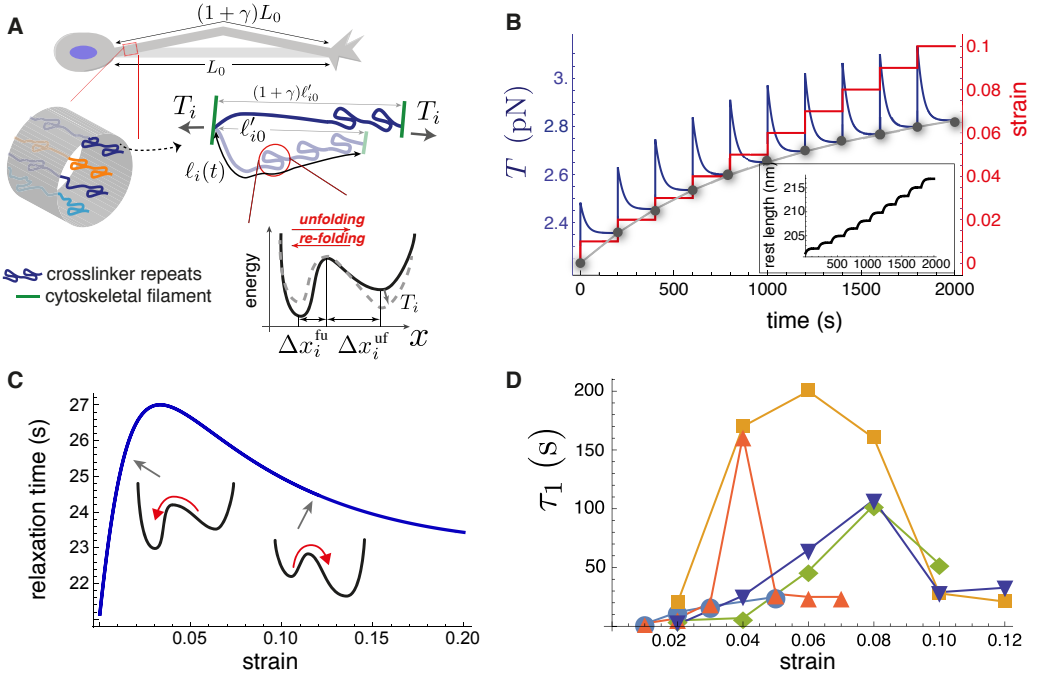


FIGURE 1: **Theoretical model recapitulates strain-softening and tension relaxation.** **(A)** Schematic illustration of stretched axon, showing unfolding of a crosslinking protein repeat as an underlying tension relaxation mechanism. The axon, initially with length $L_0$, is stretched to $(1+\gamma)L_0$. In the model, any cylindrical portion of axon contains various crosslinking proteins (shown using different colors) that experience the strain $\gamma$. The contour length of the crosslinker between two cytoskeletal filaments, $\ell_i(t)$, is variable because of repeat unfolding and re-folding. This process is represented by an energy potential with two minima. The tension, $T_i$, pushes the unfolded minimum down and the folded minimum up. **(B)** Model calculation for a single elastic element for multiple step-strain protocol. Tension versus time (purple) shows a jump after strain increment is applied (red), followed by relaxation to a steady-state value (gray points, passed through by the equilibrium tension versus extension curve (gray). This relaxation coincides with progressive repeat unfolding, as represented by the change in rest length $\ell(t)$ (inset). **(C)** Tension relaxation after a small change in applied strain is exponential, with a relaxation time, $\tau$, that depends non-monotonically on strain. The inset cartoons are to show that $\tau$ is largely controlled by re-folding at low strain, and by unfolding at higher strain. **(D)** Fitting the tension relaxation data obtained from experiments like the one shown in Fig. 3.3 to a function that is the sum of two exponentials (Fig. 3.8, Fig. 3.10) reveals a long relaxation time (denoted $\tau_1$) with a qualitatively similar dependence on strain as with the model Fig. 1C and a short relaxation time $\tau_2$ (Fig. 3.10). Model calculations in B and D were done using the following parameters for spectrin: $\ell_p = 20$ nm [166], $\ell'_0 = 170$ nm [7], $\Delta x^{\mathrm{fu}} = 2.5$ nm, $\Delta x^{\mathrm{uf}} = 15$ nm, $\ell_{\mathrm{u}} = 1200$ nm, and $\ell_{\mathrm{f}} = 200$ nm. We also used $\nu_{\mathrm{f}}(0) = 100\ \mathrm{s}^{-1}$, $\nu_{\mathrm{u}}(0) = 10^{-5}\ \mathrm{s}^{-1}$ [167] and $k_{\mathrm{B}}T = 4$ pN.nm.

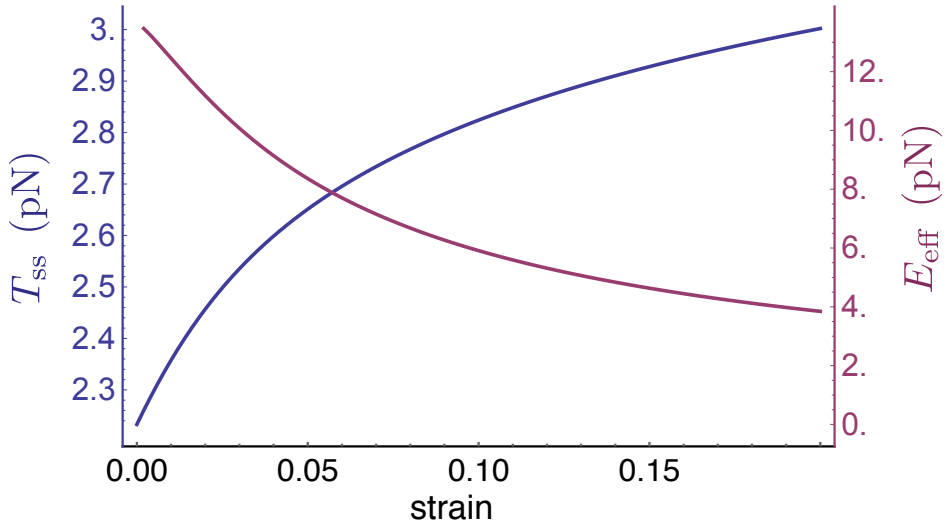


FIGURE 2: Model equilibrium tension and effective modulus vs. strain. Model equilibrium tension, $T_{ss}$ and effective Young's modulus, $E_{eff}$ versus strain curve for a single elastic element. The tension curve (blue) is obtained by solving Eqs. 2-5 and 8 of the main text at equilibrium ($d\ell/dt = 0$). The Young's modulus curve (purple) is obtained by taking $T_{ss} - T_0$, with $T_0$ the tension at zero strain, and dividing this quantity by the strain $\gamma$. The parameters used for both plots are values appropriate for spectrin tetramers: $\ell_p = 20$ nm, $\ell_0' = 170$ nm, $\Delta x^{fu} = 2.5$ nm, $\Delta x^{uf} = 15$ nm, $\ell_u = 1200$ nm, and $\ell_f = 200$ nm. We also used $\nu_f(0) = 100$ s$^{-1}$, $\nu_u(0) = 10^{-5}$ s$^{-1}$, and $k_BT = 4$ pN.nm.

crosslinking protein repeats unfold; see Fig. 1B. We use values of $\ell_p$, $\ell_0'$, $\ell_f$, $\ell_u$, $\Delta x^{fu}$, $\Delta x^{uf}$, $\nu_f(0)$, and $\nu_u(0)$ appropriate for spectrin. At long times after each strain step, the tension tends to a steady-state value such that the locus of values follows the steady-state tension versus strain curve, $T_{ss}$ found by solving Eqs. 3-5 and 14 (gray dots in Fig. 1B). We note that the model predicts that the crosslinker is under tension for zero applied strain, as is the case for the entire axon. Importantly, the $T_{ss}$ curve reflects the tension buffering behavior seen experimentally Fig. 3.3, and Ref. [111]]. This buffering, or softening, arises in the model because of a significant increase in the rest length $\ell(t)$ for strains not exceeding 10% ( inset of Fig. 1B, Fig. 2). Taken together, our hypothesis of tension-assisted unfolding of crosslinking proteins can account for the axon strain softening seen experimentally.

With our model we also predict a surprising, non-monotonic dependence of the tension relaxation time $\tau$ on strain; see Fig. 1C. This behavior can be understood as follows. For small strain, we expect that the energy minimum of the folded state is much lower than the minimum of the unfolded state. As a result, we expect then that $\nu_u \ll \nu_f$; this disparity has been measured experimentally [167].

Since $\nu_{\rm f}$ decreases with tension, according to Eq. 13, the relaxation time is then $\tau \approx \nu_{\rm f}^{-1}$, which increases with strain, for small strain. With increasing strain the last term in Eq. 13, which is $\propto \nu_{\rm u}^{-1} \propto e^{-\beta T \Delta x}$, becomes important, and leads to a decreasing relaxation time with strain. Remarkably, fitting our axon tension versus time data for a multi-step strain protocol (Fig. 3.3 and Fig. 3.8 with a function $A\, e^{-(t-t_{\rm step})/\tau_1} + B\, e^{-(t-t_{\rm step})/\tau_2} + C$ we see that both relaxation times $\tau_1$ and $\tau_2$ first increase then decrease with strain; see Fig. 1D. This result is in full qualitative agreement with our model, which is predicated on multiple types of crosslinking proteins in parallel, thus multiple tension relaxation times (Eq. 9), each with a similar non-monotonic dependence on strain.

## Choice of numerical values used to generate Fig. 1B and Fig. 1C

We used a choice a parameters appropriate for spectrin to generate Fig. 1B and Fig. 1C. For the persistence length, we used $\ell_p = 20$ nm, as measured for erythrocytes [166]. For the initial end-to-end extension, we note that the distance between adjacent actin rings in the axon is about 180-190 nm [7]. Accounting for the thickness of a ring, we assumed a value of $\ell_0' = 170$ nm. Next, we used $\ell_{\rm f} = 200$ nm as the fully folded rest length of a spectrin tetramer, based on each folded repeat being 5 nm long and there being about 40 repeats along the length of the tetramer. The amount of contour length added upon repeat unfolding is broadly distributed [168], but we may assume a value of 25 nm. Doing so, we have $\ell_{\rm u} = 1200$ nm.

The transition from the folded to the unfolded state involves crossing an energy barrier, as illustrated in Fig. 1A, representing the intramolecular bonds that need to be broken. The so-called activation length $\Delta x^{\rm fu}$, which is the change in reaction coordinate (aligned with the tension) between the barrier position and the folded minimum, is assumed to be 2.5 nm. This value is consistent with an earlier estimate [112]. The value of the activation length for the reverse reaction, $\Delta x^{\rm uf}$, is

expected to be considerably larger, since a significant conformation change of the protein is needed to re-fold. We estimate this to be $\Delta x^{\mathrm{uf}} \sim \frac{\ell_{\mathrm{u}}}{\ell_{\mathrm{f}}} \Delta x^{\mathrm{fu}} = 17.5$ nm.

Finally, for the unfolding and re-folding rates in the absence of tension, we take $\nu_{\mathrm{u}}(0) = 10^{-5}$ s$^{-1}$ and $\nu_{\mathrm{f}}(0) = 100$ s$^{-1}$. These values are similar to those measured in Ref. [167]. Given the choice of the other parameters described above, this choice of zero-force rates yielded tension relaxation times comparable to those measured for our axon stretching experiments.

# Bibliography


[1] Seshagiri Rao, R., C. Kalelkar, and P. A. Pullarkat, 2013. Optical fiber-based force transducer for microscale samples. *Review of Scientific Instruments* 84:105107.

[2] Alberts, B., A. Johnson, J. Lewis, M. Raff, K. Roberts, and P. Walter, 2002. Molecular Biology of the Cell. Garland, New York.

[3] Fletcher, D. A., and R. D. Mullins, 2010. Cell mechanics and the cytoskeleton. *Nature* 463:485–492.

[4] Bayly, P., T. Cohen, E. Leister, D. Ajo, E. Leuthardt, and G. Genin, 2005. Deformation of the human brain induced by mild acceleration. *Journal of Neurotrauma* 22:845–856.

[5] Foelix, R. F., 2011. Biology of Spiders. Oxford University Press, 3rd edition edition.

[6] Yarger, J. L., B. R. Cherry, and A. van der Vaart, 2018. Uncovering the structure–function relationship in spider silk. *Nature Reviews Materials* 3.

[7] Xu, K., G. Zhong, and X. Zhuang, 2013. Actin, spectrin, and associated proteins form a periodic cytoskeletal structure in axons. *Science* 339:452–456.

[8] Franze, K., and J. Guck, 2010. The biophysics of neuronal growth. *Reports on Progress in Physics* 73:094601.

[9] Dennerll, T. J., H. C. Joshi, V. L. Steel, R. E. Buxbaum, and S. R. Heidemann, 1988. Tension and compression in the cytoskeleton of PC-12 neurites. II: Quantitative measurements. *The Journal of Cell Biology* 107:665–674.

[10] Bernal, R., P. A. Pullarkat, and F. Melo, 2007. Mechanical properties of axons. *Physical Review Letters* 99:018301.

[11] Rajagopalan, J., A. Tofangchi, and M. T. A. Saif, 2010. Drosophila Neurons Actively Regulate Axonal Tension In Vivo. *Biophysical Journal* 99:3208 – 3215.

[12] Dubey, S., N. Bhembre, S. Bodas, A. Ghose, A. Callan-Jones, and P. A. Pullarkat, 2019. The axonal actin-spectrin lattice acts as a tension buffering shock absorber. *BioRxiv* .

[13] Hammarlund, M., E. M. Jorgensen, and M. J. Bastiani, 2007. Axons break in animals lacking $\beta$-spectrin. *Journal of Cell Biology* 176:269–275.

[14] Zhong, G., J. He, R. Zhou, D. Lorenzo, H. P. Babcock, V. Bennett, and X. Zhuang, 2014. Developmental mechanism of the periodic membrane skeleton in axons. *Elife* 3:e04581.

[15] Blackledge, T. A., 2012. Spider silk: a brief review and prospectus on research linking biomechanics and ecology in draglines and orb webs. *The Journal of Arachnology* 40:1 – 12.

[16] Tommasi, D. D., G. Puglisi, and G. Saccomandi, 2010. Damage, Self-Healing, and Hysteresis in Spider Silks. *Biophysical Journal* 98:1941 – 1948.

[17] Johns, P., 2014. Clinical Neuroscience. Churchill Livingstone, 1st edition edition.

[18] Smith, D. H., M. Nonaka, R. Miller, M. J. Leoni, X. Chen, D. Alsop, and D. F. Meaney, 2000. Immediate coma following inertial brain injury dependent on axonal damage in the brainstem. *Journal of neurosurgery* 93:315–22.

[19] Johnson, V. E., W. Stewart, and D. H. Smith, 2013. Axonal pathology in traumatic brain injury. *Experimental Neurology* 246:35–43.

[20] Meaney, D. F., and D. H. Smith, 2011. Biomechanics of Concussion. *Clinics in Sports Medicine* 30:19–31.

[21] Tang-Schomer, M. D., A. R. Patel, P. W. Baas, and D. H. Smith, 2010. Mechanical breaking of microtubules in axons during dynamic stretch injury underlies delayed elasticity, microtubule disassembly, and axon degeneration. *The FASEB Journal* 24:1401–1410.

[22] Tang-Schomer, M. D., V. E. Johnson, P. W. Baas, W. Stewart, and D. H. Smith, 2012. Partial interruption of axonal transport due to microtubule breakage accounts for the formation of periodic varicosities after traumatic axonal injury. *Experimental Neurology* 233:364 – 372. Special Issue: Stress and neurological disease.

[23] Adalbert, R., and M. P. Coleman, 2013. Review: Axon pathology in age-related neurodegenerative disorders. *Neuropathology and Applied Neurobiology* 39:90–108.

[24] Marner, L., J. R. Nyengaard, Y. Tang, and B. Pakkenberg, 2003. Marked loss of myelinated nerve fibers in the human brain with age. *Journal of Comparative Neurology* 462:144–152.

[25] Suter, D. M., and K. E. Miller, 2011. The emerging role of forces in axonal elongation. *Progress in Neurobiology* 94:91 – 101.

[26] Hahn, I., A. Voelzmann, Y.-T. Liew, B. Costa-Gomes, and A. Prokop, 2019. The model of local axon homeostasis - explaining the role and regulation of microtubule bundles in axon maintenance and pathology. *Neural Development* 14.

[27] Phillips, J. B., X. Smit, N. D. Zoysa, A. Afoke, and R. A. Brown, 2004. Peripheral nerves in the rat exhibit localized heterogeneity of tensile properties during limb movement. *The Journal of Physiology* 557:879–887.

[28] Lillie, M. A., A. W. Vogl, K. N. Gil, J. M. Gosline, and R. E. Shadwick, 2017. Two levels of waviness are necessary to package the highly extensible nerves in rorqual whales. *Current Biology* 27:673–679.

[29] Bray, D., 1984. Axonal growth in response to experimentally applied mechanical tension. *Developmental biology* 102:379–389.

[30] Dennerll, T. J., P. Lamoureux, R. E. Buxbaum, and S. R. Heidemann, 1989. The cytomechanics of axonal elongation and retraction. *The Journal of Cell Biology* 109:3073–3083.

[31] Franze, K., P. A. Janmey, and J. Guck, 2013. Mechanics in Neuronal Development and Repair. *Annual Review of Biomedical Engineering* 15:227–251. PMID: 23642242.

[32] Franze, K., 2013. The mechanical control of nervous system development. *Development* 140 15:3069–77.

[33] Hirokawa, N., 1982. Cross-linker system between neurofilaments, microtubules and membranous organelles in frog axons revealed by the quick-freeze, deep-etching method. *The Journal of cell biology* 94:129–142.

[34] Howard, J., 2001. Mechanics of Motor Proteins and the Cytoskeleton. Sinauer Associates, Inc.

[35] Gardel, M. L., K. E. Kasza, C. P. Brangwynne, J. Liu, and D. A. Weitz, 2008. Chapter 19 Mechanical Response of Cytoskeletal Networks. *In* Biophysical Tools for Biologists, Volume Two: In Vivo Techniques, Academic Press, volume 89 of *Methods in Cell Biology*, 487 – 519.

[36] Kapitein, L. C., and C. C. Hoogenraad, 2015. Building the Neuronal Microtubule Cytoskeleton. *Neuron* 87:492–506.

[37] Kevenaar, J. T., and C. C. Hoogenraad, 2015. The axonal cytoskeleton: from organization to function. *In* Front. Mol. Neurosci.

[38] Lobsiger, C. S., and D. W. Cleveland, 2009. Neurofilaments: Organization and Function in Neurons. *In* Encyclopedia of Neuroscience.

[39] Hisanaga, S., and N. Hirokawa, 1989. The Effects of Dephosphorylation of Neurofilament on the Structure of the Projections. *Journal of Neuroscience* 9:959–966.

[40] Elder, G. A., V. L. Friedrich, A. Margita, and R. A. Lazzarini, 1999. Age-Related Atrophy of Motor Axons in Mice Deficient in the Mid-Sized Neurofilament Subunit. *The Journal of Cell Biology* 146:181–192.

[41] D'Este, E., D. Kamin, F. Göttfert, A. El-Hady, and S. W. Hell, 2015. STED nanoscopy reveals the ubiquity of subcortical cytoskeleton periodicity in living neurons. *Cell Reports* 10:1246–1251.

[42] Leterrier, C., P. Dubey, and S. Roy, 2017. The nano-architecture of the axonal cytoskeleton. *Nature Reviews Neuroscience* 18:713.

[43] Ganguly, A., Y. Tang, L. Wang, K. Ladt, J. Loi, B. Dargent, C. Leterrier, and S. Roy, 2015. A dynamic formin-dependent deep F-actin network in axons. *The Journal of Cell Biology* 210:401–417.

[44] Roy, S., 2016. Waves, rings, and trails: The scenic landscape of axonal actin. *The Journal of Cell Biology* 212:131–134.

[45] Bray, D., 1979. Mechanical tension produced by nerve cells in tissue culture. *Journal of Cell Science* 37:391–410.

[46] Betz, T., D. Koch, Y.-B. Lu, K. Franze, and J. A. Käs, 2011. Growth cones as soft and weak force generators. *Proceedings of the National Academy of Sciences* 108:13420–13425.

[47] Lamoureux, P., R. E. Buxbaum, and S. R. Heidemann, 1989. Direct evidence that growth cones pull. *Nature* 340:159–162.

[48] Weiss, P., 1945. Experiments on cell and axon orientation in vitro: The role of colloidal exudates in tissue organization. *Journal of Experimental Zoology* 100:353–386.

[49] Zheng, J., P. Lamoureux, V. Santiago, T. Dennerll, R. Buxbaum, and S. Heidemann, 1991. Tensile regulation of axonal elongation and initiation. *Journal of Neuroscience* 11:1117–1125.

[50] Ahmed, W. W., T. C. Li, S. S. Rubakhin, A. Chiba, J. V. Sweedler, and T. A. Saif, 2012. Mechanical Tension Modulates Local and Global Vesicle Dynamics in Neurons. *Cellular and Molecular Bioengineering* 5:155–164.

[51] Siechen, S., S. Yang, A. Chiba, and T. Saif, 2009. Mechanical tension contributes to clustering of neurotransmitter vesicles at presynaptic terminals. *Proceedings of the National Academy of Sciences* 106:12611–12616.

[52] Ayali, A., 2010. The function of mechanical tension in neuronal and network development. *Integr. Biol.* 2:178–182.

[53] Tofangchi, A., A. Fan, and M. T. A. Saif, 2016. Mechanism of Axonal Contractility in Embryonic Drosophila Motor Neurons In Vivo. *Biophysical Journal* 111:1519 – 1527.

[54] Athamneh, A., and D. Suter, 2015. Quantifying mechanical force in axonal growth and guidance. *Frontiers in Cellular Neuroscience* 9:359.

[55] Tofangchi, A., A. Fan, and M. T. A. Saif, 2016. Mechanism of axonal contractility in embryonic drosophila motor neurons in vivo. *Biophysical Journal* 111:1519–1527.

[56] Mutalik, S. P., J. Joseph, P. A. Pullarkat, and A. Ghose, 2018. Cytoskeletal mechanisms of axonal contractility. *Biophysical Journal* 115:713–724.

[57] Bernal, R., 2006. FUERZAS CELULARES.

[58] Bernal, R., F. Melo, and P. A. Pullarkat, 2010. Drag Force as a Tool to Test the Active Mechanical Response of PC12 Neurites. *Biophysical Journal* 98:515 – 523.

[59] O'Toole, M., P. Lamoureux, and K. E. Miller, 2008. A Physical Model of Axonal Elongation: Force, Viscosity, and Adhesions Govern the Mode of Outgrowth. *Biophysical Journal* 94:2610 – 2620.

[60] O'Toole, M., P. Lamoureux, and K. E. Miller, 2015. Measurement of subcellular force generation in neurons. *Biophysical Journal* 108:1027–1037.

[61] Polacheck, W. J., and C. S. Chen, 2016. Measuring cell-generated forces: a guide to the available tools. *Nature Methods* 13:415–423.

[62] Sahin, O., S. Magonov, C. Su, C. F. Quate, and O. Solgaard, 2007. An atomic force microscope tip designed to measure time-varying nanomechanical forces. *Nature nanotechnology* 2 8:507–14.

[63] Ashkin, A., 1997. Optical trapping and manipulation of neutral particles using lasers. *Proceedings of the National Academy of Sciences* 94:4853–4860.

[64] Guck, J., R. Ananthakrishnan, H. Mahmood, T. J. Moon, C. C. Cunningham, and J. Ks, 2001. The Optical Stretcher: A Novel Laser Tool to Micromanipulate Cells. *Biophysical Journal* 81:767 – 784.

[65] Haber, C., and D. Wirtz, 2000. Magnetic tweezers for DNA micromanipulation. *Review of Scientific Instruments* 71:4561–4570.

[66] Smith, D. H., 2009. Stretch growth of integrated axon tracts: Extremes and exploitations. *Progress in Neurobiology* 89:231 – 239.

[67] Datar, A., 2014. Mechanism of shape transformation and retraction in axons.

[68] Krieg, M., A. R. Dunn, and M. B. Goodman, 2014. Mechanical control of the sense of touch by $\beta$-spectrin. *Nature Cell Biology* 16:224.

[69] Ouyang, H., E. Nauman, and R. Shi, 2013. Contribution of cytoskeletal elements to the axonal mechanical properties. *Journal of biological engineering* 7:21.

[70] Grevesse, T., B. E. Dabiri, K. K. Parker, and S. Gabriele, 2015. Opposite rheological properties of neuronal microcompartments predict axonal vulnerability in brain injury. *Scientific reports* 5:9475.

[71] Fernández, P., P. A. Pullarkat, and A. Ott, 2006. A master relation defines the nonlinear viscoelasticity of single fibroblasts. *Biophysical Journal* 90:3796–3805.

[72] Kollmannsberger, P., and B. Fabry, 2011. Linear and nonlinear rheology of living cells. *Annual Review of Materials Research* 41:75–97.

[73] Storm, C., J. J. Pastore, F. C. MacKintosh, T. C. Lubensky, and P. A. Janmey, 2005. Nonlinear elasticity in biological gels. *Nature* 435:191.

[74] Fernández, P., P. A. Pullarkat, and A. Ott, XXXX. A Master Relation Defines the Nonlinear Viscoelasticity of Single Fibroblasts. *Biophysical Journal* 90:3796–3805.

[75] Shah, J. V., and P. A. Janmey, 1997. Strain hardening of fibrin gels and plasma clots. *Rheologica Acta* 36:262–268.

[76] Gardel, M., J. H. Shin, F. MacKintosh, L. Mahadevan, P. Matsudaira, and D. Weitz, 2004. Elastic behavior of cross-linked and bundled actin networks. *Science* 304:1301–1305.

[77] Chaudhuri, O., S. H. Parekh, and D. A. Fletcher, 2007. Reversible stress softening of actin networks. *Nature* 445:295.

[78] Astrom, J. A., P. B. S. Kumar, I. Vattulainen, and M. Karttunen, 2008. Strain hardening, avalanches, and strain softening in dense cross-linked actin networks. *Phys. Rev. E* 77:051913.

[79] Ahmadzadeh, H., D. H. Smith, and V. B. Shenoy, 2015. Mechanical effects of dynamic binding between tau proteins on microtubules during axonal injury. *Biophysical Journal* 109:2328–2337.

[80] de Rooij, R., and E. Kuhl, 2018. Physical Biology of Axonal Damage. *Frontiers in Cellular Neuroscience* 12:144.

[81] Johnson, C. P., H.-Y. Tang, C. Carag, D. W. Speicher, and D. E. Discher, 2007. Forced unfolding of proteins within cells. *Science* 317:663–666.

[82] Rief, M., J. Pascual, M. Saraste, and H. E. Gaub, 1999. Single molecule force spectroscopy of spectrin repeats: low unfolding forces in helix bundles. *Journal of Molecular Biology* 286:553–561.

[83] Gov, N. S., 2007. Active elastic network: cytoskeleton of the red blood cell. *Physical Review E* 75:011921.

[84] Lee, J. C., and D. E. Discher, 2001. Deformation-enhanced fluctuations in the red cell skeleton with theoretical relations to elasticity, connectivity, and spectrin unfolding. *Biophysical Journal* 81:3178–3192.

[85] Trepat, X., L. Deng, S. S An, D. Navajas, D. J Tschumperlin, W. T Gerthoffer, J. P Butler, and J. J. Fredberg, 2007. Universal physical responses to stretch in the living cell. *Nature* 447:592–595.

[86] Trepat, X., G. Lenormand, and J. J. Fredberg, 2008. Universality in cell mechanics. *Soft Matter* 4:1750–1759.

[87] Yengo, C. M., Y. Takagi, and J. R. Sellers, 2012. Temperature dependent measurements reveal similarities between muscle and non-muscle myosin motility. *Journal of Muscle Research and Cell Motility* 33:385–394.

[88] Hong, W., A. Takshak, O. Osunbayo, A. Kunwar, and M. Vershinin, 2016. The Effect of Temperature on Microtubule-Based Transport by Cytoplasmic Dynein and Kinesin-1 Motors. *Biophysical Journal* 111:1816.

[89] Yao, N. Y., C. P. Broedersz, Y.-C. Lin, K. E. Kasza, F. C. MacKintosh, and D. A. Weitz, 2010. Elasticity in ionically cross-linked neurofilament networks. *Biophysical journal* 98:2147–2153.

[90] Das, A., and R. Dubreuil, 2009. Spectrin: Organization and Function in Neurons. *In* L. R. Squire, editor, Encyclopedia of Neuroscience, Academic Press, Oxford, 213 – 218.

[91] Baines, A. J., 2009. Evolution of spectrin function in cytoskeletal and membrane networks. *Biochemical Society Transactions* 37:796–803.

[92] Bennett, V., and A. J. Baines, 2001. Spectrin and Ankyrin-Based Pathways: Metazoan Inventions for Integrating Cells Into Tissues. *Physiological Reviews* 81:1353–1392. PMID: 11427698.

[93] Liu, S. C., L. H. Derick, and J. Palek, 1987. Visualization of the hexagonal lattice in the erythrocyte membrane skeleton. *The Journal of Cell Biology* 104:527–536.

[94] Gokhin, D. S., R. B. Nowak, J. A. Khoory, A. d. l. Piedra, I. C. Ghiran, and V. M. Fowler, 2015. Dynamic actin filaments control the mechanical behavior of the human red blood cell membrane. *Molecular Biology of the Cell* 26:1699–1710.

[95] Bennett, V., and J. M. Healy, 2009. Membrane domains based on ankyrin and spectrin associated with cell-cell interactions. *Cold Spring Harbor perspectives in biology* 1:a003012.

[96] He, J., R. Zhou, Z. Wu, M. A. Carrasco, P. T. Kurshan, J. E. Farley, D. J. Simon, G. Wang, B. Han, J. Hao, et al., 2016. Prevalent presence of periodic actin–spectrin-based membrane skeleton in a broad range of neuronal cell types and animal species. *Proceedings of the National Academy of Sciences* 113:6029–6034.

[97] Qu, Y., I. Hahn, S. E. Webb, S. P. Pearce, and A. Prokop, 2017. Periodic actin structures in neuronal axons are required to maintain microtubules. *Molecular biology of the cell* 28:296–308.

[98] Pielage, J., R. D. Fetter, and G. W. Davis, 2006. A postsynaptic Spectrin scaffold defines active zone size, spacing, and efficacy at the Drosophila neuromuscular junction . *The Journal of Cell Biology* 175:491–503.

[99] Garbe, D. S., A. Das, R. R. Dubreuil, and G. J. Bashaw, 2007. beta-Spectrin functions independently of Ankyrin to regulate the establishment and maintenance of axon connections in the Drosophila embryonic CNS. *Development* 134 2:273–84.

[100] Smith, D. H., J. A. Wolf, T. A. Lusardi, V. M.-Y. Lee, and D. F. Meaney, 1999. High Tolerance and Delayed Elastic Response of Cultured Axons to Dynamic Stretch Injury. *Journal of Neuroscience* 19:4263–4269.

[101] Ikeda, Y., K. A. Dick, M. R. Weatherspoon, D. Gincel, K. R. Armbrust, J. C. Dalton, G. Stevanin, A. Dürr, C. Zühlke, K. Bürk, et al., 2006. Spectrin mutations cause spinocerebellar ataxia type 5. *Nature Genetics* 38:184.

[102] Wang, Y., T. Ji, A. D. Nelson, K. Glanowska, G. G. Murphy, P. M. Jenkins, and J. M. Parent, 2018. Critical roles of $\alpha$II spectrin in brain development and epileptic encephalopathy. *The Journal of Clinical Investigation* 128.

[103] Vassilopoulos, S., S. Gibaud, A. Jimenez, G. Caillol, and C. Leterrier, 2019. Ultrastructure of the axonal periodic scaffold reveals a braid-like organization of actin rings. *bioRxiv* .

[104] Leite, S. C., P. Sampaio, V. F. Sousa, J. Nogueira-Rodrigues, R. Pinto-Costa, L. L. Peters, P. Brites, and M. M. Sousa, 2016. The Actin-Binding Protein -Adducin Is Required for Maintaining Axon Diameter. *Cell Rep* 15:490–8.

[105] Brown, J. W., E. Bullitt, S. Sriswasdi, S. Harper, D. W. Speicher, and C. J. McKnight, 2015. The Physiological Molecular Shape of Spectrin: A Compact Supercoil Resembling a Chinese Finger Trap. *PLOS Computational Biology* 11:1–20.

[106] Qu, Y., I. Hahn, S. E. Webb, S. P. Pearce, and A. Prokop, 2017. Periodic actin structures in neuronal axons are required to maintain microtubules. *Molecular Biology of the Cell* 28:296–308. PMID: 27881663.

[107] Wang, G., D. J. Simon, Z. Wu, D. M. Belsky, E. Heller, M. K. O'Rourke, N. T. Hertz, H. Molina, G. Zhong, M. Tessier-Lavigne, and X. Zhuang, 2019. Structural plasticity of actin-spectrin membrane skeleton and functional role of actin and spectrin in axon degeneration. *eLife* .

[108] Unsain, N., M. D. Bordenave, G. F. Martinez, S. Jalil, C. von Bilderling, F. M. Barabas, L. A. Masullo, A. D. Johnstone, P. A. Barker, M. Bisbal, F. D. Stefani, and A. Cáceres, 2018. Remodeling of the Actin/Spectrin Membrane-associated Periodic Skeleton, Growth Cone Collapse and F-Actin Decrease during Axonal Degeneration. *Scientific Reports* .

[109] Dubey, S., N. Bhembre, S. Bodas, S. Veer, A. Ghose, A. Callan-Jones, and P. A. Pullarkat, 2020. The axonal actin-spectrin lattice acts as a tension buffering shock absorber. *eLife* 9:e51772.

[110] Leterrier, C., P. Dubey, and S. Roy, 2017. The nano-architecture of the axonal cytoskeleton. *Nature Reviews Neuroscience* 18:713–726.

[111] Rief, M., J. Pascual, M. Saraste, and H. E. Gaub, 1999. Single molecule force spectroscopy of spectrin repeats: low unfolding forces in helix bundles. *J Mol Biol* 286:553–61.

[112] Zhu, Q., and R. J. Asaro, 2008. Spectrin folding versus unfolding reactions and RBC membrane stiffness. *Biophysical Journal* 94:2529–2545.

[113] Bell, G., 1978. Models for the specific adhesion of cells to cells. *Science* 200:618–627.

[114] Marko, J. F., and E. D. Siggia, 1995. Stretching DNA. *Macromolecules* 28:8759–8770.

[115] Yu, W., and P. Baas, 1994. Changes in microtubule number and length during axon differentiation. *Journal of Neuroscience* 14:2818–2829.

[116] Harmer, A. M. T., T. A. Blackledge, J. S. Madin, and M. E. Herberstein, 2011. High-performance spider webs: integrating biomechanics, ecology and behaviour. *Journal of The Royal Society Interface* 8:457–471.

[117] Vollrath, F., 2000. Strength and structure of spiders silks. *Reviews in Molecular Biotechnology* 74:67 – 83.

[118] Lubin, Y., and T. Bilde, 2007. The Evolution of Sociality in Spiders. *Advances in the Study of Behavior* 37:83 – 145.

[119] Avilés, L., 1997. Causes and consequences of cooperation and permanent-sociality in spiders, Cambridge University Press, 476–498.

[120] Gosline, J. M., M. DeMont, and M. W. Denny, 1986. The structure and properties of spider silk. *Endeavour* 10:37 – 43.

[121] Blackledge, T. A., and C. Y. Hayashi, 2006. Unraveling the mechanical properties of composite silk threads spun by cribellate orb-weaving spiders. *Journal of Experimental Biology* 209:3131–3140.

[122] Blackledge, T. A., A. P. Summers, and C. Y. Hayashi, 2005. Gumfooted lines in black widow cobwebs and the mechanical properties of spider capture silk. *Zoology* 108:41 – 46.

[123] Eberhard, W., and F. Pereira, 1993. Ultra structure of Cribellate Silk of Nine Species in Eight Families and Possible Taxonomic Implications (Araneae: Amaurobiidae, Deinopidae, Desidae, Dictynidae, Filistatidae, Hypochilidae, Stiphidiidae, Tengellidae). *The Journal of Arachnology* 21:161–174.

[124] Opell, B. D., 1994. Increased Stickness of Prey Capture Threads Accompanying Web Reduction in the Spider Family Uloboridae. *Functional Ecology* 8:85–90.

[125] Sahni, V., T. A. Blackledge, and A. Dhinojwala, 2011. A Review on Spider Silk Adhesion. *The Journal of Adhesion* 87:595–614.

[126] Blackledge, T. A., and C. Y. Hayashi, 2006. Silken toolkits: biomechanics of silk fibers spun by the orb web spider Argiope argentata (Fabricius 1775). *Journal of Experimental Biology* 209:2452–2461.

[127] Jiang, P., C. Guo, T. Lv, Y. Xiao, X. Liao, and B. Zhou, 2011. Structure, composition and mechanical properties of the silk fibres of the egg case of the Joro spider, Nephila clavata (Araneae, Nephilidae). *Journal of Biosciences* 36:897–910.

[128] Blamires, S. J., T. A. Blackledge, and I.-M. Tso, 2017. Physicochemical Property Variation in Spider Silk: Ecology, Evolution, and Synthetic Production. *Annual review of entomology* 62:443–460.

[129] Blamires, S. J., M. Nobbs, P. J. Martens, I.-M. Tso, W.-T. Chuang, C.-K. Chang, and H.-S. Sheu, 2018. Multiscale mechanisms of nutritionally induced property variation in spider silks. *PLOS ONE* 13:1–23.

[130] Glisovic, A., T. Vehoff, R. J. Davies, and T. Salditt, 2008. Strain Dependent Structural Changes of Spider Dragline Silk. *Macromolecules* 41:390–398.

[131] Simmons, A. H., C. A. Michal, and L. W. Jelinski, 1996. Molecular Orientation and Two-Component Nature of the Crystalline Fraction of Spider Dragline Silk. *Science* 271:84–87.

[132] Creager, M. S., J. E. Jenkins, L. A. Thagard-Yeaman, A. E. Brooks, J. A. Jones, R. V. Lewis, G. P. Holland, and J. L. Yarger, 2010. Solid-state NMR comparison of various spiders' dragline silk fiber. *Biomacromolecules* 11 8:2039–43.

[133] Lefèvre, T., F. Paquet-Mercier, J.-F. Rioux-Dubé, and M. Pézolet, 2012. Review structure of silk by raman spectromicroscopy: from the spinning glands to the fibers. *Biopolymers* 97 6:322–36.

[134] Shao, Z., F. Vollrath, J. Sirichaisit, and R. Young, 1999. Analysis of spider silk in native and supercontracted states using Raman spectroscopy. *Polymer* 40:2493 – 2500.

[135] Sponner, A., E. Unger, M. Görlach, and K. Weisshart, 2005. Differential polymerization of the two main protein components of dragline silk during fibre spinning. *Nature Materials* 4:772–775.

[136] Xu, M., and R. V. Lewis, 1990. Structure of a protein superfiber: spider dragline silk. *Proceedings of the National Academy of Sciences of the United States of America* 87 18:7120–4.

[137] Vehoff, T., A. Gliovi, H. Schollmeyer, A. Zippelius, and T. Salditt, 2007. Mechanical Properties of Spider Dragline Silk: Humidity, Hysteresis, and Relaxation. *Biophysical Journal* 93:4425 – 4432.

[138] Elices, M., G. V. Guinea, J. Pérez-Rigueiro, and G. R. Plaza, 2005. Finding inspiration in argiope trifasciata spider silk fibers. *JOM* 57:60–66.

[139] Agnarsson, I., C. Boutry, and T. A. Blackledge, 2008. Spider silk aging: initial improvement in a high performance material followed by slow degradation. *Journal of experimental zoology. Part A, Ecological genetics and physiology* 309 8:494–504.

[140] Blackledge, T. A., C. Boutry, S.-C. Wong, A. Baji, A. Dhinojwala, V. Sahni, and I. Agnarsson, 2009. How super is supercontraction? Persistent versus cyclic responses to humidity in spider dragline silk. *The Journal of experimental biology* 212 Pt 13:1981–9.

[141] Liu, Y., Z. Shao, and F. Vollrath, 2005. Extended wet-spinning can modify spider silk properties. *Chem. Commun.* 2489–2491.

[142] Joshi, C. H., 2018. Behavioral ecology and silk biomechanics of Stegodyphus sarasinorum (Eresidae).

[143] Dubey, S., C. H. Joshi, S. Veer, D. Uma, H. Somanathan, S. Majumdar, and P. A. Pullarkat, 2020. Strain softening and stiffening responses of spider silk fibers probed using a Micro-Extension Rheometer. *Soft Matter* 16:487–493.

[144] Seshagiri Rao, R. V., 2014. An Optical Fibre based Force Apparatus Applications to Soft and Living Matter.

[145] Blackledge, T. A., J. E. Swindeman, and C. Y. Hayashi, 2005. Quasistatic and continuous dynamic characterization of the mechanical properties of silk from the cobweb of the black widow spider Latrodectus hesperus. *The Journal of experimental biology* 208:1937–1949.

[146] Evans, R. M. L., M. Tassieri, D. Auhl, and T. A. Waigh, 2009. Direct conversion of rheological compliance measurements into storage and loss moduli. *Phys. Rev. E* 80:012501.

[147] Ferry, J., 1980. Viscoelasticity Properties of Polymers. *Wiley, 3rd Edition* .

[148] Park, S. W., and Y. R. Kim, 1999. Interconversion between Relaxation Modulus and Creep Compliance for Viscoelastic Solids. *Journal of Materials in Civil Engineering* 11:76–82.

[149] Lepore, E., M. Isaia, S. Mammola, and N. M. Pugno, 2016. The effect of ageing on the mechanical properties of the silk of the bridge spider Larinioides cornutus (Clerck, 1757). *Scientific reports* 6:24699.

[150] Peakall, D. B., 1971. Conservation of web proteins in the spider, Araneus diadematus. *The Journal of experimental zoology* 176 3:257–64.

[151] van Beek, J. D., S. Hess, F. Vollrath, and B. H. Meier, 2002. The molecular structure of spider dragline silk: Folding and orientation of the protein backbone. *Proceedings of the National Academy of Sciences* 99:10266–10271.

[152] Liu, Y., Z. Shao, and F. Vollrath, 2005. Relationships between supercontraction and mechanical properties of spider silk. *Nature Materials* 4:901–905.

[153] Termonia, Y., 1994. Molecular Modeling of Spider Silk Elasticity. *Macromolecules* 27:7378–7381.

[154] Oroudjev, E., J. Soares, S. Arcidiacono, J. B. Thompson, S. A. Fossey, and H. G. Hansma, 2002. Segmented nanofibers of spider dragline silk: Atomic force microscopy and single-molecule force spectroscopy. *Proceedings of the National Academy of Sciences* 99:6460–6465.

[155] Nova, A., S. Keten, N. M. Pugno, A. Redaelli, and M. J. Buehler, 2010. Molecular and nanostructural mechanisms of deformation, strength and toughness of spider silk fibrils. *Nano letters* 10 7:2626–34.

[156] Alam, P., 2014. Protein unfolding versus β-sheet separation in spider silk nanocrystals. *Advances in Natural Sciences: Nanoscience and Nanotechnology* 5:015015.

[157] Keten, S., and M. J. Buehler, 2007. Geometric confinement governs the rupture strength of H-bond assemblies at a critical length scale. *Nano letters* 8 2:743–8.

[158] Pijaudier-Cabot, G., Z. P. Bazant, and M. R. Tabbara, 1988. Comparison of various models for strainsoftening. *Engineering Computations* 5:141–150.

[159] Lee, H., J. M. Ferrer, M. J. Lang, and R. D. Kamm, 2010. Molecular origin of strain softening in cross-linked F-actin networks. *Phys. Rev. E* 82:011919.

[160] Eckels, E. C., R. Tapia-Rojo, J. A. Rivas-Pardo, and J. M. Fernndez, 2018. The Work of Titin Protein Folding as a Major Driver in Muscle Contraction. *Annual Review of Physiology* 80:327–351. PMID: 29433413.

[161] Yao, M., B. T. Goult, B. Klapholz, X. Hu, C. P. Toseland, Y. Guo, P. Cong, M. P. Sheetz, and J. Yan, 2016. The mechanical response of talin. *Nature Communications* 7:11966.

[162] Wegmann, S., J. Schöler, C. A. Bippes, E. Mandelkow, and D. J. Muller, 2011. Competing interactions stabilize pro- and anti-aggregant conformations of human Tau. *J Biol Chem* 286:20512–24.

[163] Ahmadzadeh, H., D. H. Smith, and V. B. Shenoy, 2014. Viscoelasticity of tau proteins leads to strain rate-dependent breaking of microtubules during axonal stretch injury: predictions from a mathematical model. *Biophysical Journal* 106:1123–1133.

[164] Suozzi, K. C., X. Wu, and E. Fuchs, 2012. Spectraplakins: master orchestrators of cytoskeletal dynamics. *J Cell Biol* 197:465–75.

[165] Aranda-Espinoza, H., P. Carl, J. F. Leterrier, P. Janmey, and D. E. Discher, 2002. Domain unfolding in neurofilament sidearms: effects of phosphorylation and ATP. *FEBS Lett* 531:397–401.

[166] Stokke, B., A. Mikkelsen, and A. Elgsaeter, 1986. Spectrin, human erythrocyte shapes, and mechanochemical properties. *Biophysical Journal* 49:319 – 327.

[167] Scott, K. A., S. Batey, K. A. Hooton, and J. Clarke, 2004. The Folding of Spectrin Domains I: Wild-type Domains Have the Same Stability but very Different Kinetic Properties. *Journal of Molecular Biology* 344:195 – 205.

[168] Lenne, P. F., A. J. Raae, S. M. Altmann, M. Saraste, and J. K. Hörber, 2000. States and transitions during forced unfolding of a single spectrin repeat. *FEBS Lett* 476:124–8.